



UNIVERSITA' DELLA CALABRIA

Dipartimento di Chimica

Scuola di Dottorato

Bernardino Telesio – Scuola di Scienza e Tecnica

Indirizzo

Mesofasi e Materiali Molecolari, M³

XXVI CICLO

**Modelling of nanostructured membranes
for wastewater purification**

Settore Scientifico Disciplinare CHIM/02 Chimica Fisica

Direttore: Ch.mo Prof. Roberto BARTOLINO

Supervisore: Ch.mo Dr. Giorgio DE LUCA

Dottorando: Dott./ssa Federica BISIGNANO

Eadem Mutata Resurgo
Jacob Bernoulli (1654-1705)

Contents

Abstract	v
1 Introduction	1
1.1 Nanoscale science and nanostructures	1
1.2 Nanoenhanced membranes for water treatment	4
1.3 Aim of the thesis	7
1.4 Methodology and Outline of the thesis	10
2 Theoretical background	17
2.1 Introduction	17
2.2 Density Functional Theory	18
2.3 Role of noncovalent bonds	23
3 Implemented algorithms	29
3.1 Zigzag carbon nanotubes	29
3.2 Molecular topological analysis	34
3.3 Pore molecular sieving	39
3.3.1 Maximun free area and Molecular permeation area . .	39
4 CNTs properties	51
4.1 On rejection of Carbon Nanotubes	51
4.1.1 Introduction	51
4.1.2 The geometric criterion	52
4.1.3 Computational approaches and models	54

4.1.4	Results and discussion	56
4.1.5	Conclusions	62
4.2	Perm-Selectivity optimization of Olygomer-IM functionalised CNT-polymer membranes	62
4.2.1	Introduction	62
4.2.2	Materials and methodology	64
4.2.3	Molecular models and computational details	68
4.2.4	Results and discussion	73
4.2.5	Conclusions	79
5	Bromide ion exchange with a Keggin polyoxometalate on functionalized polymeric membranes	85
5.1	Introduction	85
5.2	Molecular models and computational details	87
5.3	Results and discussions	91
5.4	Conclusion	97
6	Conclusions	103
A	Appendix	105
	Acknowledgments	111

Abstract

Nel trattamento delle acque reflue industriali la rimozione di inquinanti ed il recupero di molecole a basso peso molecolare con alto valore aggiunto sono sfide attuali. I processi a membrana possono essere considerati come una valida opzione alla risoluzione di questi problemi. Due aspetti molto importanti che devono essere ottimizzati nei processi di separazione a membrana sono un'alta reiezione di materia organica ed alta permeabilità di acqua. In generale l'aumento del primo va a scapito dell'altro in quanto alta reiezione causa lo sporcamento della membrana che a sua volta riduce drammaticamente la permeabilità dell'acqua. Di fondamentale importanza in questo campo è la progettazione di materiali innovativi che possano mostrare alta permeabilità all'acqua ed allo stesso tempo reiezione molecolare con una bassa propensione allo sporcamento. Membrane composite costituite dall'aggiunta di nanostrutture come Nanotubi di Carbonio (CNTs) o Nano particelle (NPs) stanno ricevendo un'enorme attenzione in quanto le proprietà di queste strutture possono migliorare l'efficienza della membrana in termini di permeabilità, selettività, resistenza ed infine prevenzione dello sporcamento. La scelta del giusto nanomateriale può essere altamente velocizzata da una modellazione computazionale. Pertanto in questa tesi è stato effettuato uno studio modellistico *ab-initio* nell'ambito della Density Functional Theory (DFT) al fine di investigare le relazioni struttura-proprietà delle nanostrutture come ad esempio CNTs e NPs di poliossometallati (POM). Queste nanostrutture sono usate nella preparazione di membrane composite all'interno del progetto BioNexGen [1] al fine di proporre nuove membrane da utilizzare in bioreat-

tori per il trattamento delle acque reflue industriali. In particolare è stata analizzata la reiezione da CNTs di soluti organici a basso peso molecolare provenienti da acque reflue di industrie cosmetiche, farmaceutiche e da frantoi in combinazione con l'ottimizzazione della permeabilità all'acqua attraverso i CNTs. In aggiunta è stato analizzato l'adsorbimento di POM sulla superficie di membrane polimeriche con lo scopo di capire se l'aggiunta di queste nanoparticelle che posseggono eccellenti proprietà antibatteriche e ossidanti, potesse conferire alla membrana un'efficiente prevenzione allo sporco.

Mentre la permeabilità dei nanotubi è stata ampiamente studiata sia da un punto di vista sperimentale che modellistico mostrando per nanotubi aventi diametri nel range dell'osmosi inversa e della nanofiltrazione [2] un aumento della portata di acqua pari a vari ordini di grandezza, meno lavoro è stato fatto per la selettività di piccoli soluti organici. Un preciso controllo della sintesi dei CNT permette di mettere a punto i diametri esterni ed interni nel caso di nanotubi a parete singola e multipla (rispettivamente SWNT e MWNT) offrendo la possibilità di controllare la loro selettività verso piccoli soluti. Pertanto in questa tesi uno studio modellistico fu rivolto a definire l'ottimale diametro interno del CNT che dovrebbe essere usato al fine di raggiungere una totale reiezione di vari composti selezionati che sono difficili da separare. Per raggiungere gli obiettivi summenzionati, in questa tesi sono stati implementati tre nuovi algoritmi [3, 4]. Questi algoritmi non usano alcun parametro aggiustabile (cioè parametri di fitting) poichè sono basati sulle ottimizzazioni delle geometrie effettuate tramite un alto livello di approcci quantistici (DFT) e su analisi topologiche dei sistemi in esame. Le caratteristiche geometriche dei CNT inoltre dovrebbero essere ottimizzate al fine di ottenere un giusto compromesso fra permeabilità e reiezione. Come promettente soluzione a questo problema [5, 6] è stata proposta la funzionalizzazione della bocca dei nanotubi con specifici gruppi funzionali abili ad ostacolare il passaggio dei soluti pur permettendo alle molecole di acqua di fluire. Così in questo lavoro è stato effettuato uno studio teorico di membrane CNT-composite con l'obiettivo di ottimizzare la bocca dei CNT

mediante una funzionalizzazione che sia in grado di massimizzare sia la permeabilità dell'acqua che la selettività dei soluti. Questo studio è la base del terzo algoritmo implementato [7].

Relativamente allo sporcamento della membrana, al fine di raggiungere un ottimale adsorbimento di anioniche NPs antibatteriche (cioè POM) sulla superficie di membrane polimeriche, è stata effettuata un'analisi dell'adsorbimento di queste NPs. Sono state valutate le interazioni noncovalenti tra POM e surfattanti commerciali usati nella preparazione della membrana. I POM anionici sono infatti promettenti agenti antibatterici [8] e quindi un efficiente scambio con gli ioni di bromuro, che sono usati per controbilanciare la carica positiva dei surfattanti commerciali, permetterebbe un aumento dell'efficienza della membrana tramite una riduzione dello sporcamento organico e biologico. Al fine di raggiungere questo risultato oltre alle summenzionate interazioni noncovalenti POM-surfattanti fu valutata anche l'energia elettronica di idratazione degli anioni POM e bromuro in modo da predire il probabile scambio di questi anioni sulla superficie polimerica.

Le conclusioni di questa tesi sono state raggiunte utilizzando solo metodi *ab-initio* e quindi i risultati possono essere considerati abbastanza generali ed omogenei, liberi da parametri empirici o di fitting. Relativamente allo scambio tra POM e bromuro è fornita una validazione della predizione teorica mediante un esperimento progettato *ad hoc*. I risultati sperimentali sono in accordo con le predizioni teoretiche [9].

Abstract

The removal of pollutants as well as the recovery of high added value molecules with low molecular weight is a current challenge in the wastewater treatment. Membrane processes can be considered as a viable option to solve these issues. In separations based membranes, high rejection of organic matter and water high permeability are two very important aspects that must be optimised. In general, the increase of the former comes at the expense

of the latter because high rejection is cause of membrane fouling which in turns reduces dramatically the water permeability. Thus, membrane fouling constitutes one of the major limitations in membrane separation processes. The design of innovative materials which show high water permeability and at same time molecular rejection but with a low propensity to fouling is of fundamental relevance in this area. Mixed-matrix composite membranes where nanostructures such as Carbon Nano Tubes (CNTs) or Nano particles (NPs) are added, are receiving a huge focus since the properties of these nanostructures can confer an increase of the membrane efficiency in terms of permeability, selectivity, resistance and finally antifouling. The choice of the right nanomaterial can be highly accelerated by computational modelling. Thus, in this thesis an *ab-initio* modelling study in the frame of the Density Functional Theory (DFT) is carried out in order to investigate the structure-property relationships of nanostructures like CNTs and polyoxometalates NPs (POM). These nanostructures are used in the preparation of composite membranes in the frame of BioNexGen project [1] with the aim to propose novel membranes to be used in bioreactor for industrial waste water treatment. In particular, the rejection of CNTs towards organic solutes with low molecular weight coming from industrial waste water such as cosmetic, textile and oil olive was analysed in conjunction to the optimization of water permeability in CNTs. Also, the adsorption of POMs on polymeric membrane surface was analysed in order to understand if an efficient antifouling property can be imparted to the membranes by adding these NPs which possess excellent antibacterial and oxidants properties.

While nanotube permeability has been extensively studied in both experimental and modelling works resulting in orders of magnitude water flow enhancements for tube diameters in the reverse osmosis and nanofiltration range [2], less work has been done on CNT selectivity of small organic solutes. Precise control of the CNTs synthesis allows for fine-tuning of the outer and inner diameters in the case of single- and multi-wall carbon nanotubes (SWNTs and MWNTs, respectively), offering the possibility of controlling

their selectivity toward small solutes. In this thesis a modelling study was, therefore, addressed to define the optimal CNT internal diameter that should be used in order to achieve a total rejection of several target compounds very difficult to separate. Three novel algorithms [3, 4] were implemented during the thesis for reach the aforementioned objective. These algorithms do not make use of any adjustable parameters (i.e. fitting parameters) being based on geometry optimizations carried out in the frame of high level of quantum approach (DFT) and topological analysis of the considered systems. In addition, the CNTs geometrical characteristics should be optimized in order to get the best compromise between permeability and rejection. The functionalizing of the nanotubes tip with specific functional groups capable of hindering the passage of solutes while allowing water molecules to flow has been suggested as a solution to this problem [5, 6]. Thus, a theoretical study of CNT-composite membranes was carried out in this work with the aim of optimizing the CNTs tip, through their functionalization, to maximise both water permeability and solutes selectivity. This study is the basis of the third implemented algorithm [7].

Concerning the membrane fouling, the analysis of the adsorption of antibacterial anionic NPs (i.e. POM) on the surface of polymeric membranes was carried out in this thesis in order to achieve an optimal adsorption of these NPs. Noncovalent interactions between POM and commercial surfactants, used in polymer membrane preparations, were evaluated. Anionic POMs are in fact promising antibacterial agents [8], therefore, an efficient exchange with the bromide ions, used to counterbalance the positive charge of the commercial surfactants, would allow to increase the efficiency of the membrane by reducing the organic and bio fouling. In order to achieve this result, besides the aforementioned POM-surfactants noncovalent interactions the electronic hydration energy of POM and bromide anions was also evaluated in order to predict the probable exchange of these anions on the polymer surface.

The conclusions of this thesis are achieved by using only *ab-initio* methods

thus the results can be considered quite general and homogeneous, free from empirical or fitting parameters. A validation of the theoretical prediction is provided concerning the POM-bromide exchange by means of an *ad hoc* designed experiment. The experimental results are in agreement with the theoretical predictions [9].

Bibliography

- [1] www.bionexgen.eu
- [2] M. Whitby, N. Quirke (2007) *Nat. Nano.* 2, 87.
- [3] A. Buekenhoudt, F. Bisignano, G. DeLuca, P. Vandezande, M. Wouters, K. Verhulst (2013) *Journal of Membrane Science* 439 36-47
- [4] F. Bisignano, E. K. Karahaliou, V. G. Mavrantzas and G. De Luca *On rejection of Carbon Nano Tubes: a Density Functional and Molecular Dynamic study* (to be submitted)
- [5] B. Corry (2011) *Energy & Environmental Science* 4, 751
- [6] G. De Luca, A. Gugliuzza, and E. Drioli (2009) *J. Phys. Chem. B*, 113, 5473-5477
- [7] F. Bisignano, D. Mattia, G. De Luca *Selectivity-permeability optimization of functionalised CNT-polymer membranes for water treatment: a modelling study* (to be submitted)
- [8] M. Carraro, A. Sartorel, M. Ibrahim, N. Nsouli, C. Jahier, S. Nlate, U. Kortz, M. Bonchio (2012) Ed: P. Andersson, Wiley-WCH, pp 1-XX
- [9] G. De Luca, F. Bisignano, A. Figoli, F. Galiano, E. Furia, R. Mancuso, O. Saoncella, M. Carraro, M. Bonchio, and B. Gabriele (2013) *Bromide ion exchange with a Keggin polyoxometalate on functionalized polymeric membranes: a theoretical and experimental study* *Journal of Physical Chemistry* (submitted, Manuscript ID: jp-2013-11401v)

Chapter 1

Introduction

1.1 Nanoscale science and nanostructures

“If I were asked for an area of science and engineering that will most likely produce the breakthroughs of tomorrow, I would point to nanoscale science and engineering.” (Dr. Neal Lane on April 1998 [1]).

Nanoscale science, engineering and technology are areas that deal with matter on the nanometer length scale. Small features permit more functionality in a given space, but nanoscience is not only a simple continuation of miniaturization from micron meter scale down to nanometer scale. The essence of nanotechnology is the ability to work at the molecular level, atom by atom, to create large structures with fundamentally new molecular organization. Compared to the behavior of isolated molecules of about 1 nm (10^{-9} m) or of bulk materials, behavior of structural features in the range of about 10^{-9} to 10^{-7} m (1 to 100 nm) exhibit important changes. There are many definitions of nanotechnology and this reflect the fact that nanotechnology covers a broad spectrum of the research field. In general, nanotechnology can be understood as a technology of design, fabrication, and applications of nanostructures and nanomaterials [2]. It is concerned with materials and systems whose structures and components exhibit novel and significantly improved physical, chemical, and biological properties, phenomena, and processes due

to their nanoscale size [1].

Nanostructured materials (NSMs) as a subject of nanotechnology are low dimensional materials comprising of building units of a sub-micron or nanoscale size at least in one direction. The first classification idea of NSMs was given by Gleiter in 1995 [3] and further was explained by Skorokhod in 2000 [4]. However, Gleiter and Skorokhod scheme was not fully considered because of novel nanostructures (NSs) obtained in the past two decades, such as fullerenes, nanotubes, and nanoflowers were not taken into account. Therefore, Pokropivny and Skorokhod [5] reported a modified scheme in which a classification of NSs and NSMs is given. As reported by the European Commission in [6] “*Nanomaterial means a natural, incidental or manufactured material containing particles, in an unbound state or as an aggregate or as an agglomerate and where, for 50 % or more of the particles in the number size distribution, one or more external dimensions is in the size range 1 nm - 100 nm*”. The characterized particles are known as nanostructures, therefore NSs should be separated from NSMs since the former are characterized by a form and dimensionality while the last by a composition in addition. In Ref. [5] a restricted set of nanostructures classes was suggested to build from the constituting elementary units, namely, 0D clusters and particles, 1D nanotubes and nanowires, 2D nanoplates and layers. Thus all NSs, classified as 0D, 1D, 2D or 3D on the basis of their dimensionality, can be built from elementary units (blocks) having low dimensionality 0D, 1D, and 2D. The 3D units are excluded because they can't be used to build low dimensional NSs except 3D matrix. However 3D structures can be considered as NSMs if they involve the 0D, 1D, 2D NSs.

Three sorts of elementary units and other classes for a total of 36 classes were defined on the basis of the dimensionality as shown in Fig. 1.1. However some of the classes still remained thin demonstrating the predictive ability of the suggested classification of NSs. While plentiful man made materials with nanostructures have been in use for a long time (partially without knowing it) a change of the scientific and technological is related to a few key ideas and

Dimensionality classification of nanostructures (L < 100 - 500 nm)

Designation: dimensionality of NS \rightarrow $kDlmn$ \leftarrow dimensionality of elementary units
 $k \geq l, m, n$ $\{k, l, m, n\} = \{0, 1, 2, 3\}$

Elementary building units :

1. 0D Molecules, clusters, fullerenes, rings, metcarbs, thoroids, domens, particles, powders, grains, schwartzons	2. 1D nanotubes, fibers, filaments, whiskers, spirals, belts, springs, horns, columns, needles, pillars, helicoids, wires, ribbons	3. 2D layers
0D-nanostructures :		
4. 0D0 uniform particles arrays	5. 0D00 heterogeneous particles arrays, "core-shell" dendrimers, onions	
1D-nanostructures :		
7. 1D00 heteropolymers	8. 1D1 bundles, ropes, cables, corals	9. 1D11 heterochains, heterocables, saws, hair, heterobundles, junctions, combs, bows
	10. 1D10 beads, pea-pods, fullereno-fibers	
2D-nanostructures :		
11. 2D0 fullerene films	12. 2D1 nanostraw, PhC, fibers films	
13. 2D2 tiling, mosaic, layered films	14. 2D00 heterofilms of heteroparticles, fullereno-powders	15. 2D10 films of pods, fullereno-fibers
17. 2D20 fullereno-plate films	18. 2D21 bridges, fiber-layer films	19. 2D22 hetero-layers, MOS-structures
	20. 2D210 fullerene-fiber-layer films	16. 2D11 films of fibers and nanotubes, PhC-waveguides
3D-nanostructures :		
21. 3D0 Fullerites, clathrates, powder skeletons, fog	22. 3D1 skeletons of fibers, nanotubes	23. 3D2 layer skeletons, buildings, honeycombs, foams
24. 3D00 sols, colloids, smogs, heteroparticles composites	25. 3D10 skeletons of fibers-powders	26. 3D11 skeletons of heterofibers, nanotubes
27. 3D20 intercalates, skeletons of layers and powders	28. 3D21 Cross-bar-layers, layer-fiber skeletons	29. 3D22 heterolayers
30. 3D30 opals, dispersions, particles, pores, fullerenes in matrix	31. 3D31 membranes, PhC, fiber composites, waveguides	32. 3D32 friction pairs, contacts, interfaces, cavities, grain boundaries
33. 3D210 composites of layers, fibers and particles in matrix	34. 3D310 membranes + impurities, powder-fiber composites	35. 3D320 powder-layers composites
	36. 3D321 layers-fibers-composites in matrix, VCSEL	

Notices :

1. Interfaces between building units not regarded as additional 2D-NSs
2. Inverse NSs with cavity building units not regarded as separate ones
3. The classification may be extended with account of fourfold combinations

Figure 1.1: Dimensionality classification of nanostructures [5]

discoveries: the idea of assembling nanostructures from atomic, molecular or nanometer sized building blocks [7], the discovery of new forms of carbon, i.e., fullerenes [8] and carbon nanotubes (CNTs), and the development of scanning probe microscopy [9], such as scanning tunneling microscopy (STM) and atomic force microscopy (AFM). Thus, many researchers worldwide have worked intensively on the development of novel or improved synthesis methods and characterization techniques and on the measurement and the design of the properties of nanostructured materials [10]. Ultimately, the idea of nanostructured materials focuses on four key questions [11]: i) What nanostructures are interesting? ii) How can they be synthesized? iii) How can they be introduced into materials? iv) How can the relationships between their structures and compositions and their interfaces control the properties of the materials that incorporate them? The last question is an old one: “materials by design” has been a goal of materials science since its inception [12]. It remains, however, a difficult question, in fact, that the majority of research still focuses on the first three, where progress is easier to achieve and recognize.

In recent years the application of NSs is growing in several areas. For example, in the field of water treatment new NSs, such as carbon nanotubes, are receiving an increasing interest due to their remarkable property that, if conferred to the materials used for water treatment processes, can provide a real solution to the major challenges: removal of pollutants or recovery of valuable low molecular weight compounds and high water permeability in addition to preventing fouling of the materials.

1.2 Nanoenhanced membranes for water treatment

The main goal regarding the water treatment is the production of ultra pure water from different sources. Because of vastly expanding populations, increasing water demand, and the deterioration of water resource quality and

quantity, water is going to be the most precious resource in the world. According to the World Health Organisation, the most dangerous threat for health of mankind emerging within the next years is polluted water. The demand of clean water as basis for health and good living conditions is increasing for under developed countries in Africa but also for European countries that already partially suffer from insufficient clean water supply. Thus the low quantities of fresh water in these countries for industrial, agricultural and municipal usage should be well preserved by efficient, sustainable and cost-effective technologies.

There are many different methods to treat contaminated water; one being filtration. Membranes emerged as a viable means of water purification in the 1960s with the development of high performance synthetic membranes. Implementation of membranes for water treatment has progressed using more advanced membranes made from new materials and employed in various configurations. An increasing scarcity in fresh water sources fueled a push towards alternative resources such as ocean water. Proving successful at producing purified water from salt water, membranes became a viable alternative to evaporation-based technologies in the water treatment market. Over the past decade, there has been a rapid increase in the volume of wastewater that is treated with membranes to exceptionally high quality standards, typically for reuse purposes. In fact, today more municipal wastewater treatment facilities are using membrane technologies than ever, and this number is on the rise as the technology offers unparalleled capability in meeting rigorous requirements.

Different types of membranes are used for drinking water production and for the treatment and recycling of industrial wastewater. They include microfiltration (MF), ultrafiltration (UF), reverse osmosis (RO), and nanofiltration (NF) membranes (Fig. 1.2). However, despite the fact that in water purification technique a large number of small and large scale applications are reliant on membranes, they are not always cost-effective due to technical challenges that require further research and development. Relevant issues are

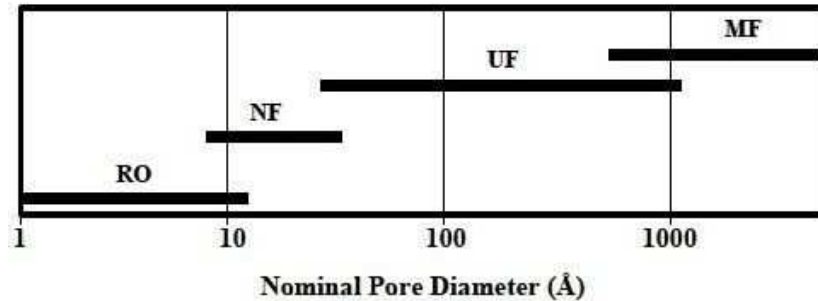


Figure 1.2: Range of nominal membrane pore sizes [13]

- increased flux;
- increased membrane selectivity;
- increased membrane resistance and lifetime. Numerous are in fact the drawbacks related to material resistance: chemical and biological degradation, swelling and embrittlement, mechanical and thermal resistances;
- reduction of membrane fouling. Membrane fouling is regarded as the main limitation for further development particularly when it leads to flux losses that cleaning cannot restore [14]. Generally, membrane fouling can be caused by a variety of constituents, among them bacteria, suspended solids, colloids as well as dissolved inorganic and organic compounds. It can be basically attributed to pore blocking (deposition within the pores) or to cake layer formation on the membrane surface [15].

Thus, particular attention should be given to the materials used in the membranes preparation with regard to the aforementioned issues.

The functionalization of membranes with nanoparticles is one way to address these challenges and hence, improve membrane performance. This method is rather new, and therefore several different terms are being used to describe this technology. In this thesis nanoenhanced membranes (NEMs)

will be used in order to indicate membranes that are functionalised with discrete nanoparticles or nanotubes.

NEMs aim to combining nanotechnology with membrane technology to improve membrane properties and hence increase their performance. Despite the idea of functionalizing membranes with nanoparticles is rather new, a large body of literature on NEMs exists even if most of this work is still in the laboratory stage and relatively far from actual implementation. There are different directions of research: some scientists are trying to integrate CNTs as pores in membranes [16, 17]. These membranes could be used instead of RO membranes for the production of ultrapure water with the advantage of an increased flux [18]. Other approaches involve the design of membranes from a CNT-mesh [19] or the surface functionalization of membranes with different nanoparticle types such as TiO_2 , Ag, aluminum oxides, silica, CNT, zirconia or iron oxides nanoparticles [20] to achieve increased flux and/or to reduce fouling. In Fig. 1.3 a classification of novel desalination NEMs is given.

In the Bionexgen project [22] the formation of NEMs by aligned CNTs with tailored physical and chemical properties for high-flux and selectivity performances is proposed in addition to the application of nanoparticles on the membranes surface as antimicrobial agents (Fig. 1.4). In particular Polyoxometalates (POMs), considered as the molecular analogs of solid metal-oxides, are proposed in order to take advance from the straightforward synthetic procedures by which the inorganic surface of molecular POMs can be tailored.

1.3 Aim of the thesis

The overall aim of this thesis was to investigate structures-properties relationships necessary in the development and design of innovative materials to be used in the fabrication of novel membranes. In particular as reference material in this work was considered a NEM in which vertically aligned

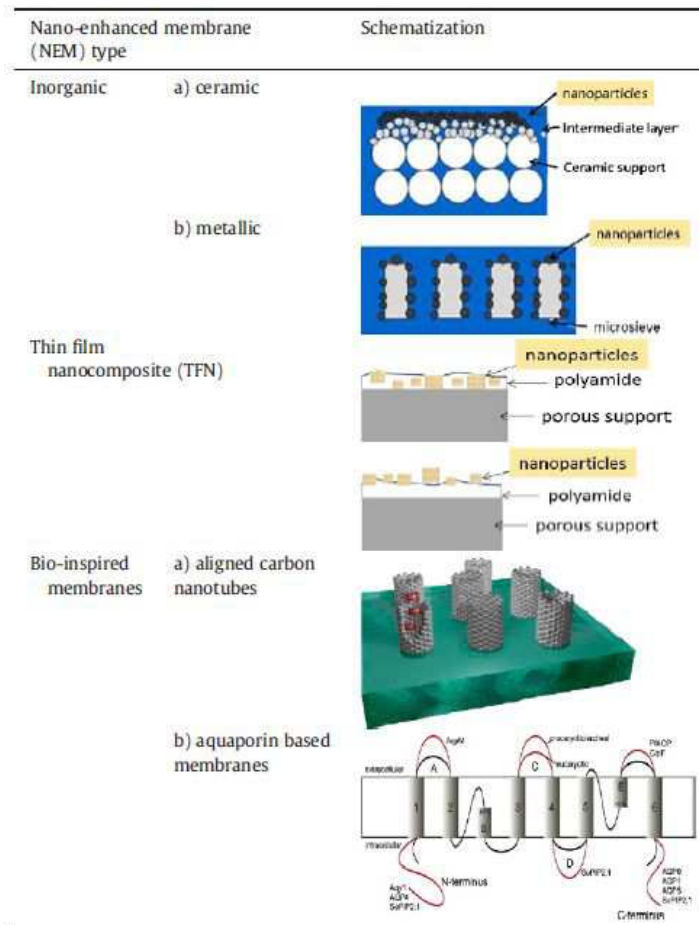


Figure 1.3: Classification of novel desalination membranes. [21]

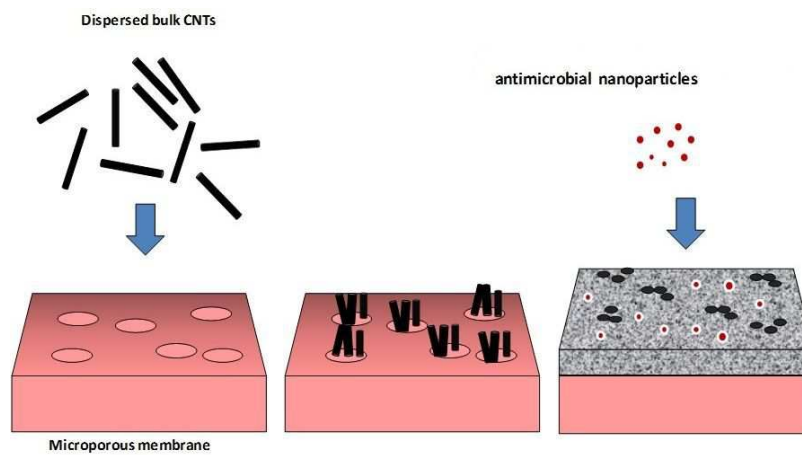


Figure 1.4: Proposed NEMs within BioNexGen project

CNTs and antibacterial nanoparticles are considered as added nanostructures Fig. 1.4. Thus the structure-property relationships of organic 1D and inorganic 0D elementary building units, i.e. carbon nanotubes and polyoxometalate nanoparticles, dispersed in membranes used for wastewater purification were investigated.

Enhanced flow rates were reported for membranes composed of an array of aligned CNTs. CNTs appear in fact to be the nanomaterial with the most potential to improve permeability as experimental and modeling results have shown orders of magnitude water flow enhancements than that predicted by traditional hydrodynamic models for tube diameters in the reverse osmosis and nanofiltration range [23]. In addition recent theoretical results have shown that CNTs with relatively low chirality (small diameters) should be used in order to obtain an efficient rejection of small organic solutes and ions [24, 25]. High fluxes, implying a high density of aligned CNTs in polymeric supports, coupled with a high rejection of small organic contaminants and ions are necessary in order to justify the use of novel membranes. However at present, high density of aligned CNTs can be difficult to obtain experimentally also considering that the materials and the techniques used in their preparation must be scaled economically to a level where they can supply the waste-water membrane market. In these terms for example the use of multi-wall or double-wall nanotubes is widely favored compared to that of single-wall nanotubes.

Overall, for an effective implementation of aligned CNT membranes in wastewater treatment, the problem of increase the rejection of small organic solutes from high chirality CNTs in order to control their permeability properties, namely, to keep the water flux high and that of certain ions as well, is an opened issue. Simulations studies on model pore (a mechanosensitive channel) [26, 27, 28, 29] indicate that a critical pore diameter exists above which water and ions will pass but below which they will not. At this critical diameter, it is possible that water molecules permeate whereas ions do not. A similar investigation is needed to analyze small organic solutes trans-

port from aqueous solutions, a study which has not been carried out to date. This is important in order to know which organic solutes rejection can be expected from CNTs having a pre-assigned chirality. Thus the first objective of this thesis was a computational investigation in order to provide structures-properties relationships useful to solve this problem: the prediction of the CNTs chirality able to reject low molecular weight compounds was provided. In addition, functionalizing the inlet or the tip of high chirality CNTs with molecules capable of hindering the passage of solutes while allowing water molecules to flow was investigated.

The role of modeling and computer simulations in the design of new membrane materials is important in optimizing the experimental work, particularly in reducing the number of experiments. For example, as described in the section 1.2, one of the most important drawbacks in the membranes processes is the membrane fouling and ageing mainly due to hydrodynamic effects but also to the intrinsic properties of the materials composing membranes (e.g., their surface proprieties). Modeling studies and simulations can be very helpful since they can provide fundamental information to overcome these limitations. The use of titanium bi-oxide, silver and soluble POMs [22] is receiving considerable attention as antibacterial materials. A modeling investigation of the interactions among nanoparticles and polymer functionalities can be useful to identify novel optimal materials with antifouling properties. Thus the second objective of this study was aimed to investigate the adsorption of POMs, regarded as antibacterial particles, on polymeric membrane surface in order to understand if efficient antifouling properties can be conferred to the membrane.

1.4 Methodology and Outline of the thesis

Quantum Mechanics (QM) approaches coupled with bespoke topological algorithms were used in order to achieve the objectives of this thesis. The use of such a approach was adopted mainly in order to be free of adjustable

or fitting parameters that are often necessary when the description of a phenomenon is modeled. Thus the geometry description of the key models involved in this study along with the chemical properties that rule the target systems, such as binding energy or electronic free energy, were all carried out by *ab-initio* approach. A QM approach, although may be characterized by a rather significant computational effort, helps to estimate accurately some molecular chemical properties which are, currently, impossible to assess experimentally and it definitely represents the most reliable method since it does not make use of any adjustable parameter. In particular the here proposed calculations were all performed in the frame of Density Functional Theory (DFT) because of its low computational cost compared with post-Hartree-Fock methods.

Also, the implemented algorithms do not make use of any adjustable parameter being based on QM geometries of the models. Furthermore general algorithms, which are not related for example at the kind of material or operating conditions, were developed leading to the possibility of a wide range of applications. This means that the same methodologies here proposed could be applied to other nano-architectures by changing the input structures. It is also worth pointing that the values obtained by these methodologies can be considered homogeneous overcoming the frequent inconvenience of handling data obtained in different experimental conditions, which makes comparison difficult.

Summarizing, in this thesis mainly three properties of a nano-enhanced membrane were investigated: first, the rejection of low molecular weight compounds by carbon nanotubes in order to understand which kind of CNT is able to reject a given compound. Second, perm-selective properties of the membrane in order to predict the kind of carbon nanotubes that can confer optimal conditions. Third, antifouling properties of a membrane that was performed by modeling the adsorption of antibacterial particles on the membrane surface. The thesis is divided in six chapters as follows:

After giving an overview of the definitions and classifications of nanostruc-

tures with particular regard to their applications in wastewater purification, and after having focused on CNTs and POMs which are the subjects of this study, in chapter 2 a short prologue about theoretical background of the performed calculations is provided. The important role that noncovalent interactions play in supramolecular chemistry is also included.

The chapter 3 contains the details of the development of topological algorithms implemented in this thesis.

Finally, in the chapter 4 the application of the above algorithms is provided in order to describe the structure-properties relationships of Carbon nanotubes. A full discussion about the theoretical knowledge acquired is presented.

The chapter 5 describes the theoretical investigations on the adsorption of antibacterial nanoparticles on a membrane surface. The computational details and results obtained are discussed. A brief reference to an *ad-hoc* experiment that validates the theoretical predictions here achieved is also given.

In chapter 6 the conclusions are reported.

Bibliography

- [1] *National Nanotechnology Initiative 2000 Leading to the Next Industrial Revolution*, A Report by the Interagency Working Group on Nanoscience, Engineering and Technology (Washington DC: Committee on Technology, National Science and Technology Council), <http://www/nano.gov>.
- [2] Guozhong Cao and Ying Wang (2011), *Introduction. Nanostructures and Nanomaterials*, 2nd, pp. 1-17. doi: 10.1142/9789814340571_0001
- [3] H. Gleiter (2000), *Acta Mater.* 48, 1
- [4] Skorokhod V, Ragulya A, Uvarova I. (2001) *Physico-chemical kinetics in nanostructured systems*, Academperiodica, Kyiv, p. 180.
- [5] V.V. Pokropivny , V.V. Skorokhod (2007) *Classification of nanostructures by dimensionality and concept of surface forms engineering in nanomaterial science*, *Materials Science and Engineering C* 27, 990993
- [6] *COMMISSION RECOMMENDATION of 18 October 2011 on the definition of nanomaterial*, Official Journal of the European Union, (2011/696/EU)
- [7] H. Gleiter (1981), *Proc. of the 7th Riso Int. Symposium on Metallurgy and Materials Science*, Roskilde, pp. 1521
- [8] R. Smalley, R. Curl, H. Kroto, Nobel Prize in Chemistry 1996
- [9] Heinrich Rohrer, Gerd Binnig, Nobel Prize in Physics 1985

-
- [10] H. Hahn, (2005) *Unique Features and Properties of Nanostructured Materials*, in *Nanomaterials by Severe Plastic Deformation* (eds M. Zehetbauer and R. Z. Valiev), Wiley-VCH Verlag GmbH & Co. KGaA, Weinheim, FRG. doi: 10.1002/3527602461.ch1a
- [11] George M. Whitesides, Jennah K. Kriebel, and Brian T. Mayers *Self-Assembly and Nanostructured Materials* 9, 217-239
- [12] Jones, W., Rao, C. N. R. & Editors (2002). *Supramolecular Organization and Materials Design* Cambridge University Press: Cambridge, UK.
- [13] Perry, R. H.; Green, D. W. (1997). Eds. Perry's Chemical Engineers' Handbook, 7th ed., McGraw-Hill, New York.
- [14] J. A. Howell, H. C. Chua and T. C. Arnot (2004). *In situ manipulation of critical flux in a submerged membrane bioreactor using variable aeration rates, and effects of membrane history* Journal of Membrane Science Volume 242, Issues 1-2, Pages 13-19.
- [15] Jiang, M.D. Kennedy, W. G.J. van der Meer, P. A. Vanrolleghem, J. C. Schippers, (2003). *The role of blocking and cake filtration in MBR fouling* Desalination Volume 157, Issues 1-3, Pages 335-343.
- [16] A. Srivastava, O.N. Srivastava, S. Talapatra, R. Vajtai, P.M. Ajayan, (2004) *Carbon nanotube filters* Nat. Mat. 3, 610614.
- [17] J. Holt, H. Park, Y. Wang, M. Stadermann, A. Artyukhin, C. Grigoriopoulos, A. Noy, O. Bakajin, (2006) *Fast mass transport through sub-2-nanometer carbon nanotubes* Science 312, 10341037.
- [18] F. Zhu, K. Schulten, (2003) *Water and proton conduction through carbon nanotubes as models for biological channels* Biophys. J. 85, 236244.
- [19] C.D. Vecitis, M.H. Schnoor, M.S. Rahaman, J.D. Schiffman, M. Elimlech, (2011) *Electrochemical multiwalled carbon nanotube filter for vi-*

- ral and bacterial removal and inactivation* Environ. Sci. Technol. 45, 36723679.
- [20] J. Kim, B. Van der Bruggen, (2010) *The use of nanoparticles in polymeric and ceramic membrane structures: review of manufacturing procedures and performance improvement for water treatment* Environ. Pollut. 158, 23352349.
- [21] M.G. Buonomenna, (2013) *Nano-enhanced reverse osmosis membranes* Desalination 314, 7388.
- [22] www.bionexgen.eu
- [23] M. Majumder, N. Chopra, R. Andrews, B.J. Hinds (2005) *Nanoscale hydrodynamics-enhanced flow in carbon nanotubes* Nature 438, 44.
- [24] B. Corry, (2008) *Designing Carbon Nanotube Membranes for Efficient Water Desalination* J. Phys. Chem. B, 112, 1427-1434
- [25] A. Kalra, G. Hummer, S. Garde, (2004) *Methane Partitioning and Transport in Hydrated Carbon Nanotubes* J. Phys. Chem. B, 108, 544-549
- [26] O. Beckstein, M. Sansom, (2004) Phys. Biol. 1, 42-52.
- [27] A. Anishkin, S. Sukharev, (2004) J. Biophys., 86, 2883-2895.
- [28] M. Sotomayor, K. Schulten, (2004) J. Biophys., 87, 3050-3065.
- [29] B. Corry, (2006) Biophys. J., 90, 799-810.

Chapter 2

Theoretical background

2.1 Introduction

The choice of theoretical and computational procedure strictly depends on the target property that need to be assessed. Moreover the definition of structural models is another crucial aspect that has to be considered. Quantum Mechanics (QM) approaches allow the evaluation of chemical-physical quantities that could not have been estimated by experimental tests, or only with remarkable inaccuracy. For example, binding energies, molecular electrostatic properties such as dipole, partial charges and electron density distribution, as well as orbital configurations must be evaluated by QM calculations. In addition QM allows to be free from adjustable or fitting parameters resulting in a general approach. However as above mentioned when computational procedures are used particular attention has to be paid to the structural chemical models. Molecular models are dependent on the properties to be assessed and consequently by the computational procedure. For example QM methods are not applicable to the optimization of macromolecules geometries such as polymers or systems containing thousands of atoms (such as biological systems). Molecular Dynamics (MD) methodologies or Monte Carlo can be used in these cases. However, the MD approaches cannot be used to describe the breaking or/and formation of bonds. Although large structural

models cannot be used in conjunction with accurate QM approaches, such as correlated Hartree-Fock [1], Density Functional Theory (DFT) [2] allows obtaining different electronic properties in a relatively short computational time with respect to the mentioned methods. Thus, this theoretical approach is a powerful tool to investigate large chemical systems at QM level [3]. In this thesis DFT calculations were carried out on systems having large number of atoms (up to 700 atoms), and though sometimes high computational time was required, an accurate evaluation of the energies associated with noncovalent interactions involved in the target systems was achieved. In addition Molecular Mechanics calculations were carried out on flexible molecules in order to have an accurate description of the conformational space. Since the noncovalent interactions play important role on chemical systems analysed in this work, after a brief introduction on the DFT, a section on this kind of interactions will be provided.

2.2 Density Functional Theory

DFT is a relative new quantum theory that allows to replace the complicated N -electron wave function $\Psi(\mathbf{x}_1, \mathbf{x}_2, \dots, \mathbf{x}_N)$ describing a many-electron system and the associated Schrödinger equation by the much simpler electron density $\rho(\mathbf{r})$ and its associated Kohn-Sham equation.

For an isolated N -electron atomic or molecular system in the Born-Oppenheimer nonrelativistic approximation, the time-independent Schrödinger equation is given by:

$$\hat{H}\Psi = E\Psi \quad (2.1)$$

where E is the electronic energy, $\Psi(\mathbf{x}_1, \mathbf{x}_2, \dots, \mathbf{x}_N)$ is the wave function, and \hat{H} is the Hamiltonian operator,

$$\hat{H} = \hat{T} + \hat{V}_{ne} + \hat{V}_{ee} \quad (2.2)$$

where

$$\hat{T} = \sum_{i=1}^N \left(-\frac{1}{2} \nabla_i^2 \right) \quad (2.3)$$

is the kinetic energy operator,

$$\hat{V}_{ne} = \sum_{i=1}^N v(\mathbf{r}_i) \quad (2.4)$$

is the electron-nucleus attraction energy operator in which $v(\mathbf{r}_i) = -\sum_{\alpha} \frac{Z_{\alpha}}{r_{i\alpha}}$ is the ‘external’ potential acting on electron i , the potential due to nuclei of charges Z_{α} , and

$$\hat{V}_{ee} = \sum_{i<j}^N \frac{1}{r_{ij}} \quad (2.5)$$

is the Coulomb electron-electron repulsion energy operator. When a system is in the state Ψ , which may or may not satisfy (2.1), the average of many measurements of the energy is given by the formula

$$E[\Psi] = \frac{\langle \Psi | \hat{H} | \Psi \rangle}{\langle \Psi | \Psi \rangle}. \quad (2.6)$$

In the Hartree-Fock method the N -electron wave function of the system can be approximated by a Slater determinant of N mono electron orbitals depending on the single electron position. The energy of the ground-state is found in agreement with the **variational principle for the ground state** by minimizing the functional (2.6) subject to the orthonormalization conditions of the mono electron orbitals.

The foundation of DFT rests on two theorems by Hohenberg and Kohn that legitimizes the use of electron density $\rho(\mathbf{r})$ as basic variable in place of $\Psi(\mathbf{x}_1, \mathbf{x}_2, \dots, \mathbf{x}_N)$. The first theorem states:

The external potential $v(\mathbf{r})$ is determined, within a trivial additive constant, by the electron density $\rho(\mathbf{r})$.

In the proof of this theorem is shown that a contradiction is achieved if there are two external potentials, $v(\mathbf{r})$ and $v'(\mathbf{r})$ differing by more than a constant, each giving the same $\rho(\mathbf{r})$ for its ground state. Thus $\rho(\mathbf{r})$ determines N by simple quadrature

$$N = N[\rho(\mathbf{r})] = \int \rho(\mathbf{r}) d(\mathbf{r}) \quad (2.7)$$

and $v(\mathbf{r})$ and hence all properties of the ground state such as the total energy. In the second theorem the energy variational principle is provided:

For a trial density $\tilde{\rho}(\mathbf{r})$, such that $\tilde{\rho}(\mathbf{r}) \geq 0$ and $\int \tilde{\rho}(\mathbf{r})d\mathbf{r} = N$, $E_0 \leq E_v[\tilde{\rho}]$.

$E_v[\rho]$ is the DFT energy functional expressed as sum of the kinetic energy and electrons-nuclei and electron-electron potential energy:

$$\begin{aligned} E_v[\rho] &= T[\rho] + V_{ne}[\rho] + V_{ee}[\rho] \\ &= F_{HK}[\rho] + \int \rho(\mathbf{r})v(\mathbf{r})d\mathbf{r} \end{aligned} \quad (2.8)$$

where

$$F_{HK}[\rho] = T[\rho] + V_{ee}[\rho] \quad (2.9)$$

with $V_{ee}[\rho]$ that can be write as sum of the classical repulsion energy, $J[\rho]$, and a nonclassical term

$$V_{ee}[\rho] = J[\rho] + \text{nonclassical term.} \quad (2.10)$$

It is important to observe that $v(\mathbf{r})$ can express the electrons-nuclei interactions as well as any other type of electrostatic potential.

In 1965 Kohn and Sham proposed an ingenious indirect approach to the kinetic functional $T[\rho]$, by setting the problem in such a way as to have an *exact* kinetic-energy component, $T_s[\rho]$, related to an isoelectronic non-interacting system. To obtain the desired separation out of $T_s[\rho]$, (2.9) was rewrite as:

$$F_{HK}[\rho] = T_s[\rho] + J[\rho] + E_{xc}[\rho] \quad (2.11)$$

where

$$E_{xc}[\rho] = T[\rho] - T_s[\rho] + V_{ee}[\rho] - J[\rho]. \quad (2.12)$$

The defined quantity $E_{xc}[\rho]$ is called the *exchange-correlation energy*; it contains the difference between the kinetic energy of interacting system and the kinetic energy of the non-interacting system and the nonclassical part of the $V_{ee}[\rho]$.

Assuming differentiability of $E[\rho]$, the variational principle (second Hohenberg-Kohn theorem) requires that the ground-state density satisfy the stationary principle

$$\delta \left\{ E_v[\rho] - \mu \left[\int \rho(\mathbf{r}) d\mathbf{r} - N \right] \right\} = 0 \quad (2.13)$$

which gives the Euler-Lagrange equation

$$\mu = \frac{\delta E_v[\rho]}{\delta \rho(\mathbf{r})} = v(\mathbf{r}) + \frac{\delta F_{HK}[\rho]}{\delta \rho(\mathbf{r})}. \quad (2.14)$$

It should be noted that the functional F_{HK} depends only on the total number of electrons, N , of the system while $E_v[\rho]$ depends on N and on the external potential $v(\mathbf{r})$; thus by N and $v(\mathbf{r})$ the system is completely described by solving the Euler-Lagrange equation.

A useful procedure to obtain the $\rho(\mathbf{r})$ of the ground state energy was given by Kohn and Sham that did not resolve directly the above Euler-Lagrange equation. Orbitals were introduced in the problem and the electron density $\rho(\mathbf{r})$ was defined through a set of basic functions (atomic orbital basis set, $\phi_j(\mathbf{r})$) [1] as

$$\rho(\mathbf{r}) = \sum_i^N |\psi_i(\mathbf{r})|^2 \quad (2.15)$$

where:

$$\psi_i(\mathbf{r}) = \sum_j^K c_j^i \phi_j(\mathbf{r}), \quad i = 1, \dots, N. \quad (2.16)$$

Again, the variational principle ensures that the minimum of the functional $E_v[\rho]$, but this time in the space of $\phi(\mathbf{r})$, is the best approximation of the ground state energy. The search of this minimum lead to solve the non-linear *Kohn-Sham (KS) orbital equations* [2] :

$$\left[-\frac{1}{2} \nabla^2 + v_{eff}(\mathbf{r}) \right] \psi_i(\mathbf{r}) = \epsilon_i \psi_i(\mathbf{r}) \quad (2.17)$$

$$\begin{aligned} v_{eff}(\mathbf{r}) &= v(\mathbf{r}) + \frac{\delta J[\rho]}{\delta \rho(\mathbf{r})} + \frac{\delta E_{xc}[\rho]}{\delta \rho(\mathbf{r})} \\ &= v(\mathbf{r}) + \int \frac{\rho(\mathbf{r}')}{|\mathbf{r} - \mathbf{r}'|} d\mathbf{r}' + v_{xc}(\mathbf{r}) \end{aligned} \quad (2.18)$$

where $v_{eff}(\mathbf{r})$ is the the effective potential and $v_{xc}(\mathbf{r})$ is the exchange-correlation potential.

The approximations of $F_{HK}[\rho]$ are expressed as a function of the exchange and correlation functional [4, 5, 6]. The form of $E_{xc}[\rho]$ continues to be upgraded although several its approximations have been published. In practical calculations a large basis set is necessary to obtain high accuracy and convergence of the KS equations. Thus, the accuracy and the computational time of a DFT calculation is affected by the level of theory, i.e. by the choice of functional $E_{xc}[\rho]$ and the choice of an appropriate orbital basis set. In addition other points have to be taken into account in the QM calculations. In (2.18) the external potential $v(\mathbf{r})$ depends on the geometrical disposition of the nuclei, considered in fixed positions (Born-Oppenheimer approximation). A specific arrangement of the nuclei defines therefore a particular potential $v(\mathbf{r})$. Nevertheless, it is worth noting that a particular arrangement does not necessarily provide the lowest total energy of the molecular system. Thus, an optimization of the molecular geometry is necessary to find the nuclei arrangement corresponding to the lowest molecular total energy, that is, the minimum. However, in addition to a global minimum, molecular structures may have several local minima (conformational isomers). The research of all the conformational isomers may require high computational time. In this case, the combination of QM methods with other computational approaches should be used. The research of local and global minima is the necessary and first step to obtaining the chemical and physical properties of the system. The external potential $v(\mathbf{r})$ can also be substituted by an effective potential that replaces the core electrons of the atoms constituting the system with an effective electrostatic potential (ECP); in this case only the electrons of the external orbitals are explicitly considered in the calculation [7]. This procedure decreases the computational time and allows to take into account relativistic effects, which are important when transition metals are present in the molecule.

Finally the Coulomb, exchange and correlation potentials, which are the

last two terms in the relation (2.18) can be evaluated by a grid of points or expanding these potentials using another set of functions, called the ‘auxiliary’ basis set. Large atomic orbital basis makes the calculations very time-consuming. Thus, the calculation is faster if auxiliary basis set is used instead of a grid of points to evaluate the Coulomb, exchange and correlation potentials.

Ultimately, all these points should be taken into account during a calculation to optimize both the accuracy and computational effort [3].

2.3 Role of noncovalent bonds

There is a chemical bond between two atoms or groups of atoms when the forces acting between them are strong enough to lead to the formation of an aggregate with sufficient stability to be regarded as an independent species [8]. The amount of energy required to break a bond and produce neutral atoms is called bond energy. Three classes of chemical bonds can basically be considered: atomic bonds (that includes homopolar, covalent, dative and electron delocalized bonds), electrostatic bonds (that includes ionic, dipolar and hydrogen bonds) and metallic bonds. The second class of bond regulates various properties of the nono-systems studied in this thesis thus a their description by means of accurate DFT approaches, was adopted.

Elettrostatic forces play an important role in many chemical systems defining the field of supramolecular chemistry in which the formation of host-guest complexes or supramolecular clusters is regulated from noncovalent forces between molecular fragments (subunits). Noncovalent interactions differ in their energy and for the mechanism of interaction. For example ionic bond results from the attraction of oppositely charged ions. The atoms of metallic elements lose their outer electrons easily, while the atoms of nonmetals tend to gain electrons. The highly stable ions that result retain their individual structures as they approach one another to form a stable supramolecule or crystal. Other types of noncovalent bonds are the result of electrostatic

Table 2.1: Relative strength of intermolecular noncovalent energies

Bond type	Dependence on distance	Energy ($kcal \cdot mol^{-1}$)	Mechanism	Relative Strength
Ion-Ion	$1/r$	60, 84-150	Interaction between net charges	Strong
Cation- π	$1/r^{x>1}$	1.2-19	Coordination bond	Medium-Weak
Hydrogen Bond	-	4-25	Only occurs between hydrogen and highly electronegative atoms	Medium-Weak
Ion-Dipole, DipoleDipole, Elec. long-range interactions	$1/r^3$	3-7	Electr. attraction forces generated between charges of molecules (polar molecules)	Medium-Weak
Dispersion forces	$1/r^6$	0.5-5	Elect. attraction forces caused by instantaneous dipoles (non-polar molecules)	Weak

attraction generated between opposite charges located on molecules containing permanent dipoles. For example, London dispersion force are attractive interaction between two instantaneously induced dipoles arising from temporary instantaneous fluctuation of charge that occur in all the atoms and molecules, even if electrically symmetrical. Also, hydrogen bonding is an electrostatic attraction between two independent polar molecules, i.e., molecules in which the charges are unevenly distributed, usually containing nitrogen, oxygen, or fluorine. These elements have in fact strong electron-attracting power, therefore when a hydrogen atom is located between them serves as a bridge. The hydrogen bond is weaker than the ionic or covalent bonds. Tab. 2.1 summarizes the main noncovalent bonds involved in the formation of supramolecular clusters distinct as ‘weak’, ‘medium-weak’, or ‘strong’, according to their energy values. As aforementioned in this thesis strong and medium-weak noncovalent bonds were investigated.

All these kind of interactions play an important role in chemistry and

physics and, moreover, are of key importance in the bio-disciplines. The structures of liquids, solvation phenomena, molecular crystals, physisorption, the structures of bio-macromolecules such as DNA and proteins, and molecular recognition are only a few phenomena determined by noncovalent interactions. The role of noncovalent interactions in nature was fully recognized only in the last three decades and although several researches on supramolecular chemistry have led to remarkable results, theoretical studies on the influence of hydrogen bonds, van der Waals interactions (dipolar interactions) and dispersion force on the properties of materials used in the membranes preparation is still at an early stage.

In this specific frame, De Luca *et al.* [9] analysed the hydrogen-bonding interactions involved between an amphiphilic modifier (*guest*, N-ethyl-o,p-toluensulfonamide) and polar functional groups of a block (ether/amide) polymer (*host*). Thus, supra-molecular adducts formed by *guest-host* models were defined. Calculations in solvent and in vacuum were done, yielding indications about the change in the availability of the polar groups of the polymer, which is considered to be partially responsible for the enhanced hydrophilicity of the membranes. Moreover, in Ref. [10] De Luca *et al.* performed QM calculations and experiments to understand the physical-chemical causes of the affinity increase in imprinted polymeric membranes to 4,4'-methylenedianiline (MDA), dissolved in an organic solvent. They showed that the hydrogen bonds and electrostatic interactions among polymeric chains are comparable to the strength of the same interactions occurring between polymer and MDA, concluding that one of the causes responsible for the increased affinity of the imprinted membranes is the augmented availability of free carboxylic groups in the nanocavities of the membranes once the template molecule is removed.

Therefore, in the wake of these research, a QM study on supra-molecular adducts formed by Tyrosol molecules-CNT was carried out in this thesis in addition to the investigation of the interactions ruling the adsorption of POMs on a membrane surface. In particular, as in the just cited papers, the calculation of binding energies related to noncovalent interactions were carried out.

Bibliography

- [1] A. Szabo and N. Ostlund (1994) *Modern Quantum Chemistry Introduction to Advanced Electronic Structure Theory* London , Macmillan Publishing CO. INC , Collier Macmillan Publishers.
- [2] R. G. Parr and W. Yang (1989) *Density Functional Theory of Atoms and Molecules* Oxford , Clarendon Press , New York, Oxford University Press.
- [3] G. De Luca (2013) *Assessment of the key properties of materials used in membrane reactors by quantum computational approaches* Handbook of membrane reactors, Woodhead Publishing Limited, 17, 598-626
- [4] A. D. Becke (1993) *Density-functional thermochemistry. III. The role of exact exchange* J. Chem. Phys., 98, 5648
- [5] J. P. Perdew, K. Burke and M. Ernzerhof (1997) *Generalized gradient approximation made simple* Phys. Rev. Lett., 78, 1396 .
- [6] X. Xu and W.A. Goddard (2004) *The X3LYP extended density functional for accurate descriptions of nonbond interactions, spin states, and thermochemical properties* PNAS, 101(9), 2673-2677.
- [7] F. Pacios and P.A. Christiansen (1985) *Ab initio relativistic effective potentials with spin-orbit operators. I. Li through Ar* J. Chem. Phys., 82, 2664 2671
- [8] L. Pauling (1954) Nobel Prize
- [9] G. De Luca, A. Gugliuzza E. and Drioli (2009) *Competitive hydrogen-bonding interactions in modified polymer membranes: a Density Functional Theory investigation* J. Phys. Chem. B, 113, 5473-5477.

- [10] G. De Luca, L. Donato, S. G. Del Blanco, F. Tasselli and E. Drioli (2011)
On the cause of controlling affinity to small molecules of imprinted polymeric membranes prepared by noncovalent approach: a computational and experimental investigation J. Phys. Chem. B, 115, 9345-9351

Chapter 3

Implemented algorithms

Some algorithm was implemented in order to model the property-structure relationships investigated in this thesis. In particular in the first part of the section an algorithm for building models of zig-zag CNTs was developed. In addition, an algorithm was developed in order to define the main sizes of compounds. In the second part of the section the modeling of the molecular sieving mechanism by functionalized CNT was dealt. The algorithms described below were all implemented using MATrix LABoratory environment [1].

3.1 Zigzag carbon nanotubes

A single-wall carbon nanotube (SWNT) can be described as a graphene sheet rolled into a cylindrical shape with a diameter of about 0.7-10.0 nm. Neglecting the two ends of a carbon nanotube (CNT), an open-ended CNT characterized by a large aspect ratio of the cylinder (i.e., length/diameter which can be as large as $10^4 - 10^5$) is obtained. It is a 1D nanostructure with axial symmetry, and in general exhibiting a spiral conformation, called *chirality*. The chirality is given by a single vector called the “chiral vector” and indicated with $C_h \equiv (n, m)$ where n, m are integers with $0 \leq |m| \leq n$. To specify the structure of CNTs, various vectors were defined from the chiral vector as described in Ref. [2]. The structure of a CNT is characterized by the orientation of the six-membered carbon ring (a hexagon) in the honeycomb lattice relative to the axis of the nanotube. The direction of the six-membered ring in the honeycomb lattice can be taken almost

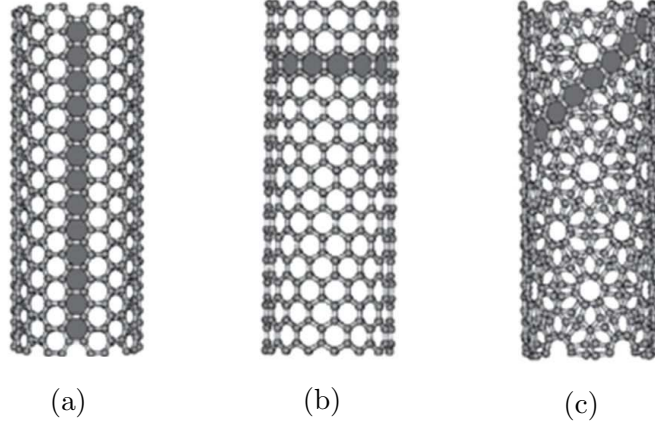


Figure 3.1: Classification of carbon nanotubes: (a) armchair, (b) zigzag and (c) chiral nanotubes.

arbitrarily, without any distortion of the hexagons except for the distortion due to the curvature of the CNT. This fact provides many possible CNTs structures, even though the basic shape of the CNT wall is a cylinder.

The primary symmetry classification is either being achiral or chiral. An achiral CNT is defined by a carbon nanotube whose mirror image has an identical structure of the original one. There are only two cases of achiral nanotubes; armchair that corresponds to the case of $n = m$, and zigzag nanotubes that corresponds to the case of $m = 0$. The name of armchair and zigzag arise from the shape of the cross-sectional ring, as is shown at the edge of the nanotubes in Fig. 3.1a and 3.1b, respectively. All other (n, m) chiral vectors corresponds to chiral nanotubes, shown in Fig. 3.1c, that exhibit a spiral symmetry whose mirror image cannot be superposed on the original one. The diameter of a carbon nanotube, d_{CNT} , is given by L/π , in which L is the circumferential length of the CNT:

$$d_{CNT} = L/\pi, \quad L = |C_h| = \sqrt{C_h \cdot C_h} = a\sqrt{n^2 + m^2 + nm} \quad (3.1)$$

where $a = 1.44\text{\AA} \times \sqrt{3} = 2.49\text{\AA}$ is a lattice constant of the honeycomb lattice.

We have thus a variety of geometries in CNTs with diameter and chirality. The existence of many kind of nanotubes in various samples has also been confirmed experimentally, nevertheless a geometrically homogeneous macroscopic sample of any carbon nanotube has not been produced yet since details of their structural parameters are not well known. Although all bonds should be equivalent in a

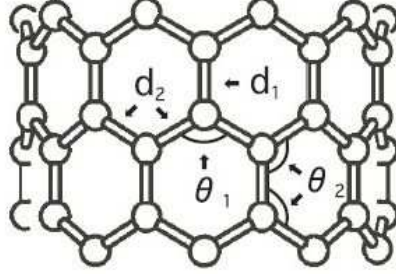


Figure 3.2: Two kinds of bonds and angles in zigzag nanotube, [3]

graphene sheet, not all the bonds are equivalent in carbon nanotubes; there are two or three kinds of bonds in each nanotube. Fig. 3.2 shows two kind of bond lengths, d_1 and d_2 and two kind of bond angles, θ_1, θ_2 found for a zigzag CNT. However, due to the lack of the crystalline sample of structurally uniform carbon nanotubes, their bond lengths and other structural parameters have not been reported experimentally. The only experimental information about their geometries have been given by the Scanning Tunneling Microscopy measurements, which are enough to discuss the chirality of each nanotube but are not sufficient enough to discuss the details of the bond lengths. Some theoretical study [3, 4] was made in order to investigate the curvature effects on structural parameters of nanotubes such as bond lengths and bond angles by fully optimized geometries. These studies pointed out that the curvature effects become significant at small radii. Thus, since the first step of this study was the building of reliable CNTs models, an algorithm generating the coordinates of a $(n, 0)$ carbon nanotube was implemented on the reference of Kanamitsu and Saito [3].

If the diameter of CNT (d_{CNT}) is known, the bond lengths d_1, d_2 and bond angles θ_1, θ_2 can be calculated [3] as:

$$\begin{aligned}
 d_1 &= d_0 + s_1 \left(\frac{1}{d_{CNT}^2} \right) \\
 d_2 &= d_0 + s_2 \left(\frac{1}{d_{CNT}^2} \right) \\
 \theta_1 &= \theta_0 + t_1 \left(\frac{1}{d_{CNT}^2} \right) \\
 \theta_2 &= \theta_0 + t_2 \left(\frac{1}{d_{CNT}^2} \right)
 \end{aligned} \tag{3.2}$$

where $s_1 = -0.320 \text{ \AA}^3$, $s_2 = 0.427 \text{ \AA}^3$, $t_1 = -147.12^\circ \text{ \AA}^2$, $t_2 = 1.18^\circ \text{ \AA}^2$, and where

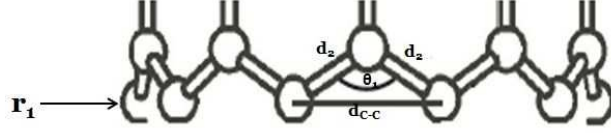
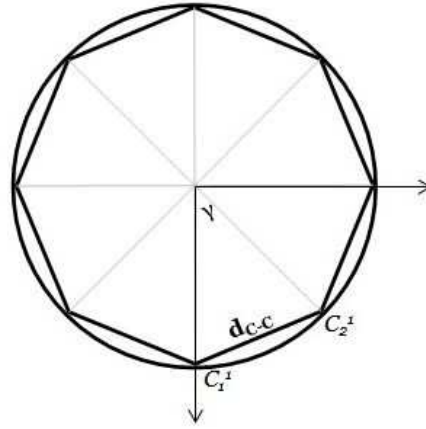


Figure 3.3: row of carbon atoms

Figure 3.4: first row of carbon atoms like a n -sided regular polygon

$d_0 = 1.406\text{\AA}$ and $\theta_0 = 120^\circ$ are the optimized bond length and angle of graphene. The algorithm implemented was developed in such a way that the differences $d_1 - d_0$, $d_2 - d_0$ and bond angles depending on the CNT diameter follow the trend reported in Ref. [3]. In particular the structure of the zig-zag CNT is built row by row. Let r_1 be a circle row of carbon atoms of a $(n, 0)$ CNT as shown in Fig. 3.3. r_1 consists of n atoms away from each other of a d_{C-C} distance that can be found as function of d_2 and θ_1 :

$$d_{C-C} = 2d_2 \sin\left(\frac{\theta_1}{2}\right). \quad (3.3)$$

Thus the first circle row can be outlined as a n -sided regular polygon (Fig. 3.4) centred in a cartesian plane and having sides equal to d_{C-C} and central angles equal to

$$\gamma = 2 \arcsin\left(\frac{d_{C-C}}{d_{CNT}}\right) \quad (3.4)$$

Since n must be an integer number, d_{CNT} can be adjusted and therefore exactly defined. Denoted with C_1^1, \dots, C_n^1 the n vertices of the regular polygon, their

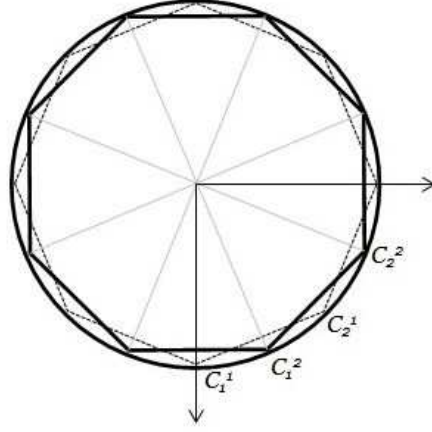
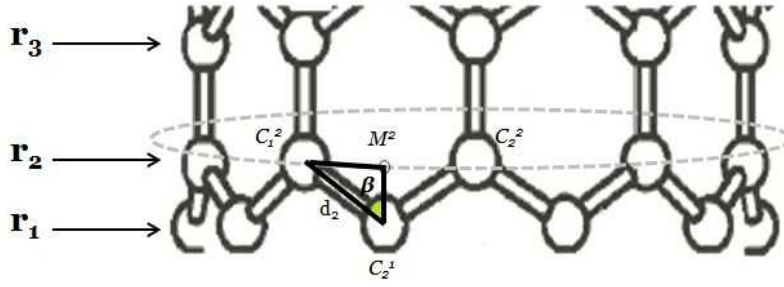


Figure 3.5: second row of carbon atoms

Figure 3.6: representation for the calculation of the z -coordinates

coordinates are given by:

$$C_k^1 = \left(x_k^1(d_{CNT}, \gamma), y_k^1(d_{CNT}, \gamma), 0 \right) \quad k = 1, \dots, n \quad (3.5)$$

thus the first row of the CNT is built.

The coordinates of each atom of the next r_2 row can be determined from the position of the carbon atoms of r_1 just calculated. In fact, the projections of the r_2 points on the plane of r_1 will form another equal n -sides regular polygon but with the first vertex C_1^2 rotated of $\gamma/2$ than C_1^1 (Fig. 3.5).

In addition, the z -coordinates of these points can be found by focusing on the triangle formed between r_1 and r_2 ; let's consider for example $C_2^1 C_1^2 M^2$ as shown in (Fig. 3.6).

With M^2 was denoted the point obtained moving of a $\gamma/2$ angle the point C_1^2

on the circle row r_2 . The β angle shown in figure is given by:

$$\beta = \arcsin\left(\frac{\overline{C_1^2 M^2}}{d_2}\right) \quad (3.6)$$

where from the Carnot Theorem

$$\overline{C_1^2 M^2} = \sqrt{\frac{d_{CNT}^2}{2} \left(1 - \cos\left(\frac{\gamma}{2}\right)\right)} \quad (3.7)$$

Thus is possible to evaluate the z - coordinates of the r_2 points compared to r_1 points:

$$\overline{C_2^1 M^2} \equiv \Delta z = d_2 \cos \beta. \quad (3.8)$$

Finally, the coordinates of r_2 atoms will be:

$$C_k^2 = \left(x_k^2(d_{CNT}, \gamma), y_k^2(d_{CNT}, \gamma), \Delta z\right) \quad k = 1, \dots, n \quad (3.9)$$

Similarly, the carbon atoms of all the other rows will be obtained properly repeating the x and y coordinates of r_1 or r_2 rows and considering as z -coordinates for each new row that of the previous one properly increased either of d_1 or Δz . In this way a $(n, 0)$ CNT with a required length can be built. The differences $d_1 - d_0$, $d_2 - d_0$ and bond angles depending on the CNT diameter will follow the trend reported in Ref. [3]. The curvature effects become significant at small radii. For a CNT with a diameter upper to 1 nm the bond lengths d_1 and d_2 approach the optimized bond length of graphene, d_0 , and the bond angles approach the ideal bond angle θ_0 . As result, the use of this algorithm makes sense for building reliable models of small CNTs. For larger CNTs the models used in this work are built by the Saito algorithm reported in Ref. [2].

3.2 Molecular topological analysis

The description of the molecular sizes of organic compounds is widely discussed and treated since sizes are fundamental molecular features for the modelling of the compounds retention by means of nano-porous membranes. The morphology of the molecules is especially important when the size of the pores are comparable with those of the molecules to be rejected. In these cases in fact steric hindrance may be the driving factor in the rejection of molecules. The approximation of

the molecular shape in a spherical one, by effective diameters empirically defined, can lead to errors. Thus the molecular morphology is the starting point for a systematic study of the rejection of small solutes which is the aim of this thesis.

The most easily accessible parameter that describes the size of a molecule is the molecular weight but it does not provide accurate information on the rejection of molecules. In fact although empirical correlations and sizes are available for some class of compounds, they have not general validity and normally are only valid for molecules of large size. In several studies molecular size parameters such as molecular width, Stokes radii, and molecular mean size have been shown to be a better descriptor of the steric hindrance in Nano Filtration membranes than weight [5, 6, 7, 8, 9, 10].

The Stokes radius is a commonly used descriptor for the evaluation of the molecular steric hindrance, however the diffusivities to estimate Stokes radius cannot be obtained for many organic solutes [8]. In addition, the Stokes radius is based on the assumption that molecules are spherical in shape and rigid, which is not always correct [7]. Because Stokes radii can be difficult to measure for some molecules, other molecular sizes have been developed to take into account the molecular geometry effect on the solute rejection [8, 11, 12, 13, 14].

In the footsteps of aforementioned works, an algorithm able to provide the molecular sizes of a given compound only starting from its molecular geometry is implemented. The molecular descriptor was obtained only using the *ab-initio* optimized geometry of each involved solute. *Ab-initio* calculation requires only the knowledge of the chemical formula and allows to be free from empirical or fitting parameters. In addition *ab-initio* calculations take into account the molecular non-covalent intra and intermolecular interactions that can significantly modify the molecular structures of the compounds and as result their molecular size.

In detail, the implemented algorithm is developed as follows: starting from a molecular structure reliably described by Quantum mechanics calculations (in molecules with a large number of rotamers a preliminary search of the most stable conformer is performed), each atom is represented by a hard sphere having radius equal to the vdW radius. Three main dimensions are defined: the height H , d_{min} and d_{max} dimensions. A 3D-Cartesian coordinate system is fixed in such a way that the origin of the Cartesian axes match the geometric center of the molecule

and that the z -axis is parallel to the straight line connecting the two most distant atoms in the structure. The van der Waals radii are taken into account in this evaluation. The height H is defined as the distance between the two farthest atoms. The molecule is now projected on a plane perpendicular to the z -axis and the problem to define the most proper geometric form that includes these projections is analyzed. This geometric form will describe the minimum cross section (MCS) of the molecule. Braeken et al. [14] determined around the projected molecule a circle with minimum area. Basically, the determination of this circle refers to the 'Smallest Enclosing Circle Problem' treated in computational geometry and whose solution is not trivial:

Given a set of circles $C = \{c_1, \dots, c_n\}$ on the Euclidean plane with centers $\{(a_1, b_1), \dots, (a_n, b_n)\}$ and radii $\{r_1, \dots, r_n\}$, the smallest enclosing circle (of fixed circles) problem is to find the circle of minimum radius that encloses all circles in C .

Most algorithms discussed in the literature [15, 16, 17] consider only the special case of enclosing points, namely the case in which the radii are equal to zero although several approaches are also proposed for the general cases where at least one circle has non-zero radius [18]. Thus a good description of the solution of the Smallest Enclosing Circle Problem should follow these studies.

However the circle that includes the atoms projections could overestimate MCS, as for example in the case of 'flat' molecules. Fig. 3.7 shows two different dispositions of the atom projections. In both cases, the smallest enclosing circle (in blue colour) and the smallest enclosing rectangle (in green colour) around the projected atoms were delineated. Fig. 3.7a, describing the disposition of the atom projections aspected in the case of flat molecules, shows that MCS is overestimated if the circle is considered.

Thus, based on this consideration, a description of the molecular MCS by means of the Smallest Enclosing Rectangle is adopted in the algorithm implemented in this thesis.

Given a set of circles $C = \{c_1, \dots, c_n\}$ on the Euclidean plane with centers $\{(a_1, b_1), \dots, (a_n, b_n)\}$ and radii $\{r_1, \dots, r_n\}$, find the rectangle of minimum area that encloses all circles in C .

In order to solve this problem the following algorithm is here proposed:

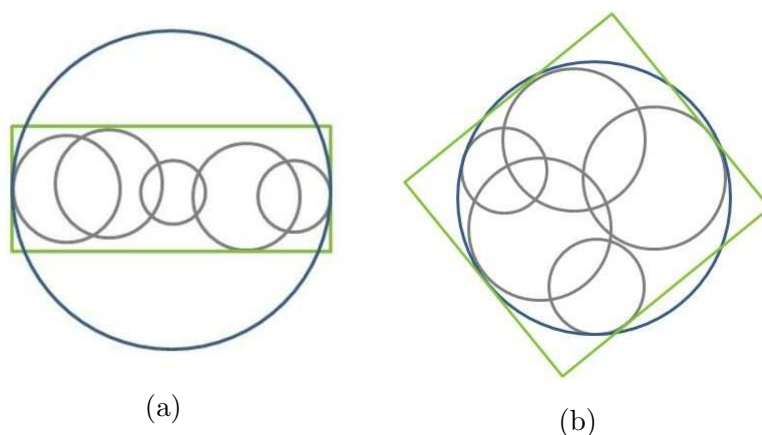


Figure 3.7: Smallest enclosing rectangle and smallest enclosing circle in two limit cases

Step 1: Compute the rectangle of minimum area having sides parallel to the cartesian axis;

for each $c_i \in C$, $i = 1, \dots, n$, four coordinates were identified allowing to define the vertices of the searched rectangle and consequently its sides.

Step 2: Apply a counterclockwise rotation of the cartesian plane through a given angle about its center and go back to step 1.

This procedure is sequentially applied for different angles in such a way that the whole interval $[0, \pi/2]$ is scanned. Fig. 3.8 shows the procedure applied for 0 , $\pi/6$ and $\pi/3$.

Among all rectangles searched the minimum area rectangle is finally provided as MCS and the sides of related rectangle are denoted with d_{min} and d_{max} .

These molecular characteristic sizes can then used in order to calculate a molecular effective diameter that is an average size taking into account the different molecule's orientations when approaching to membrane surface [14]. If the axis of the molecule (z -axis) is supposed to make an angle α with the membrane surface (Fig. 3.9), the height in projection (H') can be evaluated as

$$H' = H \cos(\alpha) + d_{max} \sin(\alpha). \quad (3.10)$$

The effective diameter (d_{eff}) can therefore be obtained assuming that the probability distribution of α is equal to $\cos(\alpha)$. As a result, the effective diameter can

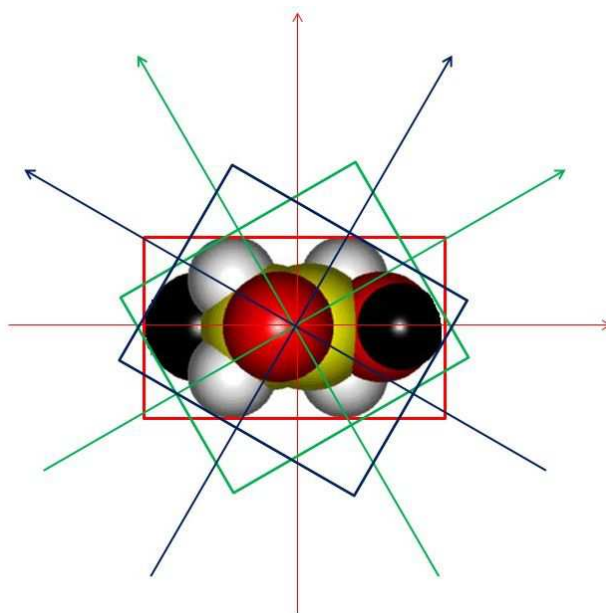


Figure 3.8: Procedure applied for 0 (in red) $\pi/6$ (in green) and $\pi/3$ (in blue)

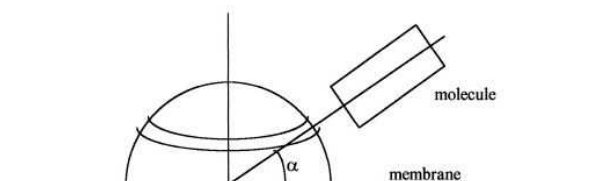


Figure 3.9: Probability distribution for the angle α between the molecule and the membrane, [19].

be calculated as

$$d_{eff} = \frac{\pi}{4}H + \frac{1}{2}d_{max}. \quad (3.11)$$

This algorithm was used in order to calculate the characteristic sizes of 12 organic solvents for a purpose other than that of this thesis but in which, however, the molecular sizes play an important role. Precisely, in paper [20] in order to take into account the non-spherical character of the solvents and overcome the lack in literature of the kinetic diameter for all considered solvents, the above defined sizes were used. In Tab. 3.1 are listed the calculated d_{min} and d_{eff} for some of the solvents along with their kinetic diameters, d_{kin} , taken from different publications [21, 22, 23]. It is clearly shown that d_{eff} calculated by means of the algorithm

Table 3.1: Comparison between molecular sizes

Molecules	$d_{eff}(nm)$	$d_{min}(nm)$	$d_{kin}(nm)^*$
Water	0.47	0.28	0.27
Methanol	0.62	0.42	0.38
Ethanol	0.74	0.42	0.44
Dichloromethane	0.73	0.42	0.49
Dimethylformamide	0.84	0.43	0.50
Toluene	0.98	0.43	0.55
Hexane	1.08	0.42	0.51

developed in this thesis is greater than d_{kin} contrary to d_{min} which is found to be very similar. Should be stressed that d_{kin} is widely used when molecular rejection is studied and that the general algorithm developed here allows to have a similar size obtained in a homogeneous way and without use empirical parameters.

3.3 Pore molecular sieving

3.3.1 Maximun free area and Molecular permeation area

Maximun free area (MFA) algorithm is used in order to evaluate the free area, $A_{CNT,free}$, of a CNT inlet after that more functional groups (FGs) are anchored on its edge. However MFA algorithm is developed in a general way and therefore it is applicable to any nano-pore with defined profile. In particular concerning the aim of the thesis, in which the ability of a CNT to reject small compounds without losing in water flux is investigated, MFA algorithm will be illustrated considering as reference the CNT that actually can be regarded as an ideal pore due to the well defined shape of its inlet.

In detail, the atoms of the FGs will be treated as a set of rigid spheres having as radii the vdW radii. A 3D -Cartesian coordinate system is fixed in such a way that the origin of the Cartesian axes match the center of the CNT inlet while the z -axis is along the CNT axis. A points grid is built on the inlet of a CNT: the

*Experimental data from literature

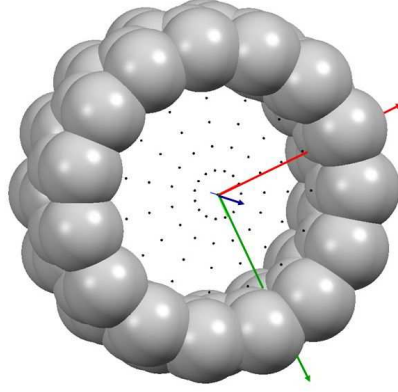


Figure 3.10: Points grid building on the CNT inlet.

i -th point on the plane $z = 0$ is determined by a Δr_i radial coordinate and an $\Delta \vartheta_i$ angular coordinate. The radius of the CNT and the center angle, 2π , are divided in an n and m integer numbers that will define the grid spacing. In the grid building the edge of the CNT is taken into account in fact the grid is built on the disk $D(0, r_s)$ centred in $(0, 0)$ and having radius $r_s = r_{CNT} - r_C$, where r_C is the vdW radius of a carbon atom. The figure 3.10 shows the points grid built on the CNT inlet in the $3D$ -Cartesian coordinate system.

The anchored FGs, whose optimised geometries were carried out at quantum level, will cover part of the CNT inlet. In order to calculate the covered portion, the projections of the FGs are considered on the $z = 0$ plane. The projections of FGs atoms are the $D_p((x_s, y_s), r_{vdW})$ disks of center equal to the (x_s, y_s) and radius equal to the vdW radius of the atoms. The following geometric problem was considered:

Problem 3.3.1. *Let G be a circular points grid in a Cartesian plane having Δr and $\Delta \vartheta$ as radial and angular spacing and let $\{D_p(c_p, r_p), p = 1, \dots, N\}$ be a set of disks whose intersections are not necessarily empty. Find the grid portion covered by disks and evaluate its area.*

Let ‘0’ a label by which any point of the starting grid is characterized. A grid point (x_G, y_G) will be covered by $D_p(c_p, r_p)$ if $(x_G, y_G) \in D_p(c_p, r_p)$, that is if

$$(x_G - x_p)^2 + (y_G - y_p)^2 \leq r_p^2 \quad (3.12)$$

with $c_p \equiv (x_p, y_p)$.

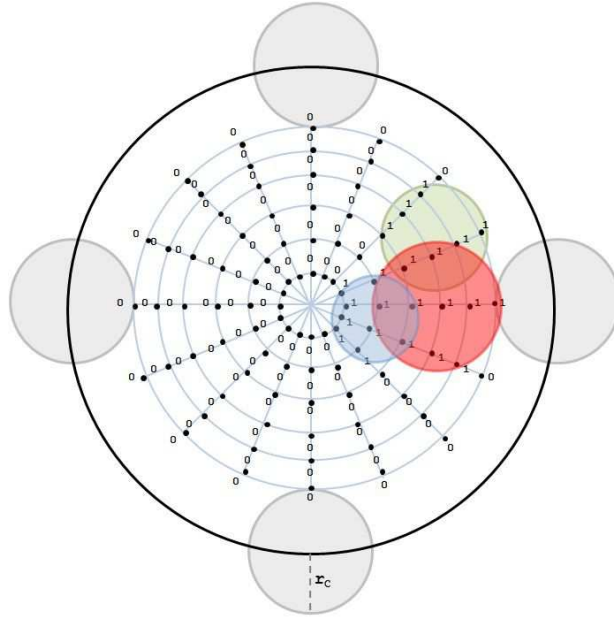


Figure 3.11: Points grid marked with free and covered points

Thus, given p , \forall grid point, if the equation (3.12) is satisfied the label of that point will become '1'. This check will be done $\forall p$, with $p = 1, \dots, N$ and as result the points grid will be characterized by '0' labels, that will indicate 'free' points, and by '1' labels, that will indicate 'covered' points. The Fig. 3.11 shows an example of some disk covering part of a points grid.

On the basis of the grid defined, the CNT inlet can be decomposed into circular (C_s) and annular sectors (A_s) shown in Fig. 3.12.

Thus in order to evaluate the area of grid portion covered by disks, the area

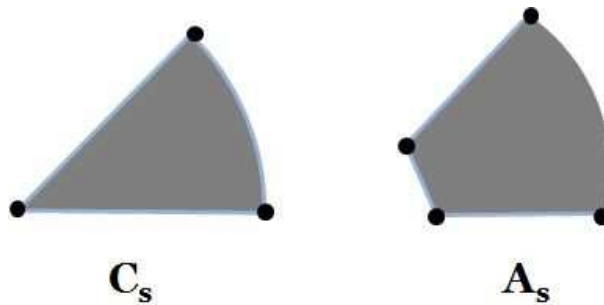


Figure 3.12: Sectors forming the CNT inlet

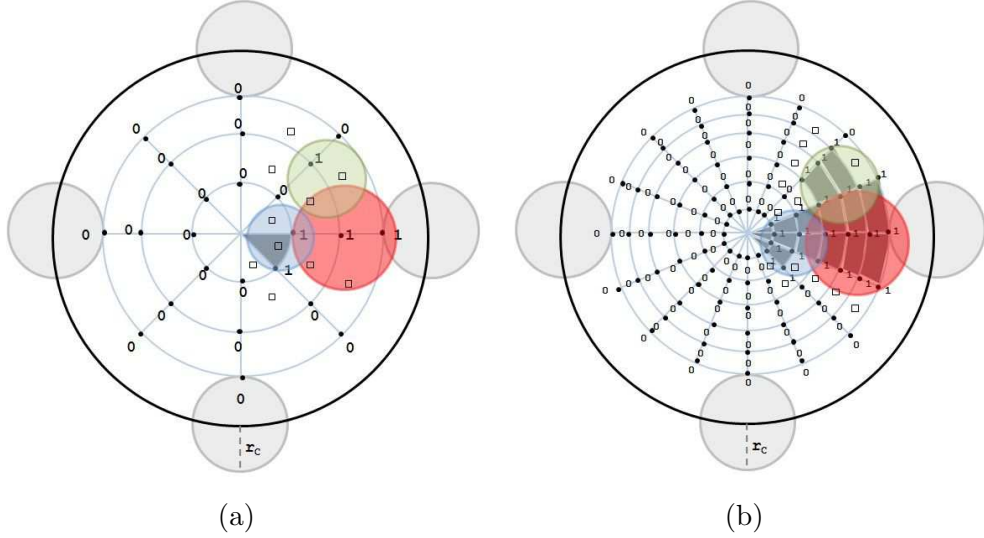


Figure 3.13: Points grid with (a) a large spacing and (b) a tighter spacing. Covered sectors are shown in grey.

of covered sectors was evaluated. In particular a sector was considered 'covered' when all its vertices are labelled with '1'.

The covered area is therefore given by:

$$A_c = \alpha C_s + \sum_{\beta} A_s^{\beta} \quad (3.13)$$

where

$$C_s = \frac{1}{2} \Delta r^2 \Delta \vartheta$$

$$A_s^{\beta} = \pi \frac{((r^{\beta} + \Delta r)^2 - (r^{\beta})^2)}{m} \quad (3.14)$$

are respectively the area of a covered circular sector and the area of a covered annular sector having internal radius equal to r^{β} .

Should be noted that tighter the grid spacing is, the smaller the error got on the covered area is. The Fig. 3.13 provides an illustration of this concept.

By solving the problem (3.3.1), the portion of area covered by anchored FGs on the CNT inlet can therefore be evaluated and consequently also $A_{CNT,free}$. The last in fact can be evaluated like difference between the known area of a CNT inlet without FGs and the just evaluated A_c .

The rejection mechanism through molecular sieving by functionalised nanopore is investigated here as a geometrical problem thus hereinafter an algorithm for the evaluation of the ‘molecular permeation area’, $A_{mol,perm}$, of a target molecule through a functionalized CNT is developed. Precisely, $A_{mol,perm}$ is the area through which the permeation of a molecule can occur without steric hindrance due to the CNT edge or/and anchored FGs. It is crucial to note that $A_{mol,perm}$ changes by varying $A_{CNT,free}$. In fact, the former depends both on the MCS of the molecule (sec. 3.2) and on above evaluated $A_{CNT,free}$, while the last only depends on the steric hindrance of the FGs. A simple example can illustrate this difference: two molecules with different MCS will permeate in a different way through $A_{CNT,free}$, i.e. the molecule with smaller MCS will permeate more easily.

Therefore, the algorithm is based both on the sizes of the molecule to be rejected and on the steric hindrance that FGs form on the CNT inlet. The following assumptions are done:

1. the molecule is represented with its MCS (see 3.2) and the CNT inlet with a disk whose size is defined by the CNT internal diameter. The choice of MCS was made since the steric hindrance of a molecule is minimal if the molecule is placed in the MCS disposition [24]. The validity of this assumption will be clear in sec. 4.1.2.
2. the area of CNT inlet covered by functional groups is not accessible to the molecule. In other terms the molecule is rejected when, placed according its MCS, it touches a covered grid point (‘1’ point) or the CNT edge.

Finding $A_{mol,perm}$ can be regarded as the geometrical problem of estimating the area of a complicated object lying in a known area as shown in Fig. 3.14a. Thus it was evaluated following a Monte Carlo approach [25, 26] generally used in estimating the area of an irregular object (Fig. 3.14a). This procedure was applied to the case study here analysed, in which the known area is $A_{CNT,free}$. In Fig. 3.14b a top view of a functionalized CNT is shown in which the covered area by two anchored functional groups is indicated in black color; in green and blue color the $A_{CNT,free}$ and $A_{mol,perm}$ are respectively reported.

In particular in order to evaluate $A_{mol,perm}$ the following algorithm was adopted: starting from a known number of points located in the green area, it is checked if a

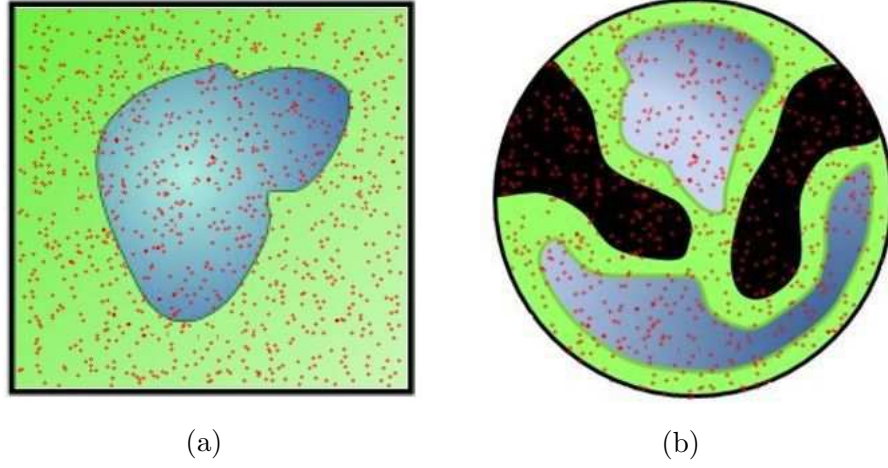


Figure 3.14: Finding an area of non regular 2D-object by using the Monte Carlo method applied in (a) a general case (b) order to find $A_{mol,perm}$

test point is inside or outside the boundary of the blue area (Fig. 3.14b). In other terms it is checked if a test point belongs to $\sigma_{mol,perm}$ or belongs to $\sigma_{CNT,free}$, with

$$\begin{aligned} \sigma_{mol,perm} &= \{p_{mol,perm} \in CNT \text{ inlet s. t. } p_{mol,perm} \text{ is a grid point} \\ &\quad \text{in which the molecule is not rejected}\} \\ \sigma_{CNT,free} &= \{p_{CNT,free} \in CNT \text{ inlet s. t. } p_{CNT,free} \text{ is a grid point} \\ &\quad \text{in which the molecule can or can not be rejected (above defined as '0' points)}\}. \end{aligned} \quad (3.15)$$

The ratio between $A_{mol,perm}$ and $A_{CNT,free}$ is equal to the ratio of number of elements of the sets $\sigma_{mol,perm}$ and $\sigma_{CNT,free}$:

$$\frac{A_{mol,perm}}{A_{CNT,free}} = \frac{|\sigma_{mol,perm}|}{|\sigma_{CNT,free}|} \quad (3.16)$$

Therefore, $A_{mol,perm}$ is evaluated as follow:

$$A_{mol,perm} = A_{CNT,free} \cdot \frac{|\sigma_{mol,perm}|}{|\sigma_{CNT,free}|}. \quad (3.17)$$

The details of the procedure adopted in order to define the points belonging to $\sigma_{mol,perm}$ are reported in annex A. The points belonging to $\sigma_{CNT,free}$ are instead the points labelled with '0' during the algorithm used to calculate $A_{CNT,free}$.

It is important noting that the accuracy of the Monte Carlo methods increases with increasing the number of test points and when a good random number generator, that allows to evenly cover the entire area, is used. This can be guaranteed by choosing a tight grid of points.

Bibliography

- [1] MATLAB and Statistics Toolbox Release 2012b, The MathWorks, Inc., Natick, Massachusetts, United States
- [2] R. Saito, G. Dresselhaus, M. S. Dresselhaus (1998) *Physical Properties of Carbon Nanotubes* Imperial College Press
- [3] K. Kanamitsu and S. Saito (2002) *Geometries, Electronic Properties, and Energetics of Isolated Single Walled Carbon Nanotubes* J. Phys. Soc. Jpn., Vol. 71, No. 2
- [4] O. Gulseren, T. Yildirim, and S. Ciraci (2002) *Systematic ab initio study of curvature effects in carbon nanotubes* Physical Review B 65 153405
- [5] H. Ozaki, H. Li (2002) *Rejection of organic compounds by ultralow pressure reverse osmosis membrane* Water Res., 36(1), 12330
- [6] P. Berg, G. Hagemeyer, R. Gimbel (1997) *Removal of pesticides and other micro-pollutants by nanofiltration* Desalination, 113, 2058.
- [7] Y. Kiso, T. Kitao, J. Kiyokatsu, M. Miyagi(1992) *The effects of molecular width on permeation of organic solute through cellulose acetate reverse osmosis membrane* J. Membr. Sci. 74(12), 95103
- [8] Y. Kiso, T.Kon, T. Kitao, K. Nishimura (2001) J. Membr. Sci. 182, 20514.
- [9] B. Van der Bruggen, J. Schaep, D. Wilms, C. Vandecasteele (1999) *Influence of molecular size, polarity and charge on the retention of organic molecules by nanofiltration* J. Membr. Sci. 156, 2941

-
- [10] B. Van der Bruggen, J. Schaep, W. Maes, D. Wilms, C. Vandecasteele (1998) *Nanofiltration as a treatment method for the removal of pesticides from ground waters* Desalination, 117-139.
- [11] K. O. Agenson, J.-I. Oh, T. Urase (2003) *Retention of a wide variety of organic pollutants by different nanofiltration/reverse osmosis membranes: controlling parameters of process* J. Membr. Sci. 225, 91103
- [12] V. Yangali-Quintanilla, A. Sadmani, M. McConville, M. Kennedy, Gary Amy (2010) *A QSAR model for predicting rejection of emerging contaminants (pharmaceuticals, endocrine disruptors) by nanofiltration membranes* Water Res. 44, 373-384
- [13] J.L.C. Santos, P. de Beukelaar, I. F.J.Vankelecom, S. Velizarov, J. G. Crespo (2006) *Effect of solute geometry and orientation on the rejection of uncharged compounds by nanofiltration* Separation and Purification Technology 50, 122131
- [14] L. Braeken, R. Ramaekers, Y. Zhang, G. Maes, B. Van der Bruggen, C. Vandecasteele (2005) *Influence of hydrophobicity on retention in nanofiltration of aqueous solutions containing organic compounds* J. Membr. Sci. 252, 195203
- [15] P. Chrystal, (1885) *On the problem to construct the minimum circle enclosing n given points in a plane* Proceedings of the Edinburgh Mathematical Society, Third Meeting, p.30.
- [16] J. Eliosoff, and R. Unger (1998) *Minimal spanning circle of a set of points* Computer Science 308-507: Computational Geometry project, school of computer science, McGill University
- [17] D.W. Hearn, and J. Vujan (1982) *Efficient algorithms for the minimum circle problem* Oper. Res.,30, 777-795
- [18] S. Xu , R. M. Freund , J. Sun (2001) *Solution methodologies for the smallest enclosing circle problem* Technical report, Singapore-MIT Alliance, National University of Singapore, Singapore

-
- [19] B. Van Der Bruggen, J. Schaep, D. Wilms, and C. Vandecasteele (2000) *A Comparison of Models to Describe the Maximal Retention of Organic Molecules in Nanofiltration* Separation Science and Technology, 35(2), pp. 169182
- [20] A. Buekenhoudt, F. Bisignano, G. DeLuca, P. Vandezande, M. Wouters, K. Verhulst (2013) *Unravelling the solvent flux behaviour of ceramic nanofiltration and ultrafiltration membranes* J. Membr. Sci. 439, 3647
- [21] A. Ilyas, M. Eic, M. H. Zahedi-Niaki, S. Vasenkov (2007) *Toward observation of single file diffusion using TZLC* Diffus. Fundam. 6, 63.1-63.2
- [22] P. Shao, R. Y. M. Huang (2007) *Polymeric membrane pervaporation* J. Membr. Sci. 287, 162-179
- [23] T. C. Bowen, H. Kalipcilar, J. L. Falconer, R. D. Noble (2003) *Pervaporation of organic/water mixtures through B-ZSM-5 zeolite membrane on monolith supports* J. Membr. Sci. 215, 235-247
- [24] J. Xiao and J. Wei (1992) *Diffusion Mechanism of hydrocarbons in zeolites-I. Theory* Chemical Engineering Science, 47, 5, 1123-1141
- [25] N. Metropolis and S. Ulam (1949) *The Monte Carlo method* J. Am. stat. Ass., 44, 335-341
- [26] N. Metropolis, A. Rosenbluth, M. Rosenbluth, A. Teller, and E. Teller (1953) *Equation of state calculations by fast computing machines* J. Chem. Phys., 21, 1087

Chapter 4

CNTs properties

4.1 On rejection of Carbon Nanotubes: a Density Functional and Molecular Dynamic study

4.1.1 Introduction

The rejection capability of CNTs to some uncharged organic solute with low molecular weight coming from pharmaceutical industrial water and olive mill wastewater was investigated. A general geometric criterion, completely free from fitting or empirical parameters, was proposed in order to predict the CNT optimal internal diameter able to reject target compounds by a size exclusion mechanism. This criterion uses the molecular minimum cross section evaluated from the Quantum Mechanics (QM) optimised geometry of the compounds. Furthermore Molecular Dynamic (MD) simulations and QM calculations were performed in order to provide a most complete view of the rejection process.

The rejection of organic molecules and ions with very low molecular weight is considered a fundamental aspect in the design of innovative membranes for water treatment. Two different aspects emerge in this contest: the removal of pollutants and the recovery of molecules with high added value from wastewater. CNTs can be considered innovative materials in this field since they combine amazing hydro-

dynamic properties with the ability to reject low molecular weight solutes thanks to their tuneable nanometric internal diameters. In the rejection of organic solutes by NF membranes, size exclusion plays an important role and as consequence the molecular sizes are reported by several authors to be fundamental descriptors in this contest. Based on a molecular descriptor, a geometric criterion able to provide direct information on the rejection capability of CNTs is here given. In details, the criterion provides the optimum internal diameter of single- or multi- walls CNTs (SWNTs, MWNTs) suitable to achieve a complete rejection of target solutes by a size exclusion mechanism.

Aware that not only steric interactions play a role in the rejection mechanism, calculations at QM level were made on a specific configuration of Tyrosol molecules inside a (8,8) SWNT provided by MD simulations [1]. These QM calculations gave a theoretical validation of the geometric criterion proposed. Thus a more complete viewing that take into account the solute-CNT affinity was considered. Moreover, in order to find an additional confirmation of the proposed criterion, MD configuration of the Tyrosol inside a (10,10) SWNT was also considered. Considering that H-bonds of water molecules around the compounds and inside the CNT affect the molecular confinement inside the CNTs and the electronic free energy gap between solute in the CNT and in bulk, DFT calculations of the activation energy of Tyrosol were carried out in the (10,10) SWNT by using MD configurations of CNTs filled with only Tyrosol or with Tyrosol and water molecules.

4.1.2 The geometric criterion

In order to study the rejection properties of organic solutes with low molecular weight (ranging from around 140 Da to 300 Da) by CNTs, a topological *ab-initio* study of a solute sample shown in Fig. 4.1 (Diclofenac, Triclosan, Tyrosol, Vanillic acid, p-Coumaric acid) was conducted. In particular, the steric hindrance of the single molecules was described by using the MCS molecular descriptor (sec. 3.2). The choice of this descriptor is due to the fact that the molecular steric-hindrance in the vicinity of a inlet pore is minimal if the molecule is placed in its MCS.

Therefore based on the MCS, a geometric criterion named Maximum Circumference Diameter (MCD) was outlined in order to describe the rejection of solutes by a molecular sieving mechanism. Since in both SWNTs and MWNTs, the size

Figure 1 Chemical structures of the target molecule with their molecular weight

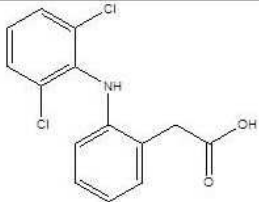
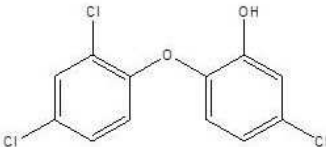
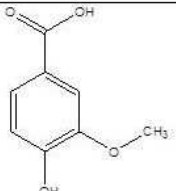
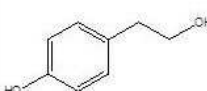
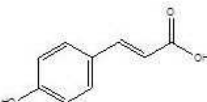
Pharmaceutical agents		
Diclofenac	Triclosan	
		
MW 296,2 Da	MW 289,5 Da	
Compounds from olive mill wastewater		
Vanillic acid	Tyrosol	p-Coumaric acid
		
MW 168,2 Da	MW 138,2 Da	MW 164,2 Da

Figure 4.1: Chemical structures of the target molecule with their molecular weight

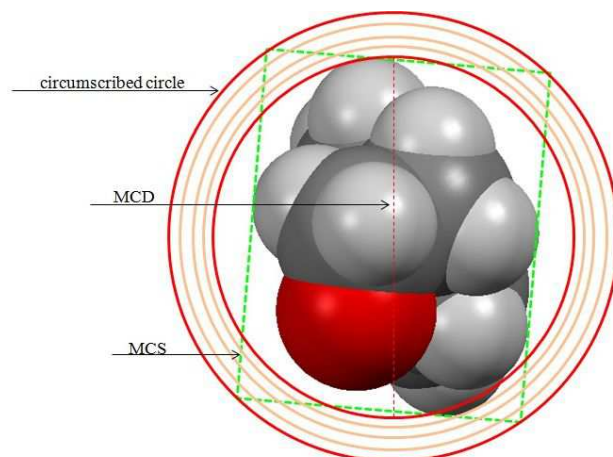


Figure 4.2: Geometrical procedure used in order to define the CNT optimal internal diameter

exclusion rejection of a molecule is ruled by the internal diameter, the criterion will immediately provide the maximum internal diameter of the CNT inlet that could be used in order to get a total rejection of a given compound. An internal diameter greater than that provided by MCD criterion will not allow to reject the target molecule for size exclusion. The circle that circumscribes the MCS was determined and it was shrunk until an atom of MCS comes out (Fig. 4.2). The diameter of this last circumference defines MCD.

It is worth noting that using the proposed criterion for a set of compounds having considerable difference in MCS, became easy calibrate the internal diameter of CNTs in order to achieve a rejection of the different solutes in CNTs-composed membranes with controlled cut-off in cascade. In this way, an efficient separation of pollutants could be obtained and at the same time small molecules with high value added could be recovered from water.

4.1.3 Computational approaches and models

As first step Molecular Mechanics calculations were carried out on all the target compound geometries with the aim to analyze their conformer space. Universal force field (UFF) was used for this work. For the geometries optimization Steepest Descent algorithm was used with a number of step equal to 500 and a convergence criterion of $10e-8$. The search of conformers was performed using the weighted

rotor search method with a number of conformers equal to 100 [2]. This method consecutively was applied 5 times for each compound in order to have a sample of conformers. Based on this sampling, the energy of each conformer was evaluated at a quantum mechanics level. A Boltzmann distribution of the energies of the optimized structures was taken into account[3] and the conformer with the highest Boltzmann factor was favoured over the other conformers. A full geometry optimization of the most stable conformer was then carried out using DFT molecular orbital method based on hybrid X3LYP [4] density functional with the 6-311G* level and using the NWChem program package [5]. In particular, the energy convergence threshold was set to 10^{-6} (au) for the self-consistent field procedure, and the root-mean square of the electron density was set to $2 \cdot 10^{-5}$ (au). The geometry was optimized using analytical energy gradients and the quasi-Newton optimization with approximate energy Hessian updates. The optimization convergence was based on the maximum and root-mean-square gradient thresholds of $4.5 \cdot 10^{-4}$ and $3.0 \cdot 10^{-4}$, respectively, in conjunction with the maximum and root-mean square of the Cartesian displacement vectors with thresholds of $1.8 \cdot 10^{-3}$ and $1.2 \cdot 10^{-3}$, respectively.

In order to find a validation of the geometric criterion and to make explicit the factors that could affect the rejection, MD simulations on the predicted CNTs singled out to reject a given molecule were used. The geometric criterion in fact does not take into account dynamic effects that could affect the rejection/inclusion of the molecules. Thus the inclusion of the molecules in such predicted CNTs could still occur if the molecular distortions are considered. MD simulations can describe these dynamic effects, then MD configurations (taken from literature [1]) of the Tyrosol molecules inside SWNT (8,8) (Fig. 4.3 model *A*) and SWNT (10,10) (Fig. 4.3 model *B-1* and *B-2*) were taken into account. DFT calculations were carried out on the MD configurations in order to evaluate the energetic cost associated to the molecular arrangements found by MD. It is worth noting that high computational time and calculation strategies were necessary since the used models are large from QM point of view (models with over 700 atoms were in fact used in this work). In details, all the calculations were conducted with hybrid energy functional X3LYP/3-21G level of theory for CNT atoms and 6-31G* for the molecules atoms. However due to the long computational time in order to

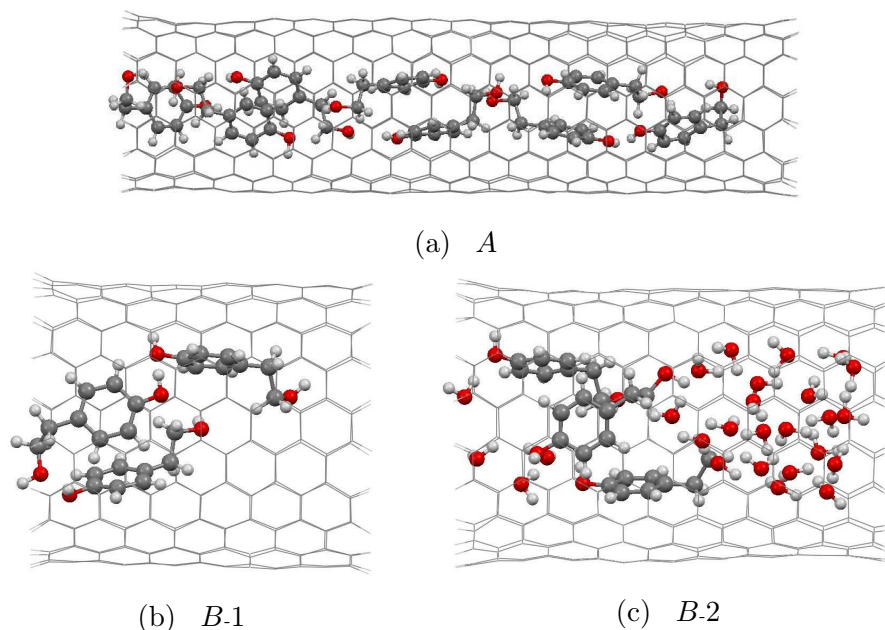


Figure 4.3: Structure of models *A*, *B-1* and *B-2* obtained by MD simulations.

achieve this level of theory different steps were necessary. The calculations in fact were started using a lower level of theory and projecting subsequently the smaller atomic orbital basis in larger one until the current basis are achieved.

4.1.4 Results and discussion

The characteristic sizes of the target solutes, H , d_{min} and d_{max} (sec. 3.2) were reported in Tab. 4.1. Thus based on the MCS, the MCD was calculated for each compound as reported in Tab. 4.2. By this value armchair and zigzag SWNTs

Table 4.1: Calculated molecular sizes

Compounds	H (Å)	d_{min} (Å)	d_{max} (Å)
Diclofenac	12.4	7.0	9.7
Triclosan	13.9	6.5	7.5
Vanillic acid	10.5	4.3	8.6
Tyrosol	10.4	5.5	6.7
p-Coumaric acid	12.1	3.5	7.3

Table 4.2: SWNTs rejecting the target compounds classified by kind and diameter (d_{CNT})

Compounds	MCD (Å)	SWNT (n,n)	d_{CNT} (Å)	SWNT (n,0)	d_{CNT} (Å)
Diclofenac	14.0	(10,10)	13.6	(17,0)	13.3
Triclosan	12.5	(9,9)	12.2	(16,0)	12.5
Vanillic acid	12.4	(9,9)	12.2	(15,0)	11.7
Tyrosol	10.8	(8,8)	10.8	(13,0)	10.2
p-Coumaric acid	10.9	(8,8)	10.8	(13,0)	10.2

Table 4.3: SWNTs rejecting a set of compounds coming from textile industry wastewater classified by kind

Compounds	MCD (Å)	SWNT (n,n)	SWNT (n,0)
(Reactive Black 5) ⁻⁴	19.1	(14,14)	(24,0)
(Remazol Brilliant Blue R) ⁻²	16.9	(12,12)	(21,0)
(Acid Red 4) ⁻	14.2	(10,10)	(18,0)
(Methylen Blue) ⁺	11.8	(8,8)	(15,0)
EDTA	15.8	(11,11)	(20,0)

singled out to reject the compounds were also reported. By analysing the MCD in Tab. 4.2, it appears that the complete rejection by a size exclusion mechanism of the solutes sample occurs by using (8,8) and (13,0) SWNTs. Tab. 4.3 shows the MCD for a set of compounds having more difference in MCS. At this point a validation of these predictions was carried out by exploiting the results of some MD simulation of Tyrosol molecules inside CNTs.

A previous work [1] reporting Equilibrium MD simulations for Vanillic acid, Tyrosol and p-Coumaric acid inside smooth SWNTs showed that due to their chemical structures (phenolic), phenyl-phenyl interactions and interactions with the CNT walls, under strong confinement, cause these molecules to form highly ordered structures inside the nanotubes. Really, this packing fits the way in which the geometric criterion was developed that is considering the molecules located respect their MCS. MD simulations indicated that the compounds cannot enter (6,6) nanotube with a diameter equal to 8.14 Å while for the larger one CNT, (8,8), a packed structure was found inside. The model *A* was used in this analysis. Thus (8,8) SWCNT with Tyrosol molecules inside was analyzed at QM level with the aim

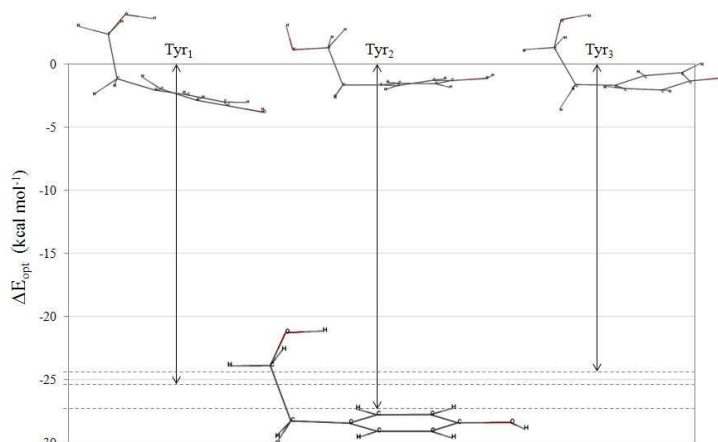


Figure 4.4: Three random molecules extracted from *A* model. The distortions of the Tyrosol phenyl ring with respect to the QM optimized geometry are shown.

Table 4.4: Energy difference between QM optimized structures and MD structures ($kcal \cdot mol^{-1}$)

Models	ΔE_{opt}
<i>Tyr</i> ₁	-25.33
<i>Tyr</i> ₂	-27.12
<i>Tyr</i> ₃	-24.19

to understand if the inclusion of the molecules can be attributed at an energetic effect that is not taken into account in the geometric prediction. Among the 8 Tyrosol molecules found in the MD configuration, three random Tyrosol molecules (*Tyr*₁, *Tyr*₂, *Tyr*₃) were extracted and a molecular relaxation was carried out by a DFT geometry optimization in order to evaluate if the molecule have undergone some distortion. First of all a relevant distortion of the Tyrosol molecules placed in the CNT was observed (Fig. 4.4). A quantification of these distortions are reported in Tab. 4.4. It is worth noting that, as described in sec. 2.3, these energies belong to the range of medium non-covalent interactions that cannot be neglected.

Also, the balance energy between the outside and the inside of the CNT was evaluated by splitting the process in more steps, that is considering the self-assembly and inclusion energy. The energy associated to the molecular self-assembly, ΔE_1 , was evaluated as difference between the Tyrosol wire and isolated

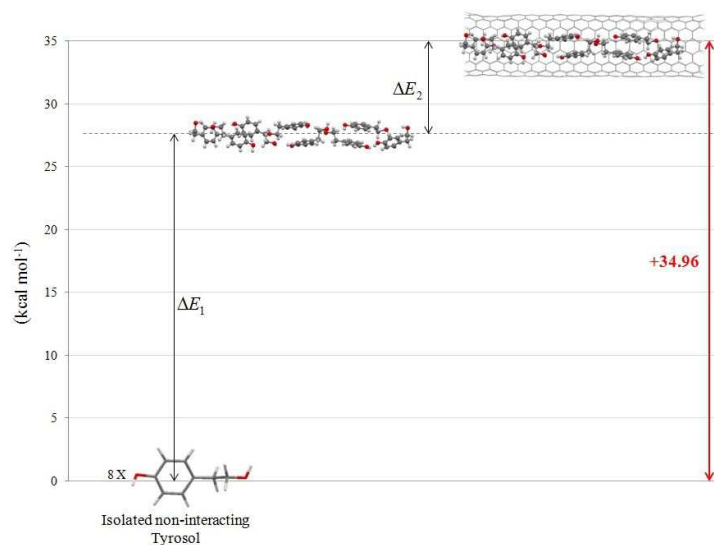


Figure 4.5: Process to evaluate the balance energy of Tyrosol molecules in a SWCNT (8,8). The average value for a single Tyrosol molecule is reported.

molecules while the inclusion energy, ΔE_2 , was evaluated as the difference between the energy of the adduct and those of the isolated single components (Tyrosol wire and CNT). The basis set superposition error (BSSE) was also included in the calculations of the interaction energies according to the counterpoise method [6]. Therefore, the energy that a Tyrosol molecule in the bulk should spend in order to be compacted and trapped in the CNT with the arrangement provided in *A* was evaluated. Fig. 4.5 shows the whole process considered according the calculated contributes ΔE_1 and ΔE_2 . As a result an average energy of $+34.96 \text{ kcal} \cdot \text{mol}^{-1}$ has to be provided at each single Tyrosol in order to take place in the (8,8) CNT. In other terms, a quantity of average total energy must be supplied to a mole of single molecules of Tyrosol in order to get the configuration *A* and without this energy a spontaneous inclusion of the Tyrosol molecules inside a (8,8) CNT is not favourite. Thus, in agreement with the geometric criterion, can be expected the occurrence of a spontaneous rejection of the Tyrosol by the (8,8) CNT.

In order to find an additional confirmation of the proposed geometric criterion, QM calculations of the Tyrosol activation energy was carried out on a SWNT (10,10) that is able to host the Tyrosol molecules according to the criterion. The model *B-1* was used in this analysis (Fig. 4.3, model *B-1*). The most external

Table 4.5: Activation energy of Mol_{ref} ($kcal \cdot mol^{-1}$) calculated at X3LYP/3-21G (CNT), 6-31G* (molecules) level considering *B-1* (MD configuration of a SWCNT (10,10) hosting Tyrosol molecules) and *B-2* model (MD configuration of a SWCNT (10,10) hosting Tyrosol and water molecules)

Model	ΔE_a
<i>B-1</i>	2.93
<i>B-2</i>	-1.29

molecule of the complex was taken as reference molecule (Mol_{ref}) and the activation energy, ΔE_a , was evaluated again as difference between the adduct and single components i.e. Mol_{ref} and CNT with the remaining two molecules. BSSE is corrected in this calculation. As reported in Tab. 4.5 a slightly positive value of +2.93 $kcal \cdot mol^{-1}$ was found confirming again that the inclusion of a Tyrosol molecule in a larger CNT can occur without spend high energy. It is worth noting that in order to verify the basis set quality impact, this calculation was also performed with a large basis set on the Tyrosol molecule (6-31++G*). The change in energy obtained was of 1 $kcal \cdot mol^{-1}$ and due to the excessive required time more, no other calculations were performed whit this basis set.

Finally, aware that the water molecules around the compounds can affect the packing and the electronic free energy gap due to the H-bonds, an evaluation of the activation energy concerning the configuration of Tyrosol and water confined inside the SWCNT (10, 10) as obtained by MD simulation (Fig. 4.3, model *B-2*) was carried out. In this case the most external molecule, bonded to a water molecule by an H-bond, was taken as reference molecule (Mol_{ref}) and the CNT with the remaining two Tyrosol and attached water molecules was taken as other component. In addition a QM valuation of the Tyrosol molecule in the bulk was considered calculating the solvation free energy of the Tyrosol without and with the first shell of water molecule around it (formed by 4 water molecules). Thus ΔG and ΔG^{hyd} contributions were taken into account. For this calculation, the continuum conductor-like screening model (COSMO), proposed by Klamt and Schüürmann [7] was used. It worth noting that due to the complexity of the systems analysed, being formed by a high number of atoms, and being sure that the chemical property here calculated will not be affected, only the initial part of the whole provided MD

Table 4.6: Solvation energy of the reference Tyrosol without and with the first shell of water molecule around it in *B-2* model ($kcal \cdot mol^{-1}$)

Model	ΔG	ΔG^{hyd}
Mol_{ref} (in <i>B-2</i>)	-8.31	-15.96

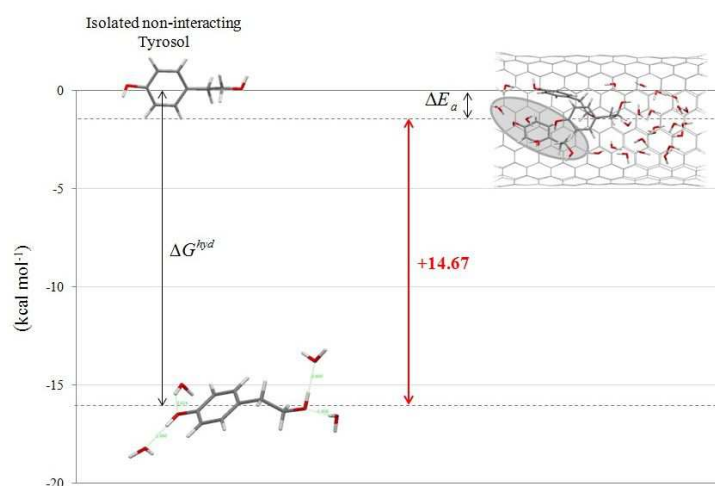


Figure 4.6: Differences of energy to calculate the activation energy of a Tyrosol molecule in model *B-2*

configuration was used in these calculations.

The activation energy obtained is $-1.29 kcal \cdot mol^{-1}$ (Tab. 4.5) without considering the solvation free energy contribute. However, by taking into account this contribution that as reported in Tab. 4.6 is $-8.31 kcal \cdot mol^{-1}$ and $-15.96 kcal \cdot mol^{-1}$ if the hydrated Tyrosol is considered, an activation energy of $+7.02 kcal \cdot mol^{-1}$ was obtained in the first case and $+14.67 kcal \cdot mol^{-1}$ in the second one. Contrary to the case of (8,8) SWNT, these energy values belong to the range of medium-weak non-covalent interactions (sec. 2.3). The energy differences are schematized in Fig. 4.6. By this value emerges that the water molecules can in part affect the spontaneous inclusion of the Tyrosol molecule that however is still possible. In fact respect to the same system without water molecules a bigger activation energy is request in order to get the Tyrosol molecule inside the CNT opening. From this argument can be expected that in general the formation of numerous H-bonds with water molecules result in an unfavourable effect in term of inclusion and as result

in a favourable effect in term of rejection. Thus it can be expected that the results provided by the geometric criterion are valid for the rejection of the target.

4.1.5 Conclusions

A geometric criterion is provided in order to outline the kind of CNTs able to reject target compounds. A validation of this criterion was provided by using previous MD simulations and QM calculations. In particular DFT calculations carried out on a crucial MD conformation of a (8,8) SWNT hosting Tyrosol molecules showed that due to significant distortions of the target molecules, that are not compensated either by hydrogen bonds that are formed in the molecular self-assembly or by the interactions between molecules and CNT, the rejection of Tyrosol by (8,8) SWNT is predicted by the geometric criterion. Also, the activation energy for the same molecule was evaluated on a MD configuration of a (10,10) SWNT hosting Tyrosol molecules without and with water molecules. A slightly positive value obtained in the first case suggests that the inclusion of Tyrosol can occur in this case. Regarding the last case instead higher activation energy is found suggesting that though the water molecules affect the separations processes, the rejection by predicted CNTs can still occur. Finally, it worth noting that the proposed geometric criterion is not related at the kind of porous material or compounds involved in the rejection process. The CNTs here studied can be regarded as ideal pores and thus a most general application of the geometric criterion could be considered.

4.2 Perm-Selectivity optimization of Olygomer-IM functionalised CNT-polymer membranes

4.2.1 Introduction

As pointed out in sec. 1.2 in membrane-based wastewater treatment, permeability and selectivity are considered key performance parameters and, in general, the increase of the former comes at the expense of the latter. Mixed-matrix membranes, where a selected phase is added to the polymer matrix to enhance either characteristic, have emerged as the most promising technology to further reduce

the energy and economic costs of membrane-based filtration processes.

In particular, as already mentioned in sec. 1.2, among the many materials considered as potential additives, carbon nanotubes have attracted the most interest due to a combination of low transport resistance and chemical inertness. The first published molecular dynamics simulation of water flow inside a SWNT with a diameter of 1 nm or less showed flow rates orders of magnitude higher than what predicted by the standard no-slip Hagen-Poiseuille (H-P) equation for steady state flow in a cylindrical channel under a constant pressure gradient [8]. This ‘flow enhancement’ was initially described in terms of ballistic transport [9] and associated with the hydrophobicity of the nanotube’s wall in respect to water [10]. Although equations based on the continuum model cannot be applied for tubes of these sizes [11], further modelling and experimental results have all used flow enhancement, defined as the ratio of the measured or modelled flow rate over the no-slip H-P one, to evaluate the effective permeability of water and other fluids in carbon nanotubes. Results have varied greatly, with flow enhancements up to 10,000 in tubes with diameters varying from less than 1 nm up to tens of nanometers, including multi wall carbon nanotubes (MWNTs) [12]. This large variation can be attributed to the fact that carbon nanotubes are actually a family of materials, whose properties can vary significantly due to the synthesis process used, from geometrical characteristics (diameter and length) to the surface structure (from turbostratic to highly organized graphitic) to the surface chemistry (from hydrophobic to hydrophilic) [10, 12]. In fact, these apparent discrepancies can be resolved by normalizing modelling and experimental flow rates for the tubes’ geometrical characteristics and solid-liquid molecular interactions [13]. With this understanding and a precise control of the synthesis conditions, fine-tuning of the nanotubes’ performance in terms of permeability is now possible.

While MD simulations are mostly confined to a small number of tubes [14], most experimental work has been done on bespoke carbon nanotube membranes due to the complexity of handling individual tubes and measuring such small flows. The membranes produced for these initial experimental studies are small, 1 cm² or less of filtration area, and manufactured using an aligned array of CNTs produced via catalytic chemical vapour deposition. The array was then coated with polymer [15] or embedded in an inorganic matrix [16] to provide stability

and prevent leaks. An alternative technique deposited turbostratic carbon in the pores of alumina templates, creating what have been called nanopipe structures [17]. Unfortunately, none of these techniques can actually be scaled economically to a level where they can supply the wastewater membrane market [18].

A more practical route is to incorporate nanotube dispersions in polymeric or ceramic matrices in analogy with what done for other mixed-matrix membranes. Results, so far, have been limited due to the inability of aligning a large number of carbon nanotubes perpendicularly to the filtration surface [10, 12]. In addition, most CNTs tend to be hydrophobic, thereby requiring surface functionalization to avoid aggregation in aqueous media, which is used as a solvent in most membrane preparation methods [19, 20, 21].

While nanotube permeability has been extensively studied, less work has been done on CNT selectivity, due to the complexity of achieving nanotube membranes with adequate characteristic such as membranes with vertically aligned or well dispersed CNTs. In addition, a tricky problem is the rejection of molecules with low molecular weight since in this case CNTs with very small internal diameter should be used. For example, to reject a 200 Da molecule a SWNT with diameter of 1 nm would be required (see sec. 4.1).

Functionalization of the inlet of nanostructures has emerged as an alternative to size-based selectivity [22]. Charge-based selectivity was significantly increased when the tips of a MWNT-polymer membrane were functionalized with alkanes and amines, attached to the tubes via carboxylic defects created on the tubes' tips [23]. MD studies on the functionalization of SWNTs for use in seawater desalination have shown that the addition of charges on the tip of a 1.1 nm SWNT can reduce the passage of ions but at the expense of water permeability [24].

Therefore in this thesis, a computational study of CNT-composite membranes is presented with the aim of optimizing tube diameter and tip functionalization to maximise both permeability and selectivity.

4.2.2 Materials and methodology

An ideal MWNT-polymer membrane is considered in this modeling study where all the nanotubes are perpendicularly aligned in a polymeric matrix, even though, as discussed in the introduction, this has, so far, only been achieved for

laboratory-scale membranes. A polyester thin film composite (TFC) asymmetric membrane [24] and a chitosan porous membrane [25] were used as the reference materials. For the first membrane, the thickness of the selective layer is approximately 500 nm. A membrane area of 27 cm² and an operation pressure of 0.6 MPa at room temperature are used in the pure water flux measures as reported in ref. [24]. For the chitosan membrane, a mean thickness of the wet membrane of about 130-140 μm is used, as reported. The pure water flux is tested under the pressure drop of 0.1 MPa with an effective membrane area of 11.33 cm² [25]. Even if in both these reference membranes non-aligned MWNTs are used, however in this thesis the data used in the computational optimization refer to the membranes without MWNTs.

Permeability optimization

When considering MWNTs, the thickness of the tubes has to be considered in the calculation of the effective CNT permeable area, i.e. $A_{CNT,eff}$:

$$A_{CNT,eff} = \sum_{i=1}^n \pi \frac{d_{CNT,i}^2}{4} \equiv n\pi \frac{d_{CNT,i}^2}{4} \quad (4.1)$$

where d_{CNT} is the internal tube diameter. On the other hand, the membrane surface fraction *occupied by the CNTs* is:

$$f = \frac{A_{CNT}}{A_{mem}} = \frac{1}{A_{mem}} \sum_{i=1}^n \pi \frac{D_{CNT,i}^2}{4} \equiv \frac{n\pi D_{CNT}^2}{4A_{mem}} \quad (4.2)$$

where A_{mem} is the total membrane area and A_{CNT} the total area occupied by the CNTs. For MWNTs, $A_{CNT,eff} < A_{CNT}$ being D_{CNT} and d_{CNT} the external and internal tube diameters, respectively, and n the number of tubes. Several combinations of D_{CNT} and d_{CNT} have been investigated (Tab. 4.7) and for a SWNT it is assumed that $D_{CNT} \equiv d_{CNT}$. In this case it is useful to observe that these diameters are the carbon-carbon nuclei distance. The above equations assume no size distribution for the nanotubes, a constant cross-section throughout their length and tortuosity, $\tau = 1$. With these assumptions, f is equivalent to a standard surface porosity.

*double-wall CNTs were considered by adding the interlayer distance [26]

Table 4.7: Internal and external CNT diameters

d_{CNT} (nm)	D_{CNT} (nm)
1.66	$d_{CNT} + 2 \cdot 0.34^*$
2.22	15
2.77	35
3.33	
3.88	
4.44	
4.99	

How the liquid flow in CNTs can be described is a matter of current debate, with alternative models being put forward [10, 12]. A slip-modified Hagen-Poiseuille equation was initially adopted, yielding slip lengths in the order of tens of micrometres for channels with diameters in the nanometre range [15]. Further experimental and numerical work has shown that nanoscale confinement has strong effects on the liquid's viscosity [27]. Moreover, solid-liquid interactions between the tube walls and the fluid flowing through it have to be accounted as they can significantly alter the magnitude of the flow enhancement [28]. Finally, the tubes' structure (e.g. the presence of defects [29] or their degree of graphitization [30] by relying) and length also significantly affect water flow [31].

In this thesis instead, the uncertainty on which model to adopt is side-stepped by relying on numerical data extracted from a well-known molecular dynamics paper as [32]:

$$Q_{CNT} = nq_{CNT} = n\alpha \frac{\Delta P}{L} \quad (4.3)$$

where n is number of CNTs in the membrane with flow rate in each nanotube given by q_{CNT} and $\Delta P/L$ the pressure gradient; α is a proportionality constant obtained from numerical analysis that incorporates the high flow enhancements discussed in the introduction and all dependencies (tube radius, viscosity, solid-liquid interaction, etc) without making them explicit. This method is of general use, and could be applied to flow data extracted to other publications.

The total membrane flow rate, $Q_{mem,f}$, is defined as the sum of the water flow through the nanotubes and the water flow through the remaining free area of the

membrane (the membrane fraction area not occupied by CNTs, $1 - f$):

$$Q_{mem,f} = Q_{mem,0}(1 - f) + Q_{CNT} \quad (4.4)$$

that by dividing to $Q_{mem,0}$ gives

$$\frac{Q_{mem,f}}{Q_{mem,0}} = (1 - f) + \frac{Q_{CNT}}{Q_{mem,0}} \quad (4.5)$$

where the ratio $Q_{CNT}/Q_{mem,0}$ is a measure of the increase in overall flow rate given by the presence of CNTs occupying a fraction f of the membrane surface.

To compare experimental and modelling results for different membranes, the above results can also be reported in terms of permeability, $K = QL/\Delta PA$:

$$\frac{K_{mem,f}}{K_{mem,0}} = (1 - f) + \frac{K_{CNT}}{K_{mem,0}} \quad (4.6)$$

Selectivity optimization

An investigation on the molecular sieving is proposed based only on steric hindrance. The selectivity of the CNTs is evaluated by means of a procedure based only on geometrical analysis of compounds and pore entrance. In particular the CNT inlet is taken as pore reference whose dimension is defined by d_{CNT} . In addition the case in which the nanotube inlet is reduced by anchoring functional groups (FGs) on its tip is considered. How reported in several steric-hindrance pore models, the sieving coefficient is evaluated as function of the solute and pore membrane radius: if the solute size is larger than the pore size, the solute can not partition into the membrane resulting in 100 % rejection. Therefore based on this concept, the rejection of a target compound is here quantified as $R \propto 1 - \Sigma$ with:

$$\Sigma = \frac{A_{mol,perm}}{A_{CNT,free}} \quad (4.7)$$

where $A_{mol,perm}$ is the ‘molecular permeation area’, characterized by the $\sigma_{mol,perm}$ set, in which a molecule can permeate on the CNT inlet without steric hindrance (see sec. 3.3.1). While $A_{CNT,free}$ is the ‘maximum free area’ of the nanotube inlet characterized by the set $\sigma_{CNT,free}$. For a pore without anchored FGs $A_{CNT,free} = \pi(\frac{d_{CNT}}{2} - r_C)^2$ where r_C is the vdW radius of a carbon atom and it is clearly smaller when FGs are instead considered. $A_{CNT,free}$ and $A_{mol,perm}$ were estimated for the functionalized CNTs according to the algorithm presented

in previous chapter sec. 3.3.1. In particular in order to obtain a reliable value of $A_{CNT,free}$, the algorithm was subsequently applied for input grid having a spacing increasingly tight up to an accuracy of $5 \cdot 10^{-1}$ is achieved. A draft of a top view of a functionalized CNT is shown in sec. 3.3.1 Fig. 3.14b in which an idea of $A_{mol,perm}$ is given. It is expected that $A_{mol,perm}$ become smaller as larger is the compound examined. Thus the main role in $A_{mol,perm}$ is played by the dimensions of the compound to be rejected. An accurate dimensional analysis was made for each compound represented by its minimum cross-section. The compound was modeled as a van der Waals solid such that each atom is represented by a hard sphere with a specific radius and MCS was defined according the algorithm presented in sec. 3.2. The choice of this descriptor was made looking at the size exclusion mechanism: the steric hindrance of a molecule in the vicinity of a pore is minimal if the molecule is placed in its MCS implying that if the molecule is rejected in its MCS, it will also be rejected in any other spatial position. The results presented in sec. 4.1 also confirm this assumption. It is worth pointing out that the whole procedure adopted to describe the CNT selectivity property is free from any adjustable parameter being based only on topological analysis of the considered systems and on the geometries of the target compounds obtained from *ab-initio* quantum calculations.

4.2.3 Molecular models and computational details

A common low molecular weight therapeutic compound, rac-Fluoxetine, widely found in wastewater and whose removal is currently considered challenging, was selected in this study in addition to glucose, ethanol and water. Since the selectivity of MWNTs is ruled by the size of the inner core, a focus was given at the functionalization of the MWNT inner inlet not considering the MWNTs interlayers. It is worth noting that MWNTs with OH groups located along the inlet or along their defects are much less expensive than functionalised single- or double- wall CNTs. In particular the functionalization of an inlet of 4.44 nm was investigated. The reason for this choice is based on the permeability optimization according to the approach presented in the previous section and whose results will be presented below in sec. 4.2.4. As functional groups, the monomers belonging to a recently developed new type of ‘polymers of intrinsic microporosity (PIMs)’ [33] were con-

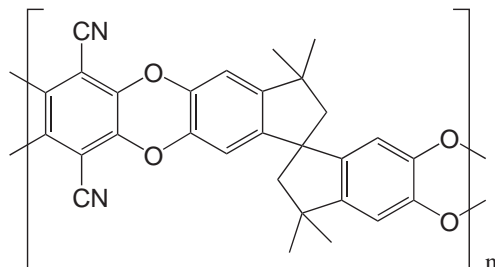


Figure 4.7: PIM-1 [33] used to elongate A and B

sidered. Thus, the nanostructures studied in this thesis could be considered as a hybrid between Olygomer-IMs and CNTs [34]. It is worth noting that the hangings to be anchored on the CNT edge should show as less as possible electrostatic interactions with the target molecules. In fact, in the size-exclusion mechanism electrostatic non-covalent interactions with the molecules are negligible, i.e. are not the driving force of the rejection.

After initialization step, made via tetrafluoro-phthalonitrile in the first case (*A*) and 1,2 bis (2-bromoethyl)-4,5-difluorobenzene in the second one (*B*), a monomer derived from the commercially available 5,5',6,6'-tetrahydroxy-3,3,3',3'-tetramethyl-1,1'-spirobisindane [33] was added in both cases. The spiro-centre provides a non-linear shape in the rigid ladder polymer structure. Then fragments were elongated by means of monomers in Fig. 4.7. $n = 1$ was used for functional model *A* and $n = 2$ for functional model *B*; the length of the FGs was calibrated as function of the inlet size. It is worth noting that depending on the spiro-centre of monomer PIM-1, different configurations can be obtained distinguished as inside (IN) and outside (OUT) on the basis of the orientation of the PIM-1 oligomers, i.e. the functional group pointing towards the center of the CNT or out. Two or three FGs were anchored with different orientations. In Fig. 4.8 and Tab. 4.8 are summarised all cases considered.

It is important to recall that *A* and *B* FGs have two different kinds of anchoring spot on the ring of the CNT. End-substituted CNTs are by -product of mild oxidation and carboxylic, carbonyl and hydroxyl groups are frequently formed [35, 36]. An end OH substitution was considered in the model randomly substituting one-third of the total hydrogen atoms on the ring of the tube. Since the position

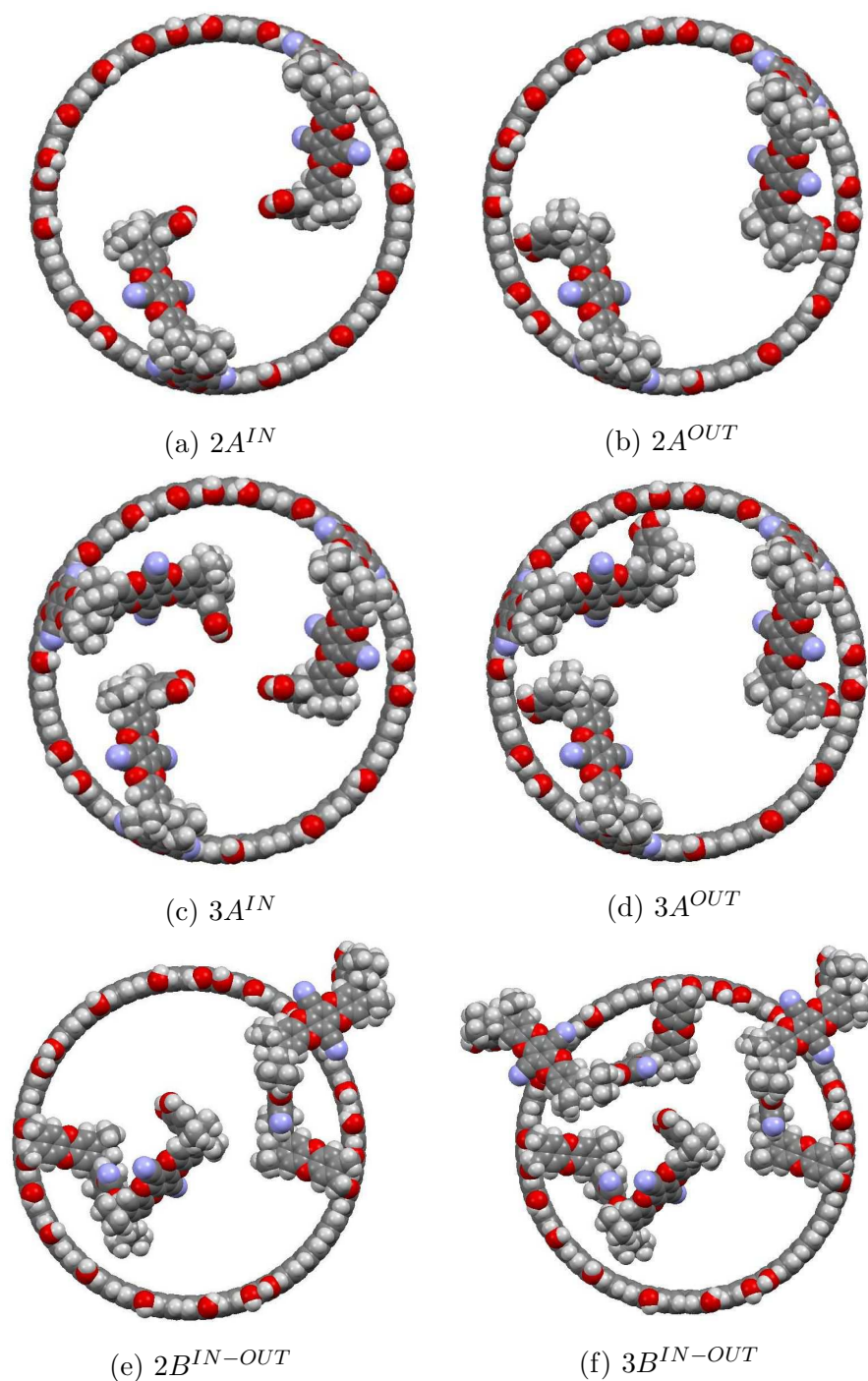


Figure 4.8: Top view of a CNT having $d_{CNT} = 4.44$ nm and functionalized by means of (a) two fragment models A pointing IN, (b) two fragment models A pointing OUT, (c) three fragment models A pointing IN, (d) three fragment models A pointing OUT, (e) two fragment models B , one pointing IN and one pointing OUT, (f) three fragment models B , one pointing IN and two pointing OUT.

Table 4.8: Total number of atoms of the functional groups anchored

Functional groups	No. of atoms
$2A^{IN}, 2A^{OUT}$	232
$3A^{IN}, 3A^{OUT}$	348
$2B^{IN-OUT}$	350
$3B^{IN-OUT}$	525

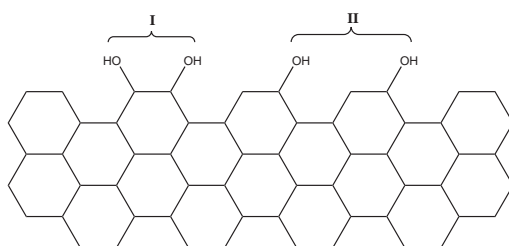


Figure 4.9: Schematic localization of two OH substituents on an armchair CNT ring.

of the OH groups used for the anchoring of *A* and *B* functional group models is random, two different situations are taken into account. In Fig. 4.9 the case of two adjacent and separated OH groups is presented.

Calculations were performed using NWChem program [5]. Exchange-correlation X3LYP [4] hybrid density functional and large basis sets (6-311++G**) were selected for the optimization of the geometry compounds. While, due to the large size of functionalized CNT systems, the DFT calculations with relatively small basis sets (3-21G*) were used for theoretical description of functional groups structure. For the CNT model, whose Cartesian coordinates were frozen during the geometry optimization of the FGs, a minimal basis set was used. In particular, a first step of optimization was carried out by considering a small piece of the whole *A* and *B* structures. Fig. 4.10 shows the starting and optimized geometry of an anchored *A* piece.

By accurate optimization of this piece of *A* functional group, the inclination of the entire model on the CNT inlet was analysed. Then a bigger model was built in which a full optimization (Fig. 4.11) was carried out by means of ‘Our own N-layered Integrated molecular Orbital and molecular Mechanics’ (ONIOM), the hybrid method of Morokuma and coworkers [38, 39]. This QM approach enables

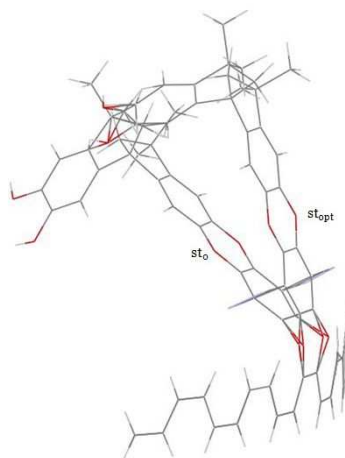


Figure 4.10: Initial (st_0) and optimized (st_{opt}) geometry of a piece of A

different levels of theory to be applied to different parts of the system and combined to produce a consistent energy expression. The optimized part was kept at the same level theory and considered as the high-level calculation contemplated in the method while the effects of the remainder were included at the lower levels of theory Slater [37]/3-21G. A deep geometry optimization (i.e. tighter criteria) was prevented by repeated fluctuations of distances and bond angles. However, it was deemed that for the property here investigated, the steric hindrance formed by the functional groups, these small fluctuations are not relevant. The same optimization procedure was used for B functional group.

Should be noted that the choice of A and B FGs is the result of a long screening among different other groups. In fact various FGs were tested such as Oligo Ethylene Glycol and silanes whose application in the functionalization of surfaces or fillers is widely found. Due to the great flexibility of the aliphatic chains constituting these functional groups, a conformational analysis was necessary in order to define their disposition on the CNT inlet. These were clearly not suitable to form steric hindrance on the CNT inlet due to their high degree of winding.

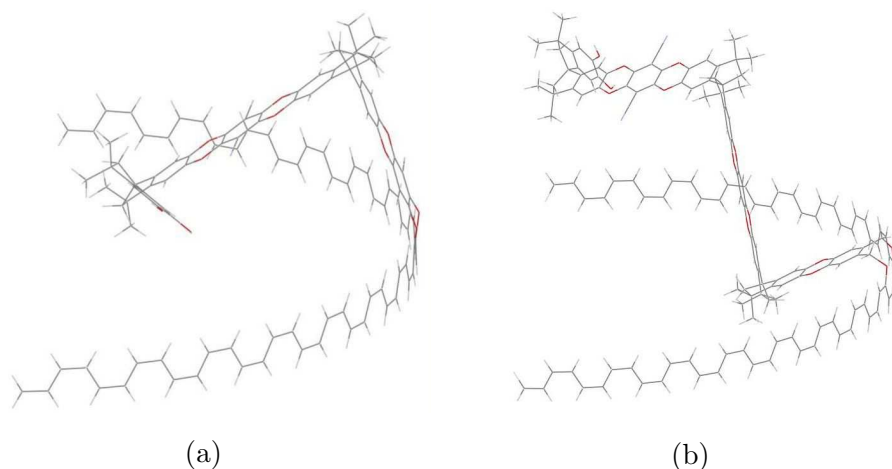


Figure 4.11: Optimized structures of (a) FG A and (b) FG B

4.2.4 Results and discussion

Permeability prediction

In Fig. 4.12 the ratio $K_{mem,f}/K_{mem_0}$ versus f is presented considering low density of vertically aligned MWNTs within the TFC membrane. All seven d_{CNT} are taken into account and a length L of 500 nm was considered for the MWNTs i.e. equal to the thickness of the TFC selective layer. The case studies in which MWNTs with $D_{CNT} = 35$ nm (Fig. 4.12a) as well as $D_{CNT} = 15$ nm (Fig. 4.12b) are added, is reported.

An increase in overall permeability directly proportional to the fraction of the membrane surface occupied by MWNTs is emerged that ranges from 135 to 732 when f is 40%. An overall permeability of 5-times bigger is obtained passing from external tube diameters of 35 nm to 15 nm. This finding is very important since it allows to optimize external CNT diameters depending on the performance required to the membrane. Also the changing of the internal tube diameters leads to a relevant variation in overall permeability: an increase of around 8-times is obtained passing from 1.66 nm to 4.99 nm. The graphs (Fig. 4.13) are also reported for the chitosan porous membrane. Again D_{CNT} and d_{CNT} were optimized but considering the MWNT length equal to the thickness of that membrane. Regardless of d_{CNT} , D_{CNT} and of the density of vertically aligned MWNTs, in the chitosan porous membrane surprisingly the inclusion of MWNTs confers a decrease of the

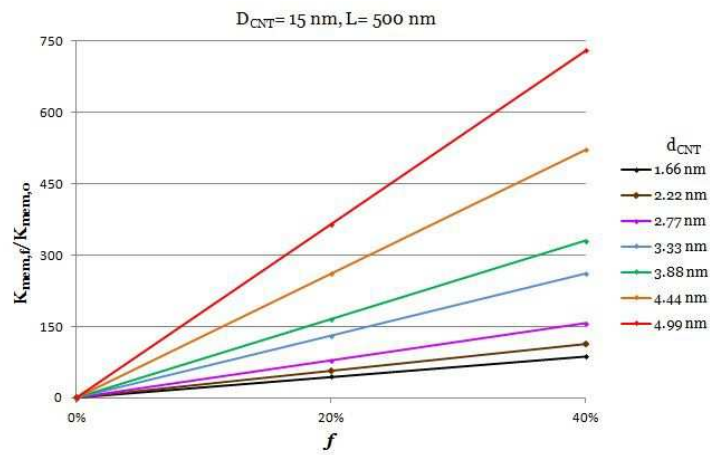
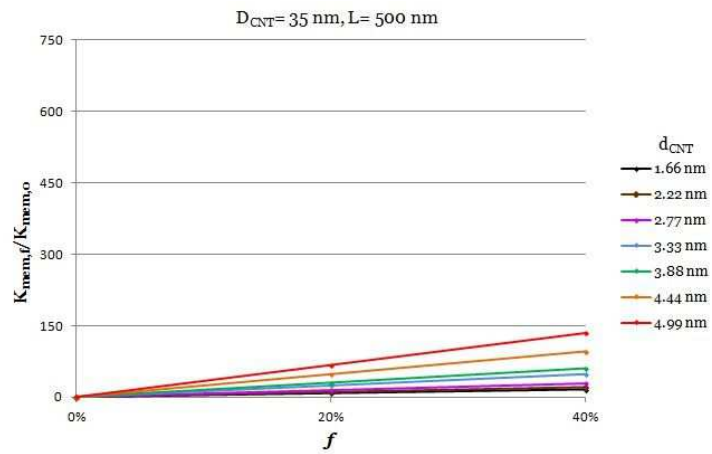
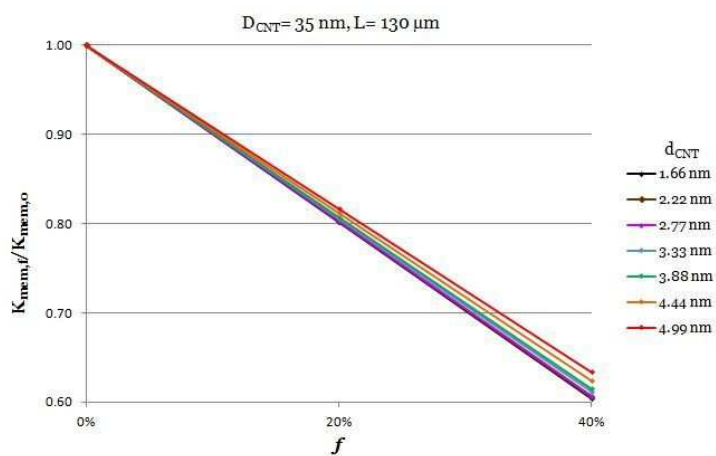
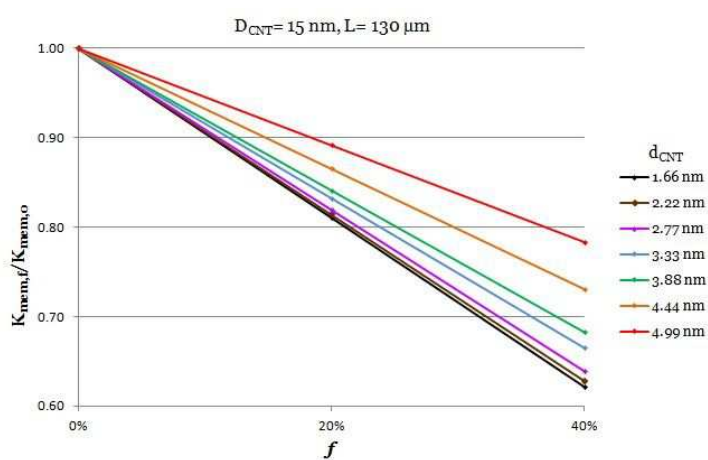


Figure 4.12: Increase in overall permeability through a TFC membrane *versus* the fraction of the membrane surface occupied by MWNTs. The case in which (a) $D_{CNT} = 35 \text{ nm}$ and (b) $D_{CNT} = 15 \text{ nm}$ are used is reported for 7 internal tube diameters.



(a)



(b)

Figure 4.13: $K_{mem,f}/K_{mem,0}$ versus f for a CNT-composite chitosan porous membrane. The case in which (a) $D_{CNT} = 35 \text{ nm}$ and (b) $D_{CNT} = 15 \text{ nm}$ are used is reported for 7 internal tube diameters.

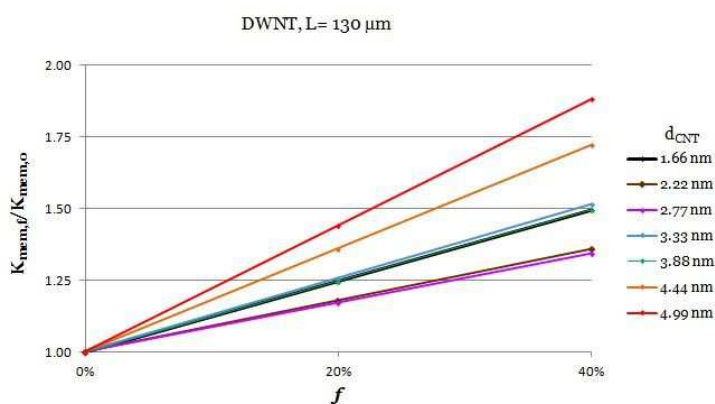


Figure 4.14: Increase in overall permeability for a Chitosan porous membrane *versus* the fraction of the membrane surface occupied by DWNTs. The case in which DWNTs are used is reported for 7 internal tube diameters.

water permeability. However this it is explained by considering that the chitosan membrane itself is extremely water permeable and the addition of MWNTs only results in losing of membrane surface since the water doesn't flow through the MWNTs interlayers. Thus the water flow enhancement that should be provided by the nanotubes is not enough to compensate the flow loss caused by the reduction of the membrane surface [34]. By these arguments an increase in permeability could be achieved if thin MWNTs are used. In Fig. 4.14, in which double-wall CNTs (DWNTs) are used, is confirmed that thin MWNTs confers an increase of the overall permeability although it does not lead to high improvement observed for the TFC membrane. Almost twice the permeability is found when the 40% of the surface membrane is occupied by DWNTs having internal diameter of 4.99 nm. Moreover, it is worth noting that on the contrary to the TFC membrane, in this last case the increase in overall permeability is not directly proportional to the internal nanotube diameters. In fact for the DWNT-chitosan membrane, the same water permeability enhancement can be achieved by using internal diameters equal to 1.66 nm or 3.33 nm or 3.88 nm.

From the analysis of the results presented in the graphs emerges that a calibration of internal and outer diameters to be used is of considerable importance especially looking at the optimization of both permeability and selectivity. In particular for the TFC membrane, MWNTs with an internal diameter of 4.44 or

Table 4.9: Dimensional analysis of the compounds: the sides of MCS (d_{min}, d_{max}) are listed

compounds	d_{min} (Å)	d_{max} (Å)
rac-Fluoxetine	6.66	11.00
Glucose	6.04	6.73
Ethanol	4.17	4.58
Water	2.80	3.15

4.99 nm allow to reach an optimal compromise between the enhancement in permeability and the density of nanotube to align with a consequently benefit in the cost. Instead for the chitosan membrane by using the same density of aligned nanotubes, SWNTs or DWNTs are necessary in order to obtain an increased permeability. This is much more expensive and difficult being the chitosan membrane already highly permeable without nanotubes.

Selectivity prediction

The MCS of the four compounds examined gives a trend on their steric hindrance in accordance with the conclusion of sec. *Selectivity optimization*. In particular, from d_{min} and d_{max} (the two sides of MCS) reported in Tab. 4.9 it results:

$$MCS_{\text{rac-Fluoxetine}} > MCS_{\text{Glucose}} > MCS_{\text{Ethanol}} > MCS_{\text{Water}}. \quad (4.8)$$

When only steric hindrance effects are considered as the driving force to the rejection, it is expected that the compounds rejection follows the same above trend: for the same permeation area a bigger molecule will be more rejected than a smaller one. As was pointed out in sec. *Selectivity optimization*, molecular rejection was assumed to be proportional to $1 - \Sigma$ with $\Sigma = A_{mol,perm}/A_{CNT,free}$. It is important to recall that in the evaluation of $A_{CNT,free}$ is taken into account the steric effect of functional groups anchored on the CNT edge that it is also taken into account in the evaluation of $A_{mol,perm}$ along with the molecular MCS. This approach [34] is innovative in fact so far only empirical approaches are presented in literature in which the steric hindrance of the functional groups on membrane pores is empirically considered by means of the sieving coefficient. It is worth noting that although in the case of non functionalized pores, a mean pore diameter or a pores

Table 4.10: Calculated $1 - \Sigma$ for all combinations investigated with A functional groups

	$1 - \Sigma$ (%)			
	$2A^{IN}$	$2A^{OUT}$	$3A^{IN}$	$3A^{OUT}$
rac-Fluoxetine	60	41	86	52
Glucose	50	35	71	44
Ethanol	35	25	50	33
Water	23	18	34	25

Table 4.11: Calculated $1 - \Sigma$ for all combinations investigated with B functional groups

	$1 - \Sigma$ (%)	
	$2B^{IN-OUT}$	$3B^{IN-OUT}$
rac-Fluoxetine	82	91
Glucose	72	85
Ethanol	57	73
Water	42	55

distribution is easy to consider, in the case of functionalized pores which size has to be considered as molecular permeation area is not clear from a purely theoretical point of view. This work is the first attempt to address this key problem in the frame of membrane separations.

Tab. 4.10 and Tab. 4.11, in which the quantity $1 - \Sigma$ is reported for the target compounds as function of the number and kind of anchored functional groups, show that the trend (4.8) is kept for the rejection.

Precisely, when A functional groups are used (Tab. 4.10) the rejection of rac-fluoxetine and glucose increase of a factor of around 2.5 and 2 respectively with respect to the water molecule. Instead, as expected a smaller increase factor is found between the ethanol and water rejection due to their more similar molecular size. These factors are found slightly reduced if B (Tab. 4.11) functional groups are used. It is important to underline that the results shown in Tab. 4.10 and 4.11 can be qualitatively provided only on the basis of a simple analysis of the molecular sizes (see trend 4.8). Nevertheless $1 - \Sigma$ values provide accurate quantitative information allowing hence detailed analysis of the structure-property relationship.

Molecular rejection can be controlled as function of the number and kind of

functional groups anchored. For example, Tab. 4.10 shows that considering all A functional groups, a sharp rejection of the rac-fluoxetine, 86 %, is achieved in $3A^{IN}$ system. Should be noted that this sharp rejection is not only achieved by using 3 FGs in place of 2, in fact a comparison between $3A^{IN}$ with $3A^{OUT}$ systems clearly show that the arrangement of FGs on the CNT inlet is the main parameter ruling the rejection. This is also confirmed by using 2 or 3 FGs of B type (Tab. 4.11). In fact for the rac-fluoxetine 82 % and 91 % of rejection is found that is comparable with the value of $3A^{IN}$ system.

Thus among all FGs analyzed a high rejection of rac-fluoxetine and glucose is achieved considering $3A^{IN}$, $2B^{IN-OUT}$ and $3B^{IN-OUT}$. Nevertheless it is interesting to compare the values obtained for rac-fluoxetine and glucose molecules with those provided for ethanol and water molecules. In fact the optimization of selectivity and permeability of MWNTs has to maximize the rejection of solutes and minimize the rejection of solvents. Thus, in these terms the system $3A^{IN}$, in which a rejection of 34 % is found for water molecule, is favored than the others in which 42 % and 55 % is found [34].

4.2.5 Conclusions

A selectivity-permeability optimization of OIMs CNT-polymer membranes was carried out in this study; high rejection of organic solutes with low molecular weight without a marked fall in water permeability was the aim of this computational optimization. CNTs with specific diameters and appropriate functional groups have been proposed. This analysis has revealed that the amazing fluid dynamics property of the CNTs are not exploited without a good alignment of the CNTs with respect to the selective surface but also without an accurate and quantitative calibration of the internal and external diameters of MWNTs (much less expensive and with fewer defects with respect to S-DWNTs). The last point is crucial in fact for a chitosan porous membrane was shown that the addition of inappropriate nanotubes (with external diameters too large) lead to a reduction in the membrane performance since the increase of flow through the inner core of MWNTs does not compensate the loss of membrane area which is also highly permeable.

For a TFC membrane the optimization showed instead that a low density of MWNTs with internal diameter of 4.44 nm yielded an enhancement in permeabil-

ity of more than 500 times compared to the membrane without nanotubes. At the same time a high rejection of rac-fluoxetine and glucose molecules is achieved by means of appropriately modified monomers, used in the PIM-1 preparation, as functional groups (Olygomer-IM). As a result, a OIM-functionalized CNT-polymer membrane could result in a more efficient membrane for wastewater treatment, with increased permeability and optimal rejection *versus* solutes with low molecular weight.

Bibliography

- [1] A. Anastassiou, E. K. Karahaliou, O. Alexiadis, V. G. Mavrantzas (2013) *Detailed atomistic simulation of the nano-sorption and nano-diffusivity of water, tyrosol, vanillic acid and p-coumaric acid in single wall carbon nanotubes* J Chem Phys., 139, 164711-16
- [2] N. M. OBoyle, M. Banck, C. A. James, C. Morley, T. Vandermeersch, and G. R. Hutchison (2011) Journal of Cheminformatics, 3:33
- [3] G. De Luca, A. Arbouznikov, A. Goursot, and P. Pullumbi (2011) J. Phys. Chem. B, 105, 4663.
- [4] X. Xu, Q. Zhang, R. P. Muller, W. A. Goddard III (2005) J. Chem. Phys., 122, 014105
- [5] T. P. Straatsma, E. Apra, T. L. Windus, M. E. Dupuis, J. Bylaska, W. de Jong, S. Hirata, D. M. Smith, A. M. Hackler, T. L. Pollack, R. J. Harrison, J. Nieplocha, V. Tipparaju, M. Krishnan, E. Brown, G. Cisneros, G. I. Fann, H. Fruchtl, J. Garza, K. Hirao, R. Kendall, J. A. Nichols, K. Tsemekhman, M. Valiev, K. Wolinski, J. Anchell, D. Bernholdt, P. Borowski, T. Clark, D. Clerc, H. Dachsel, M. Deegan, K. Dyall, D. Elwood, E. Glendening, M. Gutowski, A. Hess, J. Jaffe, B. Johnson, J. Ju, R. Kobayashi, R. Kutteh, Z. Lin, R. Littlefield, X. Long, B. Meng, T. Nakajima, S. Niu, M. Rosing, G. Sandrone, M. Stave, H. Taylor, G. Thomas, J. van Lenthe, A. Wong, Z. Zhang (2005) *NWChem, A Computational Chemistry Package for Parallel Computers* version 6.1.1, Pacific Northwest National Laboratory: Richland, WA.
- [6] S. Simon, M. Duran, J. J. Dannenberg (1996) J. Chem. Phys., 105, 11024

-
- [7] A. Klamt and G. Schüürmann (1993) *J. Chem. Soc. Perkin Trans. 2*, 799
- [8] G. Hummer, J.C. Rasaiah, J.P. Noworyta, (2001) *Water Conduction through the Hydrophobic Channel of a Carbon Nanotube* *Nature*, 414, 188-190
- [9] A. Striolo, (2006) *The Mechanism of Water Diffusion in Narrow Carbon Nanotubes* *Nano Lett.*, 6, 633-639
- [10] M. Whitby, N. Quirke (2007) *Fluid Flow in Carbon Nanotubes and Nanopipes* *Nat. Nano.*, 2, 87-94
- [11] J.A. Thomas, A.J.H. McGaughey (2009) *Water Flow in Carbon Nanotubes: Transition to Subcontinuum Transport* *Phys. Rev. Lett.*, 102, 184502
- [12] D. Mattia, Y. Gogotsi (2008) *Polymers of intrinsic microporosity (PIMs): organic materials for membrane separations, heterogeneous catalysis and hydrogen storages* *Microfluid. Nanofluid.*, 5, 289-305
- [13] D. Mattia, F. Calabr (2012) *Explaining high flow rate of water in carbon nanotubes via solidliquid molecular interactions* *Microfluid. Nanofluid.*, 13, 125-130
- [14] B. Corry (2007) *Designing Carbon Nanotube Membranes for Efficient Water Desalination* *The Journal of Physical Chemistry B*, 112, 1427-1434
- [15] M. Majumder, N. Chopra, R. Andrews, B.J. Hinds (2005) *Nanoscale hydrodynamics: Enhanced Flow in Carbon Nanotubes* *Nature*, 438, 44.
- [16] J.K. Holt, H.G. Park, Y. Wang, M. Stadermann, A.B. Artyukhin, C.P. Grigoriopoulos, A. Noy, O. Bakajin (2006) *Fast Mass Transport Through Sub-2-Nanometer Carbon Nanotubes* *Science*, 312, 1034-1037.
- [17] M. Whitby, L. Cagnon, M. Thanou, N. Quirke (2008) *Enhanced Fluid Flow through Nanoscale Carbon Pipes* *Nano Lett.*, 8, 2632-2637
- [18] K.P. Lee, T.C. Arnot, D. Mattia (2011) *A review of reverse osmosis membrane materials for desalination—Development to date and future potential* *J. Membr. Sci.*, 370, 1-22.

- [19] J.-H. Choi, J. Jegal, W.-N. Kimb (2006) *Fabrication and characterization of multi-walled carbon nanotubes/polymer blend membranes* Journal of Membrane Science 284, 406415
- [20] H. A. Shawky, S.-R. Chae, S. Lin, M. R. Wiesner (2011) *Synthesis and characterization of a carbon nanotube/polymer nanocomposite membrane for water treatment* Desalination 272, 4650
- [21] W.-H. Li, X.-H. Chen, C.-S. Chen, L.-S. Xu, Z. Yang, Y.-G. Wang (2008) *Preparation and Shear Properties of Carbon Nanotubes/Poly(butyl methacrylate) Hybrid Material* POLYMER COMPOSITES, 972-977
- [22] G. De Luca, E. Tocci, E. Drioli (2005) *Quantum and molecular mechanics calculations on modified silica nano ring* J. Mol. Struct., 739, 163-172
- [23] M. Majumder, N. Chopra, B.J. Hinds (2005) *Effect of Tip Functionalization on Transport through Vertically Oriented Carbon Nanotube Membranes* J. Am. Chem. Soc., 127, 9062-9070
- [24] H. Wu, B. Tang, P. Wu (2013) *Optimization, characterization and nanofiltration properties test of MWNTs/polyester thin film nanocomposite membrane* J. Membr. Sci., 428, 425-433
- [25] C. Tang, Q. Zhang, K. Wang, Q. Fu, C. Zhang (2009) *Water transport behavior of chitosan porous membranes containing multi-walled carbon nanotubes (MWNTs)* J. Membr. Sci., 337, 240247
- [26] Y. Saito, T. Yoshikawa, S. Bandow, M. Tomita, T. Hayashi (1993) *Interlayer spacings in carbon nanotubes* Phys. Rev. B 48, 3, 19071909
- [27] J.A. Thomas, A.J.H. McGaughey, O. Kuter-Arnebeck (2010) *Pressure-driven water flow through carbon nanotubes: Insights from molecular dynamics simulation* International Journal of Thermal Sciences, 49, 281-289
- [28] S. Joseph, N.R. Aluru (2008) *Why Are Carbon Nanotubes Fast Transporters of Water?* Nano Lett., 8, 452-458
- [29] W.D. Nicholls, M.K. Borg, D.A. Lockerby, J.M. Reese (2012) *Water transport through carbon nanotubes with defects* Mol. Simul., 38, 2012, 781-785

-
- [30] D. Mattia, M.P. Rossi, B.M. Kim, G. Korneva, H.H. Bau, Y. Gogotsi (2006) *Effect of Graphitization on the Wettability and Electrical Conductivity of CVD Carbon Nanotubes and Films* J. Phys. Chem. B, 110, 9850-9855
- [31] W. Nicholls, M. Borg, D. Lockerby, J. Reese (2012) *Water transport through (7,7) carbon nanotubes of different lengths using molecular dynamics* Microfluid. Nanofluid., 12, 257-264
- [32] J.A. Thomas, A.J.H. McGaughey (2008) *Reassessing Fast Water Transport Through Carbon Nanotubes* Nano Lett., 8, 2788-2793
- [33] N. B. McKeown and P. M. Budd (2006) *Polymers of intrinsic microporosity (PIMs): organic materials for membrane separations, heterogeneous catalysis and hydrogen storage* Chem. Soc. Rev., 35, 675683
- [34] F. Bisignano, D. Mattia, G. De Luca *Selectivity-permeability optimization of functionalised CNTpolymer membranes for water treatment: a modelling study (to be submitted)*
- [35] H. Kuzmany, A. Kukovecz, F. Simon, M. Holzweber, C. Kramberger, T. Pichler (2004) *Functionalization of carbon nanotubes* Synth Met 114, 113122
- [36] E. Chemecka, K. Pasterny, T. Kupka, L. Stobiski (2012) *OH-functionalized open-ended armchair single-wall carbon nanotubes (SWCNT) studied by density functional theory* J Mol Model 18, 14631472
- [37] J.C. Slater and K. H. Johnson (1972) Phys. Rev. B 5, 844
- [38] K. Kitaura and K. Morokuma (1976) *A new Energy Decomposition Scheme for Molecular Interactions within the Hartree-Fock Approximation* International Journal of Quantum Chemistry, X, 325-340
- [39] S. Dapprich, I. Komromi, K. S. Byun, K. Morokuma and M. J. Frisch (1999) *A New ONIOM Implementation in Gaussian 98. Part 1. The Calculation of Energies, Gradients and Vibrational Frequencies and Electric Field Derivatives* J. Mol. Struct. (Theochem) 462, 1

Chapter 5

Bromide ion exchange with a Keggin polyoxometalate on functionalized polymeric membranes

Submitted to *Journal of Physical Chemistry* [1]

5.1 Introduction

The exchange of ions on polymeric surface is a topic of considerable interest, thanks to the broad range of applications. In particular, the anions exchange on membrane surfaces may offer new possibilities for the development of novel functionalized membranes. In fact, polymeric surface modification by binding specific functional groups represents a widely used procedure for membrane preparation with peculiar functions [2, 3, 4, 5, 6, 7]. Moreover, many studies have been devoted on the use of various additives, including nanoparticles, and specific coatings of existing membranes. Thus, target surface properties such as antimicrobial, catalytic activity and hydrophobicity can be imparted to the membranes. In this frame, innovative nanostructures would definitely make a leap forward. For example, the replacement of ions, without particular features, with functional nanosized

polyanions may represent an efficient strategy for the design of novel polymeric membranes. Therefore, this work aims to describe noncovalent short-range interactions involved in the exchange, on a polymer surface, of the bromide with the polyoxometalate $[PMo_{12}O_{40}]^{3-}$.

Polyoxometalates (POMs) are polyanionic metal oxides and are widely used for the preparation of hybrid materials, owing to their large versatility in terms of tunable structural features and properties. Specifically, polyoxo vanadates and molybdates are promising antibacterial agents [8, 9, 10, 11]. Their biological activity arises from the electrostatic interactions with biological molecules and from their redox behavior, which can be exploited for the oxidations of organic substrates [12, 13, 14] including cellular components [15]. In particular, the $[PMo_{12}O_{40}]^{3-}$ is a Keggin heteropolyanion with high redox potential, which has already been used for the preparation of antimicrobial films [11].

A polymerisable bicontinuous microemulsion (PBM) membrane was taken as membrane reference prepared by using acryloyloxyundecyltrimethyl ammonium bromide (*AUTMAB*) surfactant together with specific cosurfactants, monomers, cross-linkers and water. The positive charged surfactant is typically outweighed by bromide ion and the surfactant-bromide adduct is located in aqueous phase of the microemulsion. The bromide ion, linked to the positive charged heads of surfactants by noncovalent electrostatic interactions, may be exchanged with other water soluble and functional anions, (such as the Keggin heteropolyanion). In this way, the surfactants may be used as a hook to anchor nanoparticles on the surface of the polymeric membrane.

A computational study on the exchange of Br^- with this Keggin heteropolyanion is presented in this thesis. A detailed theoretical analysis of the noncovalent interactions controlling the anion exchange was carried out. Following previous positive results [16, 17, 18, 19], describing hydrogen bonds in membranes (theory level [20, 21, 22, 23] and geometric models), Quantum Mechanics (QM), in the frame of Density Functional Theory (DFT), and Molecular Mechanics (MM) calculations were performed in this contribution. In particular, the MM simulations provided the most probable conformer of the *AUTMAB* surfactant which was used in the subsequent DFT calculations to assess accurately the interactions of the *AUTMAB* with the $[PMo_{12}O_{40}]^{3-}$ or Br^- anions. The electronic hydration energy of

these anions were also evaluated, at the same level of theory. Finally, energy balances were carried out and the exchanging probability of Br^- with the $[PMo_{12}O_{40}]^{3-}$, at neutral pH, was predicted at qualitative level. The final aim of this work is to figure out whether a good adhesion of the nanosized metal oxide can occur on the functionalized polymeric surface without loss of the antibacterial activity. In fact, an efficient exchange, on the membrane surface, with antibacterial nanoparticles definitely allows to increase the membranes efficiency by reducing the fouling caused by microorganisms; particularly harmful during wastewater purification processes.

5.2 Molecular models and computational details

The optimization of hydrated $[PMo_{12}O_{40}]^{3-}$ geometry and the *AUTMAB* conformational research were the first step of this work. The research of the surfactants conformers was carried out at MM level by using the same procedure used for the organic compounds reported in chap. 4.1 sec. 4.1.3. In Fig. 5.1 the geometry of the most probable *AUTMAB* conformer, i.e. the surfactant with 11 atoms in the carbon chain, obtained by the MM conformational analysis is reported. The conformational research was carried out holding blocked the unsaturated group of the *AUTMAB*, used for the polymerization, in order to simulate the surfactant entrapment in the polymer matrix. Conversely, the polar head, represented by the positive ammonium polar head, $-N^+(CH_3)_3$, and the carbon chain was left completely free to move. The most stable conformer found is quite linear regardless its carbon chain length, although the surfactant with 16 carbon atoms in the aliphatic chain (not reported here) is more twisted with respect to the *AUTMAB*. This preliminary analysis indicates that no special windings of the surfactants around the polyanionic nanoparticle should be expected; especially considering the *AUTMAB* with 11 carbon atoms.

After the conformational research, the number of water molecule around $[PMo_{12}O_{40}]^{3-}$ and their arrangement was evaluated. The assessment of the water disposition around POM is an important point for the subsequent calculations. Up to now, calculations on a similar large nanosystem have used mixed QM/MM approaches

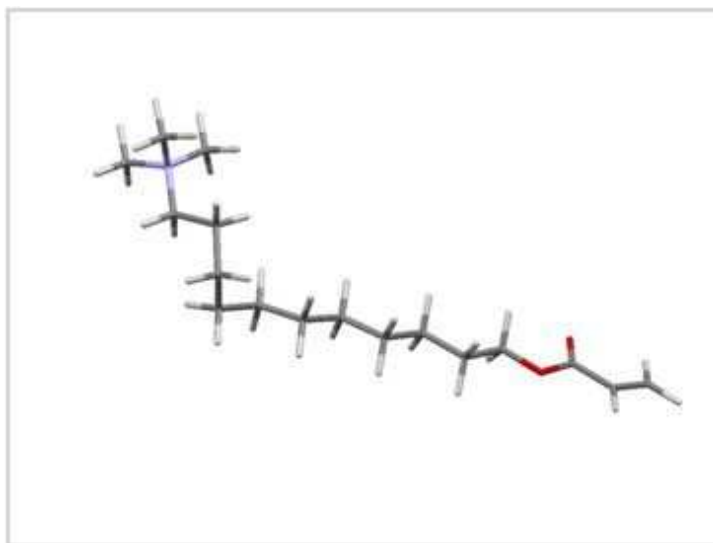


Figure 5.1: Most probable conformer of *AUTMAB* surfactant. Carbon atoms in grey colour, oxygen atoms in red, nitrogen atom in blue, hydrogen atoms in white.

[24, 25]. However, Miro' *et al.* [26] recently studied, in detail, the hydration of similar Keggin anions analyzed through an explicit solvent model. The explicit solvent model, used by these authors, includes the molecules of water in the solvation shell explicitly, and long-range bulk effects and counter ions as a set of single point charges. Miro' *et al.* [26] compared their results with those obtained by using the Conductor-like Screening Model (COSMO) [27], finding a good agreement. A similar approach was used in this thesis with the exception, with respect to Miro' *et al.* work, that the long-range effects were taken into account by using the COSMO approach. Miro' *et al.* showed that the number of hydrogen bonds between the water molecules and polyoxometalate significantly increase going from a first shell of 24 molecules to an outer shell of 49, whereupon these bonds between water and polyoxometalate remain nearly constant, whereas the H-bonds among water molecules significantly increase as well shown in Fig. 2 of the Miro' *et al.* paper [26]. Thus, here, 36 water molecules, i.e. an average value between the above first and outer solvation shells, have been placed around the POM. It is worth noting that the optimization of the geometries of a number of water molecules greater than 36 by using a pure quantum mechanics method becomes prohibitively expensive. Every water molecule was bonded to each external POM

oxygen atom by a typical H-Bond distance [28, 29, 30, 31] and random dihedral angles were defined. As outlined above, a supra-molecular model is used in which the closest water molecules are explicitly considered, whereas all the other water molecules are taken into account by the COSMO model. It is important to consider that the supra-molecular structure, i.e. POM and 36 water molecules, allows the use of the bulk water dielectric constant, i.e. 80.2 in the COSMO calculations, preventing to take into account the non-linear polarization effects of the dielectric constant when multi-charged solutes are in solution. Moreover, the use of a pure quantum mechanics approach to describe the above supra-molecular structure guarantees a certain reliability of the results, mainly in relation to the hydrogen bonds formed by water with the POM. Thus, a full quantum optimization of all the water molecules was carried out using a hybrid energy functional, X3LYP [32], whereas the polyoxometalate was kept stuck during the optimization. DFT calculations were performed using linear combinations of Gaussian-type orbitals, and the Coulomb and exchange-correlation potentials were numerically integrated on an adaptive grid with medium accuracy. Double- ξ orbital bases were employed for the phosphorous and internal oxygen atoms of the POM, instead, double- ξ orbital basis with a polarization function were employed for the external oxygen atoms and for water molecules. For the molybdenum atoms, the Stuttgart RSC 1997 effective core potentials were used. The energy convergence for the self-consistent field procedure and the root-mean square of the electron density thresholds were set to 10^{-6} (a.u.) and to $2 \cdot 10^{-5}$ (a.u.), respectively. The geometry was optimized by using analytical energy gradients and the quasi-Newton optimization with approximate energy Hessian updates. The convergence criteria for the geometry optimization are the maximum and root-mean-square gradient thresholds of $4.5 \cdot 10^{-3}$ and $3.0 \cdot 10^{-3}$, respectively, in conjunction with the maximum and root-mean square of the nucleus Cartesian displacement vectors with thresholds of $5.4 \cdot 10^{-3}$ and $3.6 \cdot 10^{-3}$ (a.u.), respectively. As above mentioned, the COSMO solvent model, proposed by Klamt and Schüürmann [27], was used to evaluate the electronic free energies of the hydrated POM and Br^- . The cavity, in which the hydrated anions, i.e. the supra-molecular structures, were located, is defined as interlocking atomic spheres constructed by using specific atomic radii. The default radii implemented in the NWChem package [33] were used. The use of these radii

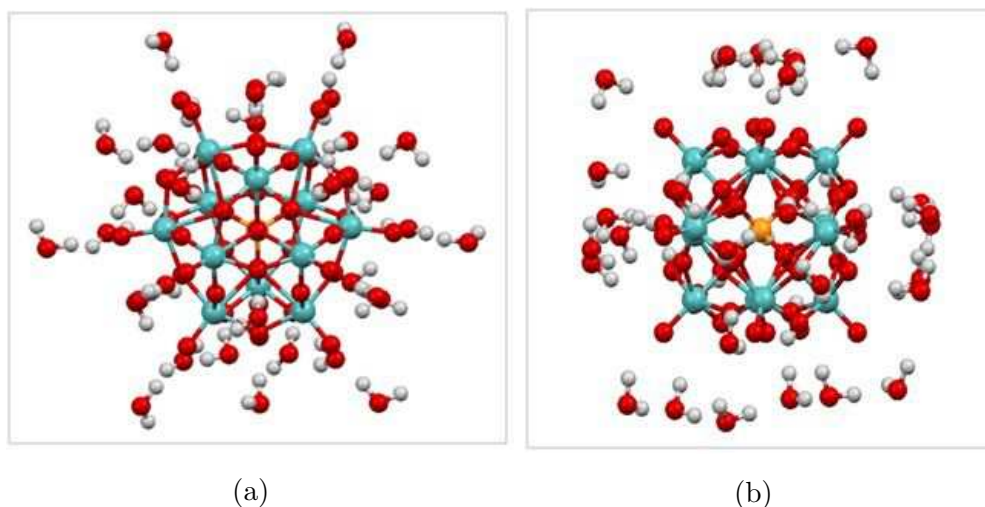


Figure 5.2: Initial (a) and DFT optimized geometries (b) of the hydrated $[PMo_{12}O_{40}]^{3-}$ (POM^{hyd}). Oxygen atoms in red colour, molybdenum atoms in blue, hydrogen atoms in white, phosphorous atom in yellow.

justifies the utilization of an “accessibility solvent parameter” for water molecules equal to 1.3 Å. In Fig. 5.2 the initial and optimized geometries of the hydrated polyoxometalate are presented, respectively. In the geometry optimization of the hydrated nanoparticle (POM^{hyd}) it is evident that the water molecules move away from the POM oxygen atoms forming simultaneously molecular clusters with each other (Fig. 5.2a). The most open structure of the hydrated anion allows to identify some oxygen atoms on the $[PMo_{12}O_{40}]^{3-}$ surface which are less hindered by water. These atoms were afterwards chosen to bind with the surfactant molecules. Conversely, the optimized hydrated POM allows to identify some parts of the POM surface more covered by the water molecules, i.e. water clusters, through which the nanoparticle could bind to the supports by means of H-Bonds formed by water. These two possible attacks were then used to define the starting geometries of the $POM^{hyd} \dots AUTMAB$ adducts for the next optimizations.

Finally, the energies associated to the noncovalent interactions between $[PMo_{12}O_{40}]^{3-}$ and $AUTMAB$ as well between Br^- and surfactant (i.e. the ΔE_{int}) were evaluated as the difference between the energy of the adduct (anions and surfactants) and those of the isolated single components. The basis set superposition error was also included in the calculations of the interaction energies according to the counterpoise

Table 5.1: Short-range noncovalent interactions energies involved in the anionic exchange.

Adduct	Total Charge	ΔE_{int} ($kcal \cdot mol^{-1}$)
$(PMO_{12}O_{40})^{hyd} \dots AUTMAB_3$	0	-324.81
$(PMO_{12}O_{40})^{hyd} \dots AUTMAB_1$	-2	-112.50
$(PMO_{12}O_{40})^{hyd} \dots H_2O \dots AUTMAB_1$	-2	-119.98
$Br \dots AUTMAB_1$	0	-90.62
$Br^{hyd} \dots H_2O \dots AUTMAB_1$	0	-85.16

Table 5.2: Anion solvation free energies.

Molecule	$\Delta G_{sol.}$ ($kcal \cdot mol^{-1}$)
$(PMO_{12}O_{40})^{-3}$	-226.08
* Br^-	-56.81

method [34].

5.3 Results and discussions

The electrostatic long-range interactions, formed between a charged surface and the negatively charged nanoparticles, are weaker than short-range interactions [35, 36]; in particular this work was focused on the short-range interactions involved in the anions exchange. To this aim, the optimized geometry of the POM^{hyd} and the most probable conformer structure were used.

The results of the quantum calculations are reported in Tab. 5.1 and 5.2. The first value, in Tab. 5.1, is referred to the energy associated to the interaction among three polar heads of surfactants and the polyanion, as shown in Fig. 5.3. The subsequent energies are instead referred to the linkage between one surfactant molecule and the POM^{hyd} , by using two different starting structures. Precisely, in the $(PMO_{12}O_{40})^{hyd} \dots AUTMAB_1$ adduct, the atoms chosen to bond with the surfactant were the freest oxygens atoms of the hydrated nanoparticle, i.e. no water molecule directly connected with them in the optimized geometry of POM^{hyd} . Conversely, in the $(PMO_{12}O_{40})^{hyd} \dots H_2O \dots AUTMAB_1$ and $Br^{hyd} \dots H_2O \dots AUTMAB_1$, the atoms chosen

*Considering the first solvation shell Br^- ($5H_2O$) in the most stable configuration

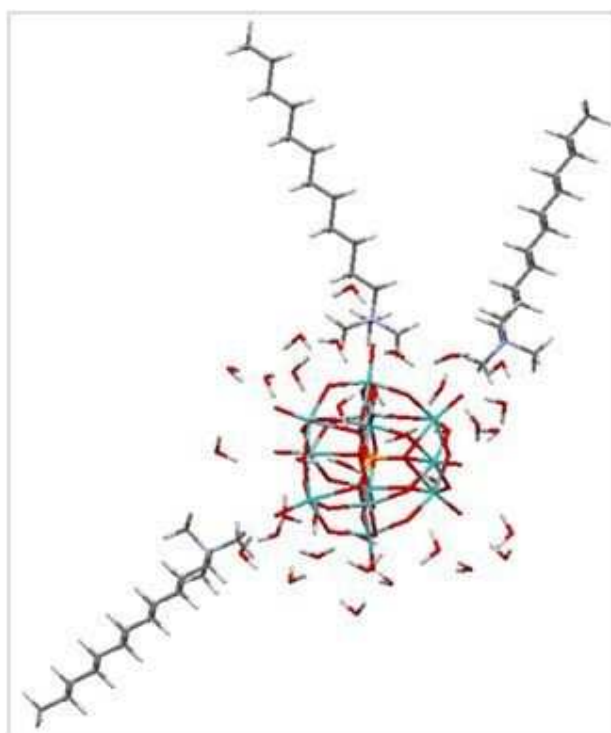


Figure 5.3: $(PMo_{12}O_{40})^{hyd} \dots AUTMAB_3$ adduct formed by three surfactant molecules and POM^{hyd} .

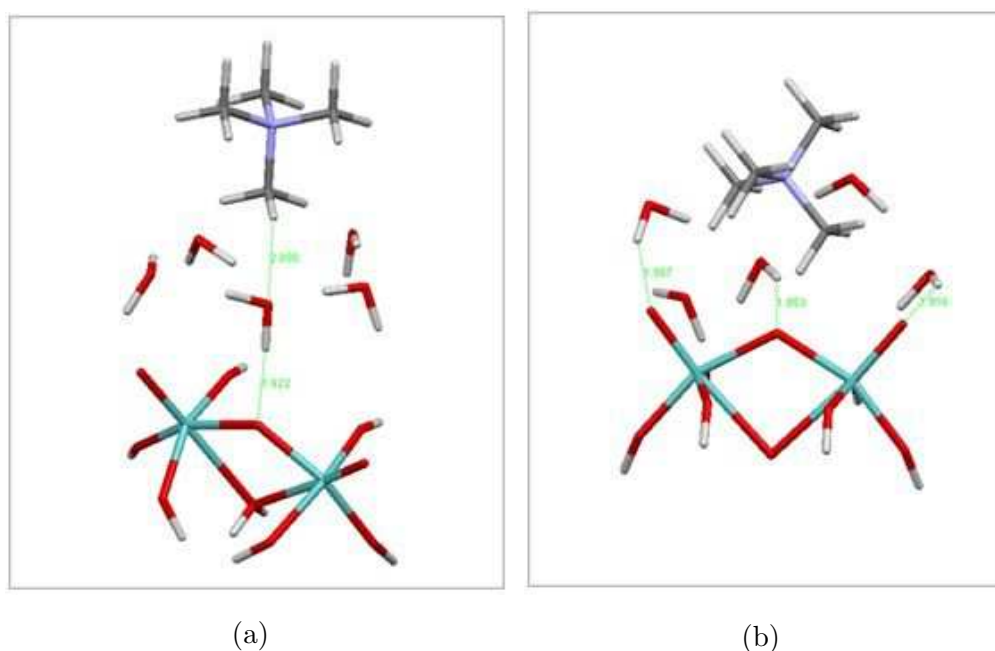


Figure 5.4: Initial (a) and DFT optimized geometries (b) of a POM model and surfactant polar head. Bridge water molecule is considered in the initial geometry.

were an oxygen of POM^{hyd} directly bonded with a water molecule, that in turn is linked with a hydrogen atom of the surfactants methyl group, i.e. the water molecule is considered a bridge between POM and polar head, as shown in Fig. 5.4 and Fig. 5.5 (as regard the bromide).

It is worth noting that these configurations (water as a bridge), as well as, the aforementioned direct link are only referred to the starting geometries used for the subsequent quantum optimizations. In fact, the interaction energies, as reported in Tab. 5.1 were calculated by using the optimized geometries in which the water molecules, both in the direct and indirect linkages, have moved. The use of two starting geometries is used only to understand how these influence the short-range interaction energies. Moreover, in the $(PM_{O_{12}O_{40}})^{hyd} \dots AUTMAB_3$ and $(PM_{O_{12}O_{40}})^{hyd} \dots AUTMAB_1$ adducts, the maximum and minimum number of noncovalent interactions between the surfactants and the antimicrobial particle are considered, respectively. The number of surfactants which coordinate the polyanion determines the total charge of the adduct. Hence, the $(PM_{O_{12}O_{40}})^{hyd} \dots AUTMAB_3$ has a total charge equal to 0, whereas the total charge of the $(PM_{O_{12}O_{40}})^{hyd} \dots AUTMAB_1$

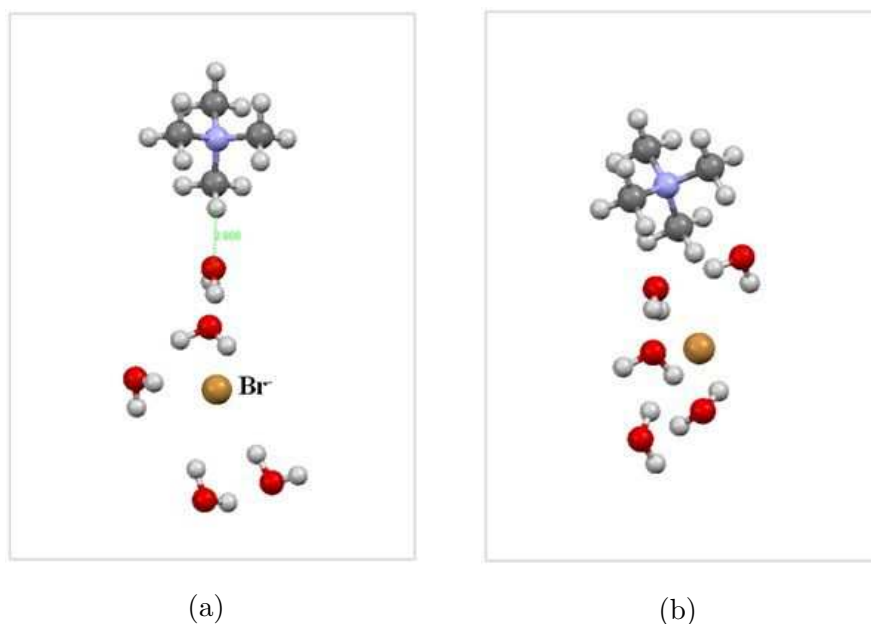


Figure 5.5: Initial (a) and DFT optimized geometries (b) of a surfactant polar head and Br^- ion. Bridge water molecule is considered in the initial geometry.

is equal to -2. The Na^+ ions, in solution, counterbalance the charge of the last adduct.

The interaction energies of Tab. 5.1, show that both $(PMo_{12}O_{40})^{hyd} \dots AUTMAB_3$ and $(PMo_{12}O_{40})^{hyd} \dots AUTMAB_1$ adducts interact with the surfactant molecules more effectively than the Br^- ion. The starting geometries do not affect this trend. However, this comparison does not take into account the solvation of ions. Thus, for a correct analysis, the solvation energies must be considered. The energy balance between ΔE_{int} and $\Delta G_{sol.}$, shown in Tab. 5.1, provides, therefore, information on the relative stability of the ions. The energy balance shows that for the $(PMo_{12}O_{40})^{hyd} \dots AUTMAB_1$ or $(PMo_{12}O_{40})^{hyd} \dots H_2O \dots AUTMAB_1$ adducts, i.e. considering a low density of surfactant on the polymeric surface, there is no net energy gain with respect to the hydrated POM. This means that the nanoparticle is more stable in water than attached to just one surfactant independent on the type of noncovalent short-range interaction. Instead, the energy balance, referred to the $(PMo_{12}O_{40})^{hyd} \dots AUTMAB_3$ adduct, shows that in this case there is a net energy gain, that is the POM interacting with 3 surfactants is more stable with respect

to the hydrated in the solvent bulk. As a result, with a high density of surfactant molecules on the polymeric surface, the nanoparticle is likely to be absorbed. However, this energy balance has to be compared with the balance referred to the bromide. The difference between ΔE_{int} and ΔG_{sol} for the $(PM_{O_{12}O_{40}})^{hyd} \dots AUTMAB_3$ adduct, is equal to -98.73 ($kcal \cdot mol^{-1}$), whereas the same difference, referred to the $Br \dots AUTMAB_1$ adduct is equal to -33.81 ($kcal \cdot mol^{-1}$). This value, nevertheless, is related to the exchange of a single Br^- ion, therefore it cannot be compared with the energy difference associated to the $(PM_{O_{12}O_{40}})^{hyd} \dots AUTMAB_3$ anion. It must be multiplied by 3 because every POM particle should break 3 interactions between Br^- surfactant. Thus, the final Br^- energy's balance is -101.43 ($kcal \cdot mol^{-1}$). These two balances are comparable within the limits of calculation error. In conclusion, there is no net energy gain if 3 Br^- ions are exchanged with a POM nanoparticle.

In these balances, the energy required to rearrange the water molecules around the POMs particle and Br^- should be considered. The assessment of this quantity through a pure quantum mechanics approach is very difficult and it would be inaccurate as it depends on a large time-space scale. In any case, this energy should be provided to the nanoparticle to reorganize the surrounding water molecules from the non-interacting hydrated POM configuration (shown in Fig. 5.2b) to the interacting POM^{hyd} structure, as shown in Fig. 5.3, at least as regards the optimized water molecules close to the interaction sites. Thus, the $(PM_{O_{12}O_{40}})^{hyd} \dots AUTMAB_3$ energy balance (i.e. -98.73 ($kcal \cdot mol^{-1}$)) should be reduced by the energy required to reorganize the water molecules when the nanoparticle interacts with surfactants. Nevertheless, this energy was estimated by using the optimized water geometries obtained by utilizing the models shown in Fig. 5.4b and 5.5b as regards the bromide. The energy required to move the water molecules was evaluated as difference between the energy, associated to the non-interacting POM^{hyd} (Fig. 5.2b) and the interacting POM^{hyd} energy, i.e. the energy of the nanoparticle reported in Fig. 5.3. The position of 5 water molecules, i.e. those involved in the $(PM_{O_{12}O_{40}})^{hyd} \dots H_2O \dots AUTMAB_1$ interaction, were optimized, along with the surfactant polar head, by using the aforementioned model. This energy difference is 38.55 ($kcal \cdot mol^{-1}$). Hence, by considering the energies required to move the water molecules around the POM and Br^- ion (i.e. 2.75 ($kcal \cdot mol^{-1}$)), although evaluated in an approximate way, the balance is unfavorable for the POM either

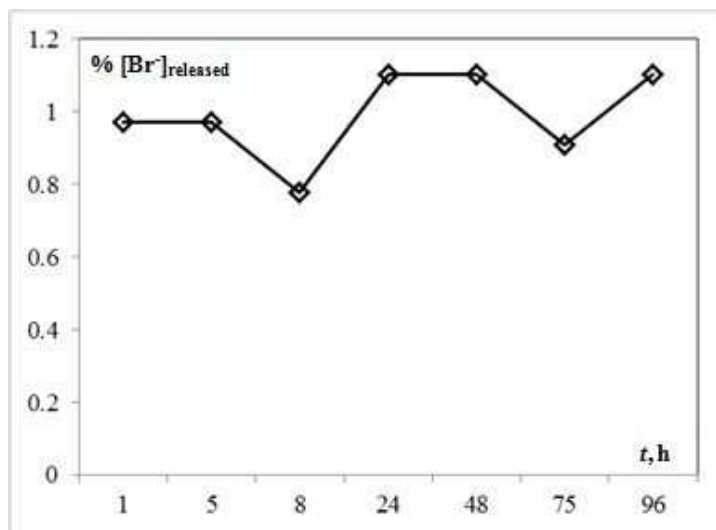


Figure 5.6: Relative concentrations of Br^- ion (%) released in the POM solution respect to the time.

considering high or low density of surfactant. Though the maximum number of noncovalent interactions between surfactant and $[PMo_{12}O_{40}]^{3-}$ is considered, the computed energy gain is not so large to compensate the energy required to shift the Br^- from the surfactant polar head. From a macroscopic point of view, this means that the bromide-POM exchange is unfavorable or forbidden.

Finally, to validate the theoretical conclusions, a comparison with *ad hoc* measurements carried out using homemade membranes in order to control the chemical composition of all the components involved in the exchange process, was made. Practically, a solution of $[PMo_{12}O_{40}]^{3-}$ in distilled water was prepared, and the membrane was dipped in the solution and allowed to stand in direct infusion for 96 hours, while continuously stirring with a magnetic bar. Then analytical measurements were performed to assess the anionic exchange. The measurements are based on the gravimetric analysis of the Br^- released in 4 days by the membrane as a consequence of the exchange with $[PMo_{12}O_{40}]^{3-}$ at neutral pH.

The concentrations of Br^- , released in aqueous phase, are expressed as a function of the time and relating to the initial amount of bromide used in the PBM membrane preparation (Fig. 5.6). As evident in Fig. 5.6, the anionic exchange took place during the first hour of the experiment. In fact, the percentage of the

released bromide reaches a constant value, *ca.* 1%, after the first hour and it is remained constant, within the uncertainty of measurements, for the whole period of the experiment. Another important aspect to be observed is related to the concentration of the reagents involved in the exchange process. In particular, the millimoles of starting bromide are in large excess (i.e. 2.46 mmol) compared to those of POM (i.e. 0.096 mmol). Nevertheless, the millimoles of bromide detected at the end of the process (i.e. after 96 hours) are just 0.024 mmol. This value is a quarter of the millimoles of POM dissolved at the beginning of the experiment. This means that most of the POM remained in solution confirming that the exchange is not favored. It is worth noting that a low concentration of POM was used in the analytical measurements to avoid the smallest precipitation of nanoparticles as sodium salt. Thus, the agreement between the theoretical conclusion and experimental data was remarkable. In addition, the exchange process was measured considering the PBM membrane submerged in the POM solution at constant room temperature and without water flow. In these conditions, physical adsorption of POM should be excluded by comparing the effective diameter of the POM^{hyd} , i.e. 2.36 nm, evaluated by the algorithm reported in sec. 3.2 and the average pore size of the membrane of about 20 nm, measured by means of a capillary flow porometer Mod.1500AEXL (USA) PMI.

5.4 Conclusion

Noncovalent interactions between the Keggin polyoxometalate, $[PMo_{12}O_{40}]^{3-}$, Br^- and *AUTMAB* surfactants were evaluated in the frame of Density Function Theory. In addition, solvation energy of the anions were evaluated at the same level of theory. Energy balances were theoretically assessed in order to predict a probable exchange between bromide and $[PMo_{12}O_{40}]^{3-}$, on the polymeric surface. The quantum calculations predict that there is no net energy gain if the Br^- ion is exchanged with POM^{hyd} . This is evident when a low density of surfactant is considered on the polymeric surface. Instead, for high surfactant density the energy loss due to this exchange is less marked. However, if the energy involved in the rearrangement of the water molecules, around the POM, is also considered, the balance is still unfavorable for the $[PMo_{12}O_{40}]^{3-}$ anion exchange. In order to verify

this theoretical prediction a comparison with experimental measurements based on the gravimetric analysis of the Br^- anion was made. The agreement between the theoretical conclusion and experimental data was remarkable. In fact, this analysis showed that the exchange takes place in a very low extent. This study is important because it helps to select tailored nanosized particles and polymer functionality, through an *ab-initio* methodology free from any adjustable parameter, in order to optimize the exchange between ions and to improve the polymer surface properties.

Bibliography

- [1] G. De Luca, F. Bisignano, A. Figoli, F. Galiano, E. Furia, R. Mancuso, O. Saoncella, M. Carraro, M. Bonchio, and B. Gabriele (2013) *Bromide ion exchange with a Keggin polyoxometalate on functionalized polymeric membranes: a theoretical and experimental study* Journal of Physical Chemistry (submitted, Manuscript ID: jp-2013-11401v)
- [2] E. Berndt, S. Behnke, A. Dannehl, A. Gajda, J. Wingender, M. Ulbricht (2010) *Polymer*, 51, 5910.
- [3] E. Berndt, S. Behnke, M. Ulbricht (2011) *Eur. Polym. J.*, 47, 2379
- [4] H. Borchering, H. G. Hicke, D. Jorcke, M. Ulbricht (2002) *Desalination*, 149, 297.
- [5] H. Urch, C. Geismann, M. Ulbricht, M. Epple (2006) *Materialwissenschaft und Werkstofftechnik*, 37, 422.
- [6] P. D. Peeva, A. E. Palupi, M. Ulbricht (2011) *Separ. Purif. Technol.*, 81, 124.
- [7] N. Hassan, T. Bahnert, A. Wego, J. S. Gutmann, M. Ulbricht (2012) *Appl. Surf. Sci.*, 259.
- [8] N. Fukuda, T. Yamase (1997) *Biol. Pharm. Bull.*, 20, 927-930.
- [9] F.-C. Yang, K.-H. Wu, W.-P. Lin, M.-K. Hu (2009) *Micropor. Mesopor. Mat.*, 118, 467-472.
- [10] K. H. Wu, P. Y. Yu, C. C. Yang, G. P. Wang, C. M. Chao (2009) *Polym. Degrad. Stab.*, 94, 1411-1418.

- [11] Y. Kong, L. Pan, J. Peng, B. Xue, J. Lu, B. Dong (2007) *Mat. Lett.*, 61, 23932397.
- [12] M. Carraro, A. Sartorel, M. Ibrahim, N. Nsouli, C. Jahier, S. Nlate, U. Kortz, M. Bonchio (2012) *Innovative Catalysis in Organic Synthesis Oxidation, Hydrogenation, and C-X Bond Forming Reactions* Ed: P. Andersson, Wiley-WCH, pp 1-25.
- [13] I. A. Weinstock (1998) *Chem. Rev.*, 98, 113170.
- [14] R. Neumann, A. M. Khenkina (2006) *Chem. Commun.*, 2529-2538.
- [15] J. T. Rhule, C. L. Hill, D. A. Judd, R. F. Schinazi (1998) *Chem. Rev.*, 98, 327-357.
- [16] G. De Luca, L. Donato, S. Garca Del Blanco, F. Tasselli, and E. Drioli (2011) *J. Phys. Chem. B*, 115, 9345. [dx.doi.org/10.1021/jp2006638](https://doi.org/10.1021/jp2006638).
- [17] G. De Luca, A. Gugliuzza, E. Drioli (2009) *J. Phys. Chem. B* 2009, 113, 5473.
- [18] A. Gugliuzza, G. De Luca, E. Tocci, L. De Lorenzo, E. Drioli (2007) *J. Phys. Chem. B*, 111, 8868.
- [19] G. De Luca, E. Tocci, E. Drioli (2005) *J. Mol. Struct.*, 739, 163
- [20] T. van der Wijst, C. Fonseca Guerra, M. Swart, F. M. Bickelhaupt (2006) *Chem. Phys. Lett.*, 426.
- [21] Y. Leng, P. S. Krstic, J. C. Wells, P. T. Cummings, D. J. Dean (2005) *J. Chem. Phys.*, 122, 244721.
- [22] C. Fonseca Guerra, F. M. Bickelhaupt, J. G. Snijders, E. J. Baerends (2000) *J. Am. Chem. Soc.*, 122, 4117.
- [23] Y. Zhao, D. G. Truhlar (2005) *J. Phys. Chem. A*, 109, 5656.
- [24] X. Lopez, C. Nieto-Draghi, C. Bo, J. Bonet Avalos, J. M. Poblet (2005) *J. Phys. Chem. A*, 109, 1216.
- [25] F. Leroy, P. Miro', J. M. Poblet, C. Bo, J. Bonet Avalos (2008) *J. Phys. Chem. B*, 112 (29), 8591, [doi:10.1021/jp077098p](https://doi.org/10.1021/jp077098p). PMID:18590304.

- [26] P. Miro', J. M. Poblet, J. Bonet Avalos, and C. Bo (2009) *Can. J. Chem.*, 87: 1296, doi:10.1139/V09-059.
- [27] A. Klamt and G. Schüürmann (1993) *J. Chem. Soc. Perkin Trans. 2*, 799.
- [28] S. J. Grabowski, T. L. Robinson, J. Leszczynski (2004) *J. Chem. Phys. Lett.*, 386, 44.
- [29] S. J. Grabowski, W. A. Sokalski, J. Leszczynski (2005) *J. Phys. Chem. A*, 109, 4331.
- [30] S. J. Grabowski, W. A. Sokalski (2005) *J. Phys. Org. Chem.*, 18, 779.
- [31] W. R. Gora, S. J. Grabowski, J. Leszczynski (2005) *J. Phys. Chem. A*, 109, 6397.
- [32] X. Xu, Q. Zhang, R. P. Muller, W. A. Goddard III (2005) *J. Chem. Phys.*, 122, 014105
- [33] T. P. Straatsma, E. Apra, T. L. Windus, M. E. Dupuis, J. Bylaska, W. de Jong, S. Hirata, D. M. Smith, A. M. Hackler, T. L. Pollack, R. J. Harrison, J. Nieplocha, V. Tipparaju, M. Krishnan, E. Brown, G. Cisneros, G. I. Fann, H. Fruchtl, J. Garza, K. Hirao, R. Kendall, J. A. Nichols, K. Tsemekhman, M. Valiev, K. Wolinski, J. Anchell, D. Bernholdt, P. Borowski, T. Clark, D. Clerc, H. Dachsel, M. Deegan, K. Dyall, D. Elwood, E. Glendening, M. Gutowski, A. Hess, J. Jaffe, B. Johnson, J. Ju, R. Kobayashi, R. Kutteh, Z. Lin, R. Littlefield, X. Long, B. Meng, T. Nakajima, S. Niu, M. Rosing, G. Sandrone, M. Stave, H. Taylor, G. Thomas, J. van Lenthe, A. Wong, Z. Zhang (2005) *NWChem, A Computational Chemistry Package for Parallel Computers* version 6.1.1, Pacific Northwest National Laboratory: Richland, WA.
- [34] S. Simon, M. Duran, J. J. Dannenberg (1996) *J. Chem. Phys.*, 105, 11024.
- [35] C.J Cramer, D.G. Truhlar (1997) *Theoretical Chemistry Accounts* Symposium Report, 98, 206.
- [36] G. De Luca, F. Bisignano, F. Paone, S. Curcio (2013) *J. Membr. Sci.*, <http://dx.doi.org/10.1016/j.memsci.2013.09.061i>.

Chapter 6

Conclusions

The application of nanostructures in last years is growing in several areas. In the field of wastewater treatment nanoenhanced membranes are receiving wide attention since the functionalization of membranes with nanostructures represent one way to address the main challenges in membrane performance.

The structures-properties relationships necessary in the development and design of innovative membranes used in wastewater treatment become important for obvious reasons; thus they were investigated in this thesis. In particular two nanostructures were considered as subject of this investigation: carbon nanotubes and polyoxometalates. The former were used in order to increase the membrane selectivity and permeability while the last in order to increase the bio and organic antifouling properties of the membrane. A modelling study based on Density Functional approach coupled with the use of home-made topological algorithms was carried out in this thesis. The use of such a approach allowed to be free of adjustable or fitting parameters providing a general methodology/criteria that could be applied in the study of other nanomaterials. In details this study has allowed to reach the following conclusions:

- A geometric criterion was provided in order to define the chirality (in particular the diameter) of SWNTs able to reject low molecular weight compounds. The criterion is based on an accurate ab-initio description of the molecular sizes. A validation of this criterion was also provided by means of QM calculations performed on a case study, i.e. Tyrosol molecules in-

side SWNTs whose configurations were taken by previous MD simulations. In particular the calculations revealed significant distortions of the Tyrosol molecules inside (8,8) SWNT which are not compensated either by hydrogen bonds formed in the molecular self-assembly or by the interactions between molecules and CNT. On the basis of this analysis the trapping of the Tyrosol molecules in (8,8) SWNT was energetically expensive. The geometric criterion proposed in fact predicted a rejection of the Tyrosol molecules by this CNT. Thus the rejection of Tyrosol occurs in agreement with the prediction of the geometric criterion.

- A selectivity-permeability optimization of Olygomer-IM functionalized CNT-polymer membranes was carried in order to obtain high rejection of organic solutes with low molecular weight without a marked fall in water permeability. In particular an ideal thin film composite (TFC) membrane and a chitosan porous membrane with vertically alignment MWNTs in the selective layer were examined. The selectivity-permeability optimization was achieved by calibrating the internal and external diameters of MWNTs and by an internal inlet reduction of large CNTs by means of selected fragment of polymers of intrinsic microporosity anchored on the CNT edge. This work is in submission status.
- A probable exchange between bromide and a Keggin polyoxometalate on polymeric membrane surface was theoretically assessed by a DFT investigation of the noncovalent interactions controlling the exchange of the mentioned anions. The quantum calculations predicted that there is no net energy gain if the Br^- ion is exchanged with the hydrated POM regardless of the surfactants concentrations on the membrane surface. This theoretical prediction was hence experimentally validated by means of gravimetical analysis of the Br^- anion. Although tested surfactants do not interact with these nanoparticle, this work helps to identify new surfactants, functional groups and new synthesis strategies able to trap more effectively the POMs.

Appendix A

Calculation of points $p_{mol,perm}$

The algorithm developed for the calculation of points $p_{mol,perm}$ belonging to the set $\sigma_{mol,perm}$ defined in sec. 3.3 is reported.

The following geometric problem is considered:

Problem A.0.1. *Let (x_c, y_c) be a point in a Cartesian plane that belongs to the disk $D(0, r_s)$ with center $(0, 0)$ and radius r_s and let V be a set of points in this disk. Let Q be a rectangle centred in (x_c, y_c) such that d_{min} and d_{max} are the minimum and maximum sides respectively and suppose that this rectangle can rotate in the plane around its center. Find some angle, if it exists, such that the rectangle does not include points of V and at the same time the rectangle is completely included in the disk.*

Let α be the angle that a straight line passing for the center of the rectangle forms with the x -axis of Cartesian plane. $\forall \alpha$ such that $\alpha \in [0, \pi)$, the rectangle Q_α is given by:

$$\alpha = 0$$

$$Q_\alpha = \left\{ (x, y) \in \mathbb{R}^2 \mid x_c - \frac{d_{max}}{2} \leq x \leq x_c + \frac{d_{max}}{2} \wedge \right. \\ \left. y_c - \frac{d_{min}}{2} \leq y \leq y_c + \frac{d_{min}}{2} \right\} \quad (\text{A.1})$$

$$\alpha = \frac{\pi}{2}$$

$$Q_\alpha = \left\{ (x, y) \in \mathbb{R}^2 \mid x_c - \frac{d_{min}}{2} \leq x \leq x_c + \frac{d_{min}}{2} \wedge \right. \\ \left. y_c - \frac{d_{max}}{2} \leq y \leq y_c + \frac{d_{max}}{2} \right\} \quad (\text{A.2})$$

$$\alpha \in (0, \frac{\pi}{2})$$

$$Q_\alpha = \left\{ (x, y) \in \mathbb{R}^2 \mid \right. \\ y \geq \tan\left(\frac{\pi}{2} + \alpha\right)x + \tan\left(\frac{\pi}{2} + \alpha\right)\left(\frac{d_{max}}{2 \cos \alpha} - x_c\right) + y_c \wedge \\ y \geq \tan(\alpha)x + y_c - \tan(\alpha)x_c - \left(\frac{d_{min}}{2 \cos \alpha}\right) \wedge \\ y \leq \tan\left(\frac{\pi}{2} + \alpha\right)x - \tan\left(\frac{\pi}{2} + \alpha\right)\left(\frac{d_{max}}{2 \cos \alpha} + x_c\right) + y_c \wedge \\ \left. y \leq \tan(\alpha)x + y_c - \tan(\alpha)x_c + \left(\frac{d_{min}}{2 \cos \alpha}\right) \right\} \quad (\text{A.3})$$

$$\alpha \in (\frac{\pi}{2}, \pi)$$

$$Q_\alpha = \left\{ (x, y) \in \mathbb{R}^2 \mid \right. \\ y \geq \tan\left(\frac{\pi}{2} + \alpha\right)x + \tan\left(\frac{\pi}{2} + \alpha\right)\left(\frac{d_{max}}{2 \cos \alpha} - x_c\right) + y_c \wedge \\ y \leq \tan(\alpha)x + y_c - \tan(\alpha)x_c - \left(\frac{d_{min}}{2 \cos \alpha}\right) \wedge \\ y \leq \tan\left(\frac{\pi}{2} + \alpha\right)x - \tan\left(\frac{\pi}{2} + \alpha\right)\left(\frac{d_{max}}{2 \cos \alpha} + x_c\right) + y_c \wedge \\ \left. y \geq \tan(\alpha)x + y_c - \tan(\alpha)x_c + \left(\frac{d_{min}}{2 \cos \alpha}\right) \right\} \quad (\text{A.4})$$

A schematic illustration is given in Fig. A.1 as function of the angle α .

Thus, by changing the angle $\alpha \in [0, \pi)$, all the positions of the rotated rectangle in the plane can be analyzed. This means that all angles can be investigated. In particular, $\forall \alpha$ can be checked if the rectangle includes points of V . In fact, for a fixed α , a point $v \in V$ is included in the rectangle if it is an element of Q_α . An angle α such that the rectangle does not include points of V is found if

$$\forall v \in V \quad \text{is} \quad v \notin Q_\alpha \quad (\text{A.5})$$

Actually, $\forall \alpha$ must be checked also that the rectangle centred in (x_c, y_c) is completely included in the disk and therefore no its parts are outside the disk. This

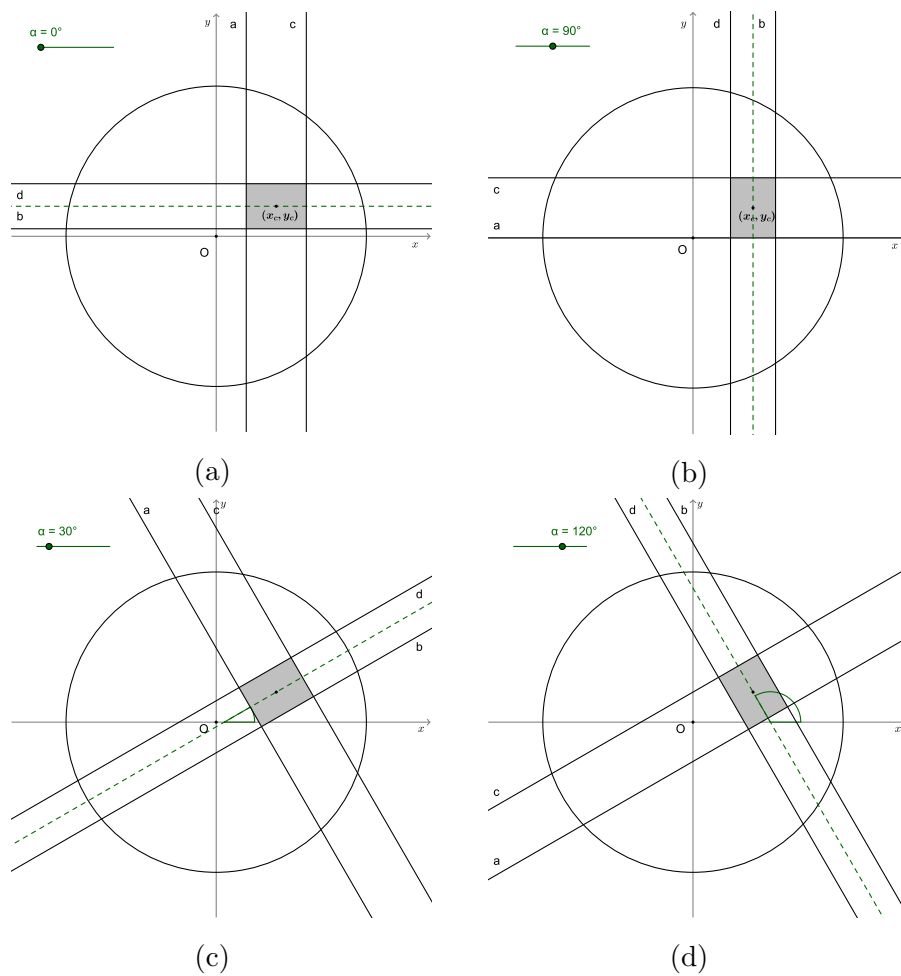


Figure A.1: Rectangle centred in (x_c, y_c) . The angle that the straight line (in dashed line) passing for the center of the rectangle forms with the x -axis of Cartesian plane is shown (a) for $\alpha = 0$, (b) for $\alpha = \frac{\pi}{2}$, (c) for $\alpha = \frac{\pi}{6}$, (d) for $\alpha = \frac{2\pi}{3}$.

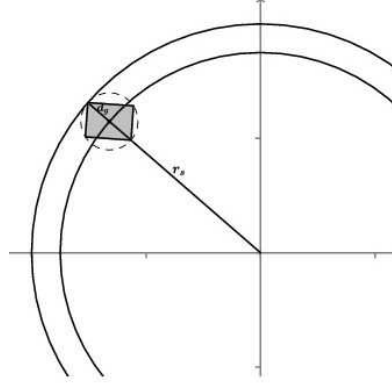


Figure A.2: Rectangle with center on the internal circle of the circular crown. In the rotation of the rectangle the vertices move along the dashed circle.

question is treated only if the point $(x_c, y_c) \in C_c$, where C_c is the circular crown defined as

$$C_c = \{(x, y) \in D(0, r_s) \mid x^2 + y^2 > (r_s - d_g/2)^2\} \quad (\text{A.6})$$

where d_g is the diagonal of Q_α .

In fact, if $(x_c, y_c) \notin C_c$, Q_α is completely included in $D(0, r_s) \forall \alpha$. The Fig. A.2 shows that the rectangle with center on the circle $x^2 + y^2 = (r_s - d_g/2)^2$ completely is included in $D(0, r_s) \forall \alpha$.

Thus, for a point $(x_c, y_c) \in C_c$, $Q_\alpha \subset D(0, r_s)$, if its four vertices are included in the disk:

$$\{A_\alpha, B_\alpha, C_\alpha, D_\alpha\} \subset D(0, r_s). \quad (\text{A.7})$$

The coordinates of $A_\alpha, B_\alpha, C_\alpha, D_\alpha \forall \alpha$ are found referring to the counter-clockwise rotation in two dimensions of the rectangle Q_0 through an angle α about the center (x_c, y_c) (Fig. A.3).

Starting from Q_0 vertices:

$$\begin{aligned} A_0 &= (-d_{max}/2, -d_{min}/2) \\ B_0 &= (d_{max}/2, -d_{min}/2) \\ C_0 &= (d_{max}/2, d_{min}/2) \\ D_0 &= (-d_{max}/2, d_{min}/2) \end{aligned} \quad (\text{A.8})$$

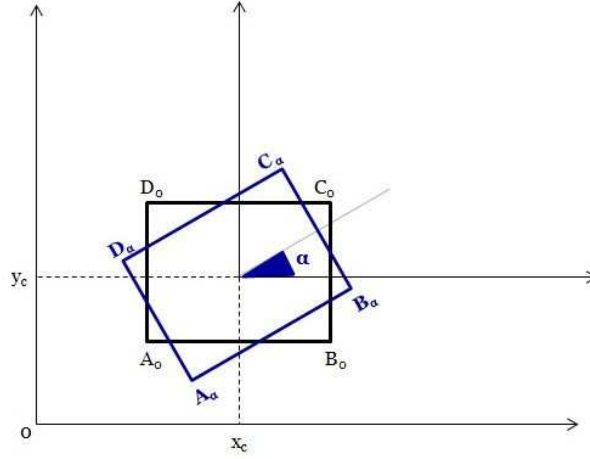


Figure A.3: Vertices of Q_α got by rotation of Q_0 through an α angle

the vertices of Q_α are given by:

$$\begin{aligned}
 A_\alpha &= U_\alpha A_0^T + \begin{pmatrix} x_c \\ y_c \end{pmatrix} \\
 B_\alpha &= U_\alpha B_0^T + \begin{pmatrix} x_c \\ y_c \end{pmatrix} \\
 C_\alpha &= U_\alpha C_0^T + \begin{pmatrix} x_c \\ y_c \end{pmatrix} \\
 D_\alpha &= U_\alpha D_0^T + \begin{pmatrix} x_c \\ y_c \end{pmatrix}
 \end{aligned} \tag{A.9}$$

where $U_\alpha = \begin{pmatrix} \cos \alpha & -\sin \alpha \\ \sin \alpha & \cos \alpha \end{pmatrix}$ is the rotation matrix through an angle α and where T denotes the transpose operation.

It is assumed that if some vertex of the rectangle belongs to the circumference with center $(0,0)$ and radius r_s then the rectangle is considered completely included in $D(0, r_s)$. This assumption is justified by the meaning associated with the rectangle. In fact, as described in sec. 3.2, since the rectangle contains disks, no part of these disks will touch the vertices. A disk may be just tangent at the two sides of the rectangle.

It is therefore possible to conclude that for a $(x_c, y_c) \in C_c$, α is a solution of the problem (A.0.1) if for that α angle the conditions (A.5) and (A.7) are at the same

time satisfied. Instead for $(x_c, y_c) \notin C_c$, α is a solution of the problem (A.0.1) if for that angle just the condition (A.5) is satisfied. The links between the geometric problem and the modeling of the functionalized CNT inlet are:

1. (x_c, y_c) is a free point, i.e. a point labelled with ‘0’;
2. the disk $D(0, r_s)$ is the CNT inlet having $r_s = r_{CNT} - r_C$;
3. V is the set of covered points i.e. points labelled with ‘1’;
4. the rectangle Q_α is the molecular MCS;
5. the point (x_c, y_c) such that an α angle is found for the problem (A.0.1) is a point in which the molecule is not rejected, $p_{mol,perm}$.

Thus by these links, for a given ‘0’ point, if a solution of the problem (A.0.1) exists then a position of the CNT inlet in which the molecule is not rejected is found. Contrary, if the problem doesn’t have a solution either some part of the molecule in that position come out from the CNT inlet or the molecule includes some ‘1’ point. In other words for all angulations checked the molecule is not able to take place in the position ‘0’. Thus \forall ‘0’ point of the CNT inlet, can be stated if that point is a $p_{mol,perm}$ point or not.

This problem is posed for each ‘0’ grid point and as a result the number of the elements of the set $\sigma_{mol,perm}$ defined in sec. 3.3 will be known.

Acknowledgments

The research leading to these results has received funding from the European Community's Seventh Framework Programme BioNexGen (Grant agreement no. CP-FP 246039-2) EU FP/ project. The author is grateful to CINECA for the use of High Performance Computers.

Desidero ringraziare il mio supervisore Dr. Giorgio De Luca per avermi seguito in tutto questo percorso di ricerca, il Prof. Davide Mattia dell'Università di Bath ed il Prof. Bartolo Gabriele per la loro disponibilità ed il loro prezioso contributo. Infine una sentita riconoscenza va alla Dr.ssa Isabella Baccarelli ed ai suoi colleghi per avermi sostenuta da lontano nei momenti sconfortanti di 'jobs failure'.